Theoretical and experimental considerations of the critical current density of DI-BiSCCO superconducting tapes as a function of magnetic field, field orientation, temperature and strain

SUNWONG, PRAPAIWAN

Theoretical and experimental considerations of the critical current density of DI-BiSCCO superconducting tapes as a function of magnetic field, field orientation, temperature and strain

Prapaiwan Sunwong

A thesis submitted in partial fulfilment of the requirements

for the degree of Doctor of Philosophy

Department of Physics, Durham University

2013

Theoretical and experimental considerations of the critical current density of DI-BiSCCO superconducting tapes as a function of magnetic field, field orientation, temperature and strain

Prapaiwan Sunwong

Abstract: The critical current density (J_c) of DI-BiSCCO superconducting tapes was measured as a function of magnetic field (B), field orientation (θ), temperature (T) and strain (ε) in a 15 T split-pair horizontal superconducting magnet using probes designed and built in-house. Strain was applied to samples using a modified bending beam apparatus with a copper beryllium springboard-shaped sample holder, which is capable of applying uniaxial strains of $-1.4\ \% \leq \varepsilon \leq 1.0\ \%$. The temperature of the sample was controlled with the use of an inverted insulating cup with a temperature stability of ± 80 mK to ± 200 mK. The vapour-cooled brass critical-current leads (incorporating high-temperature superconducting tapes) were optimised to minimise helium consumption. Optimisation includes consideration of the maximum safe temperature of the current leads and the effects of duty cycle and static helium boil-off. The optimised helium consumption of the leads is a factor of two lower than standard current leads optimised for magnets. $J_c(B,T,\theta,\varepsilon)$ data of the DI-BiSCCO tapes were characterised based on the superconducting-normal-superconducting Josephson junction model where J_c is determined by flux flow along the grain boundaries (or the normal junctions). It was found that grain boundaries in the DI-BiSCCO tapes are thick (several tens of nanometre) and exhibit semiconducting behaviour. The degree of misalignment has been included into the anisotropy analysis of J_c and the correlation between the effective anisotropy and texturing of the sample obtained. Analysis of three different samples (Nb_3Sn, YBCO and BiSCCO) is presented where the average local properties of the grain boundaries were extracted from magnetisation and the transport J_c data.

Table of Contents

Declaration and Copyright

I hereby declare that this thesis is my own work which has not been submitted for any award in any university. If material has been generated through joint work, my independent contribution has been clearly indicated. To the best of my knowledge, no part of the material offered has previously published by another person, except where due reference has been made.

Prapaiwan Sunwong

July 2013

Acknowledgements

Many people have provided the assistance and guidance throughout my PhD. First of all, I would like to thank my supervisor, Professor Damian Hampshire, for giving advice, support and encouragement. I would also like to thank everyone in superconductivity group; Josh Higgins, Betti Pusceddu, James Orr, Steve Pragnell, Helen Armstrong, Xifeng Lu, Mark Raine and Yeekin Tsui for providing a warm working environment. Special thanks go to Josh, Mark and Yeekin for giving many technical discussions and invaluable assistance in everything I needed.

I would like to acknowledge all of the supporting staff in Department of Physics, Durham University. Thanks to Phil Armstrong, Steve Lishman, Malcolm Robertshaw, Lee Bainbridge, Andrew Crosby and all mechanical workshop staff for their quality workmanship. They also provided me the practical skills and experience in engineering work during my first year, which are necessarily useful. Thanks to Wayne Dobby, John Summerill and John Dobson for their technical support and some equipment used in my experiment. Thanks to Norman Thompson and Duncan McCallum for their advice regarding the healthy and safe working environment. Thanks to Leon Bowen for his assistance with scanning electron microscope and light microscope. I also thank all of the administrative staff that are always glad to help with any paperwork.

I would like to thank Sumitomo Electric Industries for supplying the DI-BiSCCO tapes used in this work as part of collaboration, and Professor Koso Osamura for many useful discussions. Thanks to the Royal Government of Thailand Scholarship (DPST) for providing financial support and the Office of Educational Affairs, the Royal Thai Embassy for providing other necessary supports during my study in the United Kingdom. Finally, special thanks to my parents, friends and John for their love that helped me through any difficult situation.

Chapter 1

Introduction

Superconductivity is a captivating phenomenon found in those materials that exhibit the vanishing of electrical resistance below a critical temperature. An electric current can be transmitted through a superconductor without any dissipation. For a century, superconductivity has attracted the attention of scientists and engineers throughout the world and has led to developing an understanding and enabling the practical use of superconducting materials. Superconductors have been used successfully in the magnet systems of Magnetic Resonance Imaging (MRI) scanners and Nuclear Magnetic Resonance (NMR) spectrometers which are widely used in medical and scientific research applications. Superconducting magnets in large systems have also been accomplished. The Large Hadron Collider (LHC) was successfully built with a 27-kilometre ring of superconducting magnets and operated for collisions at 8 TeV in 2012, which will be increased to 13 TeV in 2015 [1]. ITER, the world's largest tokamak being built in France with contribution from several countries around the world, uses superconducting magnets to confine, shape and control the plasma for fusion reactions. The reactor has been designed to produce an output energy up to 10 times of the input energy. It is planned to be operated in the next decade and will demonstrate the feasibility of a sustainable source of fusion energy that emits no pollution to the environment [2].

The production of superconducting magnets has been dominated by the use of low-temperature superconductors such as Nb_3Sn and NbTi which are necessarily operated in liquid helium. The shortage of helium is currently a serious issue and its supply has recently become erratic [3, 4]. Scientists and users are aware of this problem and

searching for a solution or alternative cooling methods. In fact, discovery of a ceramic copper oxide compound which is superconductive at above 30 K in 1986 [5] has led to the discovery of various other high-temperature superconducting materials that exhibit critical temperatures above liquid nitrogen temperature. These materials have provided the possibility of superconducting applications operated at lower cooling cost in liquid nitrogen. However, the use of them is still limited due to their ceramic properties and a lack of understanding of the mechanism(s) that give rise to the high-temperature superconductivity. Their brittle nature restricts the available manufacturing processes. Technological fabrication techniques have been developed to overcome this problem for example by introducing metallic layers in wire/tape structure so that the conductors are now easier to handle. The anisotropy and grain boundary problems are also major concerns. The grain boundaries in high-temperature superconductor suppress current flow [6]. Therefore, the critical current density in these materials will not achieve the intrinsic ability unless the grain connectivity and alignment are understood and improved. Nevertheless, the high-temperature superconductors can be used in many applications including power cables, transportation, motors, transformers, power storage devices, fault current limiters, superconducting magnets and SQUID (superconducting quantum interference device) magnetometers which until recently were restricted to the use of low-temperature superconductors [7].

The research reported in this thesis concentrates on the critical current density of BiSCCO tapes, a commercially available high-temperature superconductor with the highest critical temperature of ~110 K. The critical current density is probably the most important property for applications. In operation, superconductors are expected to experience self-field generated by flowing current, external magnetic fields, different operating temperatures and mechanical strains. Superconducting magnet engineering needs to know the critical current density as a function of all operational parameters involved in order to design the magnet efficiently. Therefore, understanding the effect of field, temperature and strain on the critical current density

is crucial. In this work, transport (and some magnetic) critical current densities of BiSCCO tapes were measured and the data were analysed based on a theoretical model previously established in our group. The results provide insight into the current carrying mechanism in polycrystalline superconductors.

This thesis is structured as follows: Chapter 2 provides general characteristics of superconductor and fundamental theories of superconductivity including the phenomenological Ginzburg-Landau theory and BCS theory which describes superconductivity from the condensation of electron pairs. Flux pinning models are also discussed in the last section to explain the generally accepted origin of critical current density in superconductor. Chapter 3 is a review of high-temperature superconductivity which includes general properties, important production techniques and challenges in understanding and improving the superconducting properties to make it useful in applications. Chapter 4 gives the description and specification of BiSCCO samples used in this work and presents the results from early critical current measurements. Effects of magnetic field, field orientation and strain on the transport critical current density are discussed. Chapter 5 presents design and calculations of the probes used to perform the critical current measurements in high magnetic fields as a function of field, field orientation, temperature and strain. Optimisation and construction of the current leads and the variable-temperature system are the main interests. Chapter 6 introduces the superconducting-normal-superconducting Josephson junction model used to describe the critical current density in polycrystalline superconductors based on flux flow along the grain boundaries. Experimental results of three samples (Nb_3Sn, YBCO and BiSCCO) are discussed, showing applicability of the model regardless of the type of superconductors studied. Transport measurements on BiSCCO tapes were performed at various temperatures using the probe presented in Chapter 5. The results are reported and discussed in Chapter 7. Finally, suggestions for future work are stated in Chapter 8.

Chapter 2

Fundamentals of superconductivity

2.1 Introduction

In order to explain the mechanisms giving rise to superconductivity, comprehensive studies in various aspects are still in action. This chapter introduces the characteristic properties of superconductivity and provides the description of the theories including the Ginzburg-Landau theory introduced in 1950 which explains superconductivity from a phenomenological point of view and BCS theory introduced in 1957 which describes superconductivity from a microscopic point of view and includes the condensation of electron pairs. Finally we discuss flux pinning models which explains the origin of critical current density in superconductor.

2.2 Characteristic properties of superconductivity

Superconductivity was discovered in 1911 by Heike Kamerlingh Onnes [8] when he measured electrical resistance of solid mercury as a function of temperature. It was found that the mercury exhibits vanishing resistance at temperatures below ~4.2 K instead of approaching a constant value as expected by some of the current theories for metals at the time. The plot of resistance versus temperature from Onnes' original work entitled "*On the Sudden Change in the Rate at which the Resistance of Mercury Disappears*" is shown in Figure 2.1(a) where the resistance drops abruptly

to ~10^{-5} Ω in the superconducting state. Other superconductors exhibit the same behaviour with the *transition temperature* or *critical temperature* (T_c) varying from material to material. Another important characteristic of superconductivity was discovered two decades later by Walther Meissner and Robert Ochsenfeld [9] when they found the exclusion of magnetic flux from the interior of superconducting tin and lead samples. This effect is known as the *Meissner effect* and is visualised in Figure 2.1(b).

Figure 2.2 shows the magnetic response in two types of superconductors which are simply differentiated by their behaviour in a magnetic field. Type I superconductors act as a perfect diamagnet [10] in an external magnetic field strength less than the value of the *critical field strength* (H_c) at temperature below T_c. As a result, the total magnetic field inside type I superconductors is zero due to the cancellation of the applied magnetic field and the magnetisation, which is the characteristic of the Meissner state. The exception is at the surface layer of superconductor where the magnetic field can always penetrate. If the field strength and temperature are higher than H_c and T_c, the superconductivity disappears.

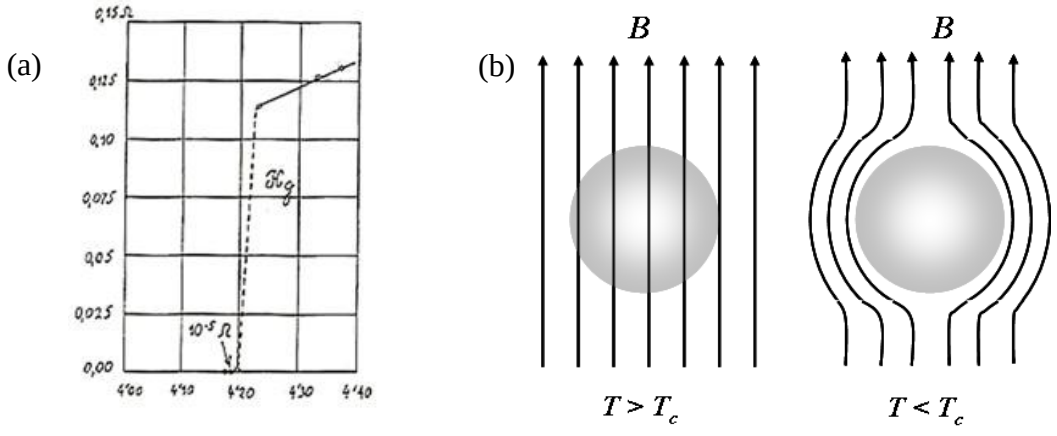

Figure 2.1 (a) Electrical resistance of mercury as a function of temperature measured by Onnes, showing zero resistance state below ~4.2 K [8]. (b) Magnetic flux exclusion from superconducting material in Meissner state below T_c.

The magnetic response in type II superconductors is more complicated. The external magnetic field can partly penetrate into a bulk of material while it still has superconducting properties up to the *upper critical field strength* (H_{c2}). This regime is called the *mixed state* due to the coexistence of normal regions and superconducting regions. The penetration of magnetic field starts at the *lower critical field strength* (H_{c1}) where the magnetisation becomes less negative before reaches zero at the H_{c2}. Below $H_{c1,}$ type II superconductor displays a Meissner-like behaviour.

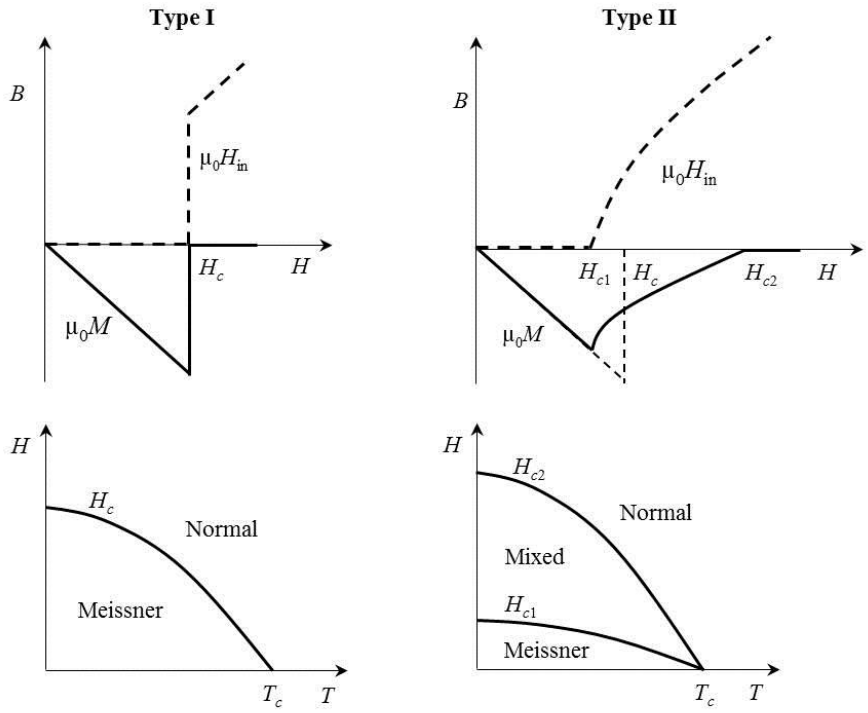

Figure 2.2 Magnetic response in type I and type II superconductors. The Meissner state is found in type I superconductor below H_c while it is found below H_{c1} in type II superconductor before the superconductor enters the mixed state as the magnetic field increases. Eventually materials become normal when the field exceeds H_c in type I and H_{c2} in type II superconductors. These behaviours occur below T_c.

2.3 Ginzburg-Landau theory

Following the London equation of superconductivity and the Landau theory of second-order phase transitions introduced in 1930s [11, 12], Ginzburg and Landau together suggested that phase transition in a superconductor can be explained in terms of a complex order parameter, $\psi(\vec{r}) = |\psi(\vec{r})|e^{i\Theta}$ with its square $|\psi|^2$ represents the *superelectron* density (n_e^*) [13]. Similar to magnetisation in the Landau theory, the superconducting order parameter decreases with increasing temperature due to thermal fluctuation and vanishes at the critical temperature. The Gibbs free energy density functional of a superconductor, which is analytic and obeys the symmetry of Hamiltonian, is expressed in the form

$$g(\vec{r},T) = g_n(\vec{r},T) + \alpha|\psi|^2 + \frac{\beta}{2}|\psi|^4 + \frac{1}{2m_e^*}\left|\left(-i\hbar\nabla - e^*\vec{A}\right)\psi\right|^2 + \frac{|\vec{B}|^2}{2\mu_0} - \vec{H}_0\cdot\vec{B} + \frac{|\vec{H}_0|^2}{2\mu_0}\,, \tag{2.1}$$

where $g_n(\vec{r},T)$ is the free energy density in the normal phase where the system is complete disordered, α and β are temperature-dependent phenomenological parameters, $m_e^* = 2m_e$ is mass of the superelectron (twice of the free electron mass m_e), $e^* = 2e$ is superelectron charge (twice of the free electron charge e), $\vec{A}$ is the magnetic vector potential and $\vec{B}$ is the magnetic field. Minimising the total free energy with respect to the order parameter in the London-Landau gauge ($\nabla\cdot\vec{A} = 0$) gives

$$\alpha\psi + \beta|\psi|^2\psi + \frac{1}{2m_e^*}\left(-i\hbar\nabla - e^*\vec{A}\right)^2\psi = 0\,, \tag{2.2}$$

which is known as the first Ginzburg-Landau equation. Similarly, minimisation of the free energy with respect to the vector potential and substituting the Ampère Law, $\nabla\times\vec{B} = \mu_0\vec{J}$, provides the second Ginzburg-Landau equation:

$$\mu_0 \vec{J} = -\frac{i\hbar e^*}{2m_e^*}\left(\psi^*\nabla\psi - \psi\nabla\psi^*\right) - \frac{e^{*2}}{m_e^*}\vec{A}|\psi|^2 \qquad (2.3)$$

where $\vec{J}$ is the superconducting current density. Considering magnetic flux penetration in a type II superconductor, (2.3) leads to quantisation of the magnetic flux (Φ) through the surface of the normal domain and line integral of the current density (known as screening current density) around the domain, with flux quantum (Φ_0) of h/e^* = 2.0679×10^{-15} Tm^2. The flux quantisation occurs in the form of vortices, consisting of the normal core region and the outer region where the field exponentially decreases with distance from the core. The magnetic flux is called *fluxoid* or *fluxon*. As mentioned in the previous section, this is a characteristic of type II superconductor in the mixed state or *vortex state*. The vortices form a triangular vortex lattice which was first obtained using a perturbation method that dealt with the nonlinear term $\beta|\psi|^2\psi$ in the mixed state below the upper critical field. It was also confirmed later by the experiments [14-16]. This arrangement provides a minimum value of the free energy. A contour plot of normalised $|\psi|^2$ is shown in Figure 2.3 where the vertical distance between vortex cores is $2\pi^{1/2}\xi/3^{1/4}$ and the horizontal distance between the rows of vortices is $3^{1/4}\pi^{1/2}\xi$ [17]. Here ξ is the *coherence length* which is the length scale at which the thermodynamic fluctuation of superconducting parameter occurs. From the first Ginzburg-Landau equation, ξ is defined as

$$\xi \equiv \left(\frac{\hbar^2}{2m_e^*|\alpha(T)|}\right)^{1/2}. \qquad (2.4)$$

The coherence length is therefore temperature dependent with $\alpha(T) = -\alpha_0(1 - T/T_c)$. Another characteristic length of superconductor is the *penetration depth* (λ) which is a parameter that represents the depth that magnetic field penetrates into a superconductor in its superconducting state. The magnetic field exponentially decays to zero inside the superconductor and λ is the distance over which the field decreases by 1/e.

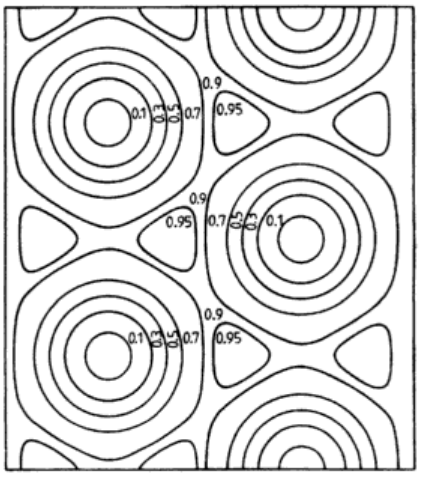

Figure 2.3 Level surfaces of normalised $|\psi|^2$ for the triangular vortex lattice, which also represent the lines of constant magnetic field and constant current flow [17].

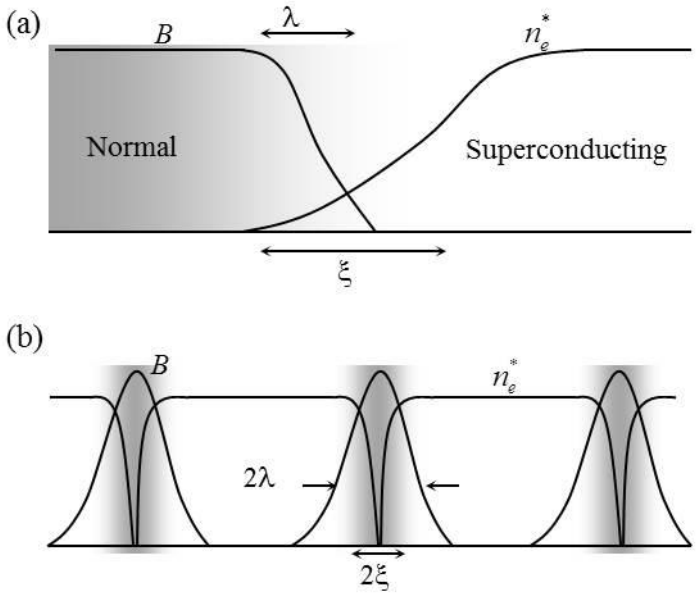

Figure 2.4 (a) Increase in the number of superconducting electrons n_e^* and the decay of the magnetic field *B* at the interface of a type I superconductor. (b) Change in the number of superconducting electrons and magnetic field around three fluxons in the vortex state of type II superconductor.

The second Ginzburg-Landau equation gives an expression for λ as

$$\lambda = \left(\frac{m_e^*}{\mu_0 n_e^* e^{*2}} \right)^{1/2} \tag{2.5}$$

which is also temperature dependent since the density of superelectrons changes with temperature. At $T = T_c$ where density of superelectron vanishes, the penetration depth becomes infinite and the superconductor becomes normal with complete penetration by the magnetic field.

The ratio of the penetration depth to the coherence length of superconductor determines whether the superconductor is type I or type II. The ratio λ/ξ is known as the *Ginzburg-Landau parameter* (κ_{GL}). Superconductors are classified as type I or type II depending on whether this parameter is less than or greater than $1/\sqrt{2}$ respectively. Figure 2.4 shows the plots of magnetic field and superconducting electron density near the interface in two types of superconductor. Ginzburg and Laudau [13] showed that the surface tension, as well as the surface enery, changes from positive to negative values at $\kappa_{GL} = 1/\sqrt{2}$. If $\kappa_{GL} < 1/\sqrt{2}$, the surface energy is positive because the energy associated with the exclusion of magnetic field is less than the condensation energy and the superconductor is type I. On the other hand, if $\kappa_{GL} > 1/\sqrt{2}$, the surface energy is negative and it is energetically favourable for the superconductor to form the vortices [18] showing type II behaviour.

Critical field strength

At the critical field strength at which the superconductivity of type I superconductor is destroyed, the Gibbs free energy in the normal phase and superconducting phase are equal and the transition is a first-order phase transition. One can obtain the expression for H_c from (2.1) by substituting $\vec{B} = 0$ in the superconducting phase and $\psi = 0$ in the normal phase, which gives

$$H_c{}^2 = \frac{|\alpha|^2}{\mu_0 \beta}. \tag{2.6}$$

Experimentally, the temperature dependence of H_c of some metallic superconductors shows a common parabolic dependency described by $H_c(T) \cong H_c(0)[1-(T/T_c)^2]$ [10].

In type II superconductor, existence of the mixed state leads to a continuous change in the order parameter approaching the H_{c2} and the superconductor exhibits a second-order phase transition from a reduction of diamagnetic energy. By solving the linearised form of the first Ginzburg-Landau Equation where the nonlinear term $\beta|\psi|^2\psi$ is ignored, the expression for H_{c2} can be derived. It is shown in (2.7) which is valid for both types of superconductor. In type I superconductor, H_{c2} is smaller than H_c and represents the stability boundary of the normal phase [17].

$$H_{c2} = \frac{m_e^* |\alpha(T)|}{e\hbar\mu_0} = \frac{\Phi_0}{2\pi\mu_0 \xi^2(T)} = \kappa_{\mathrm{GL}} \sqrt{2} H_c \tag{2.7}$$

Anisotropic Ginzburg-Landau theory

Due to structural anisotropy of some superconductors, most of the thermodynamic properties can be anisotropic and can be understood in terms of the *anisotropic Ginzburg-Landau theory* where superconductor is treated as a continuum with different properties along the three principal axes [19-21]. In the high-T_c superconductors, the anisotropy in the *ab*-plane is generally negligible and the parameter used to described the anisotropy (which is doping dependent) is defined as

$$\Gamma = \left(\frac{m_{ec}^*}{m_{e\,ab}^*} \right)^{1/2} = \frac{\lambda_c}{\lambda_{ab}} = \frac{\xi_{ab}}{\xi_c} = \frac{H_{c2ab}}{H_{c2c}} > 1. \tag{2.8}$$

If the vortices are at an arbitrary angle θ relative to the *ab*-plane, the Ginzburg-Landau parameter is in the angular form and the upper critical field from (2.7) becomes angular dependent, that is,

$$H_{c2}(\theta) = H_{c2c}\left(\sin^2\theta + \frac{1}{\Gamma^2}\cos^2\theta\right)^{-1/2} \quad \text{or}$$

$$\left(\frac{H_{c2}(\theta)\sin\theta}{H_{c2c}}\right)^2 + \left(\frac{H_{c2}(\theta)\cos\theta}{H_{c2ab}}\right)^2 = 1. \qquad (2.9)$$

The external magnetic field penetrates into the anisotropic superconductor in the form of continuous vortices, similar to that predicted from the isotropic Ginzburg-Landau theory. At low temperature, the vortices are straight with elliptical cross-sections and arrange themselves in a periodic, solid-like lattice. When the temperature is increased, the vortices become undulate due to thermal agitation and the vortex lattice undergoes first-order melting at a sufficiently high temperature. Increasing the magnetic field decreases the melting temperature of the vortex lattice and the degree of anisotropy plays an important role in determining the melting line in the *B*-*T* phase diagram. The vortices become floppier with increasing anisotropy and the melting temperature is displaced to lower temperatures.

An implicit assumption of the Ginzburg-Landau theory is that all the characteristic lengths of superconductivity are much larger than the interatomic spacing or layer periodicity length (*S*) in layered superconductor. At temperature close to T_c, all the characteristic lengths are much larger than *S*. However, the coherence length (especially the smallest one ξ_c) is reduced at lower temperature and can be smaller than *S*, making the continuum theory invalid [19, 22]. Lawrence and Doniach [23] introduced a useful theoretical model in which a layered superconductor is approximated as a stack of weakly coupled superconducting layers. It treats the superconductivity within the layers via the Ginzburg-Landau theory and treats the flow of current between adjacent layers via the Josephson effect. It can be reduced to

the anisotropic Ginzburg-Landau theory at the temperature close to T_c due to strong interlayer coupling. The transition temperature from two-dimensional (2D) behaviour (weak coupling) to three-dimensional (3D) behaviour (strong coupling) is given as

$$T_{2D-3D} = T_c \cdot \left[1 - \frac{1}{\Gamma^2} \frac{2\xi_{ab}^2(0)}{S^2} \right]. \tag{2.10}$$

The angular dependence of H_{c2} in the 2D case is given by Tinkham [24] as

$$\left| \frac{H_{c2}(\theta)\sin\theta}{H_{c2c}} \right| + \left(\frac{H_{c2}(\theta)\cos\theta}{H_{c2ab}} \right)^2 = 1. \tag{2.11}$$

In 2D behaviour, a vortex line passing through a stack of weakly Josephson-coupled layers behaves as a set of 2D pancake vortices connected by Josephson strings [19, 21]. Pancake vortices are characterised by nearly circular supercurrent patterns confined to the individual superconducting layers, as shown in Figure 2.5. Josephson strings are short segments of Josephson vortices, whose axes are confined to the weakly coupled regions.

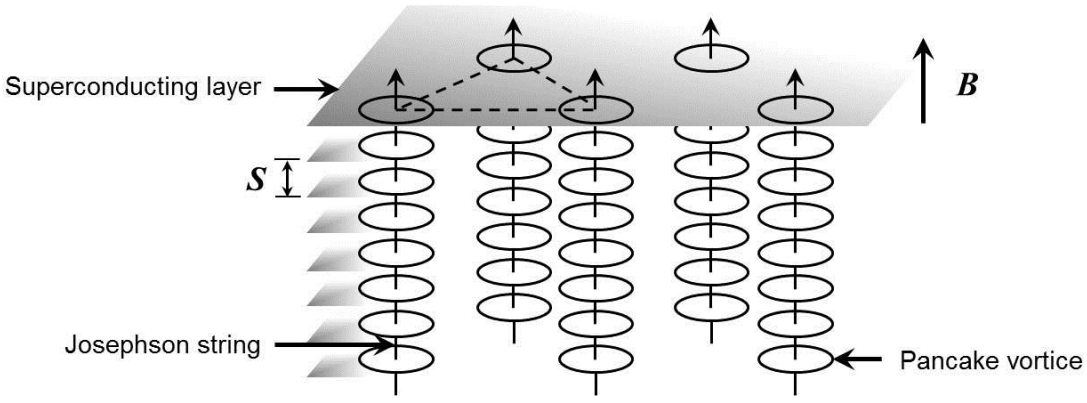

Figure 2.5 Stacks of pancake vortices connected by Josephson strings in a layered superconductor with 2D behaviour. Magnetic field is normal to the superconducting layer.

2.4 BCS theory

The experimental evidence of the isotope mass dependence of the critical temperature of mercury was found in 1950 by Maxwell [25] and Reynolds [26]. This isotope effect obeys the empirical law $T_c M_I^{1/2}$ = constant (M_I is the isotope mass), which is also true for other superconductors. More importantly, it shows a relation between superconductivity, which is a property of the electron system, and a characteristic of the crystal lattice and led to the development of microscopic theory of superconductivity. The BCS theory is named after John Bardeen, Leon Cooper and Robert Schrieffer who introduced this theory in 1957 [27] based on the isotope effect. It was proposed that electrons in a superconductor form *Cooper pairs* by means of an interaction between electrons and the lattice to lower the ground state energy. The attractive interaction is isotropic so the bound electron pairs are formed in a state with zero orbital angular momentum (*s*-wave pairing). This formation could in principle increase the kinetic energy since the momentum of the electrons changes to a new value above the Fermi surface, however, the potential energy in many-electron system decreases to more than compensate for the kinetic energy increase. By solving Schrodinger equation for two electrons interacting via a potential *V*, the eigenenergy for a weak coupling limit is obtained as

$$E = 2E_F - 2\hbar\omega_D \exp\left(-\frac{2}{V_0 D(E_F)}\right) \tag{2.12}$$

where ω_D is a phonon frequency, V_0 is the attractive potential and $D(E_F)$ is the density of states at the Fermi energy. The pair state always has energy lower than the normal ground state energy, making it more stable. This energy is also much less than phonon energy so the T_c is much less than Debye temperature. The difference between the Fermi energy and the Cooper pair energy is known as binding energy of the Cooper pair.

Figure 2.6 shows the pairing mechanism according to the BCS theory. The origin of the attraction between two electrons can be considered as the exchange of virtual phonons from an electron-phonon interaction. When atoms are disturbed by the electron moving in the crystal, the harmonic oscillator will move from the ground state to the unstable excited state and releases the energy when it returns. The energy, or virtual phonon, is then absorbed by another electron, leads to additional attraction between them. The Cooper pair momenta are slightly above the Fermi surface, within the layer of thickness $\hbar\omega_D$.

The BCS ground state has its energy separated from a single-electron state by an *energy gap* (Δ). The magnitude of the energy gap at absolute zero is given by

$$\Delta(0) = 2\hbar\omega_D \exp\left(-\frac{1}{\lambda'}\right), \tag{2.13}$$

where $\lambda' = VD(E_F)$ is the coupling constant that determines the strength of the electron-phonon coupling and is much less than 1 (weak-coupling approximation). At higher temperatures, the attraction between electrons is disrupted by thermal chaotic motion and electrons in the excited state have to be described by the *quasiparticles* [28] which behave like normal electrons even though their energy is changed. An expression for the energy gap near T_c is

$$\Delta(T)\big|_{T\to T_c} = ak_B T_c\left(1-\frac{T}{T_c}\right)^{1/2} \tag{2.14}$$

where a = 3.06 for the weak-coupling approximation. The two-fluid model describes the system as consisting of superconducting electrons and quasiparticles. At zero temperature, there is no excitation or quasiparticles. The number of quasiparticles exponentially increases with temperature while the energy gap and the number of superconducting electrons decrease and eventually vanish at the critical temperature. The BCS critical temperature is proportional to the energy gap at zero temperature and is given by (2.15) where k_B is the Boltzmann constant.

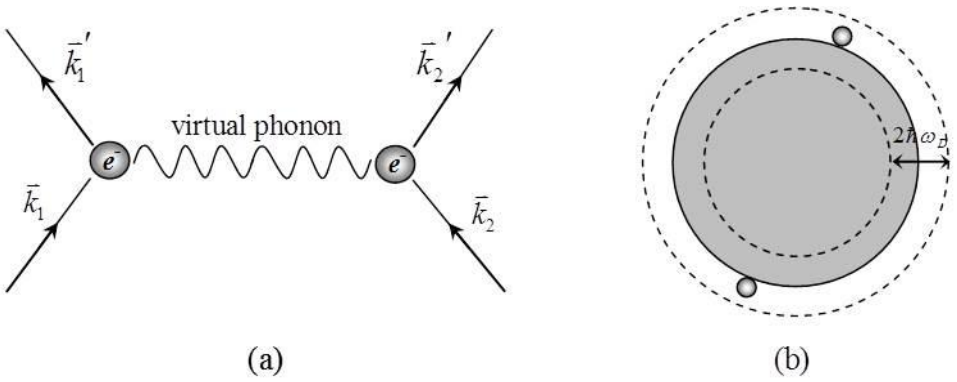

Figure 2.6 (a) The pairing mechanism via exchange of a virtual phonon (with energy $\hbar\omega_D$) - the momenta of two electrons change from $\vec{k}_1$ and $\vec{k}_2$ to $\vec{k}_1'$ and $\vec{k}_2'$ after the interaction. (b) The isotropic Fermi sphere of the electron system (the solid line shows the Fermi energy) - the new momenta $\vec{k}_1'$ and $\vec{k}_2'$ have to be above the Fermi surface since all orbitals below are filled.

$$k_B T_c = 1.14\hbar\omega_D \exp\left(-\frac{1}{\lambda'}\right) = \frac{2\Delta(0)}{3.52} \tag{2.15}$$

The energy gap in superconductor was first observed by Glover and Tinkham in 1956 using the infrared spectroscopy [29, 30]. Normally, scattering of electrons moving through a metal results in an electrical resistance because the electrons dissipate their energy. Existence of the energy gap in superconductor means that, if electrons move slowly (low current flowing in the superconductor) the electrical resistance will be zero. This is because an energy associated with the scattering process is not enough to break the pair. Nevertheless, the resistance appears if the current exceeds a certain value of the critical current, at which the Cooper pair density vanishes.

BCS theory successfully described superconductivity in many materials with weak electron-phonon coupling. For materials with strong coupling such as Pb, Hg, Bi_2Tl and $Pb_{0.7}Bi_{0.3}$ with the coupling constant larger than 1, Eliashberg modified the BCS theory and provided the equation that includes information about the relative strength

of the phonon system and the electron-phonon interaction which can be reduced to the BCS theory in the weak coupling approximation [31]. An expression for the energy gap derived from Eliashberg's equation uses $a = 3.06\cdot[1+8.8(T_c^2/\Theta_D^2)\ln(\Theta_D/T_c)]$ (Θ_D is Debye temperature), while an expression for the critical temperature uses an effective coupling constant (λ'_{eff}) which takes into account the Coulomb pseudo potential instead of the ordinary coupling constant [28, 32, 33]. The critical temperature for strong electron-phonon coupling can be written as

$$T_c \cong 0.25\Theta_D\left[\exp\left(\frac{2}{\lambda'_{eff}}\right)-1\right]^{-1/2}. \qquad (2.16)$$

With the typical values of λ'_{eff} of 1 for strong coupling and Θ_D of 300 K for alloy materials [34], upper limit of T_c in phonon-mediated superconductors is ~30 K.

The connection between the Ginzburg-Landau theory and the BCS theory was established by Gor'kov in 1959 [35] who derived the Ginzburg-Landau equations from the BCS theory. He identified the order parameter with the wave function of electron pair so the order parameter is proportional to the energy gap described in the BCS theory. A spherically symmetric gap results from the *s*-wave pairing, while asymmetric energy gaps which have also been observed result from unconventional pairing (*p*-wave and *d*-wave) with interactions other than that between electrons and phonons.

Critical field strength

In *s*-wave superconductors, the transition from the superconducting phase to the normal phase in magnetic field occurs when the magnetic energy overcomes the condensation energy of the Cooper pairs and polarises the antiparallel paired electrons. This is the Pauli paramagnetic limit (H_p) for singlet superconductor. The critical field strength is given by definition as

$$\frac{1}{2}\mu_0[H_c(0)]^2 = \frac{1}{2}D(E_F)[\Delta(0)]^2. \quad (2.17)$$

Following Gor'kov equations, the Werthamer–Helfand–Hohenberg (WHH) theory was developed to predict the upper critical field of type II superconductors in the dirty limit by including the effects of Pauli spin paramagnetism and spin-orbit impurity scattering (neglecting strong-coupling and Fermi surface anisotropy effects) [36]. While the effect of spin paramagnetism limits the critical field strength, the effect of spin-orbit scattering increases the Pauli spin susceptibility in the superconducting state and drives the transition to be second order. The prediction of H_{c2} in the orbital limit can be expressed by

$$H_{c2}(0) = -0.693T_c\left(\frac{\mathrm{d}H_{c2}}{\mathrm{d}T}\right)_{T_c}. \quad (2.18)$$

Therefore, the ratio between $\sqrt{2}\,H_{c2}(0)$ and $H_p(0)$ or the Maki parameter [37] represents the relative strength of the orbital pair breaking and Pauli paramagnetic pair breaking.

p-wave and d-wave superconductivity

While the order parameter in *s*-wave superconductivity (angular momentum $l = 0$) can be a complex number, it should be written as a complex vector to account for all components of the spin pairing in *p*-wave ($l = 1$) and *d*-wave ($l = 2$) superconductivity which is favoured in the correlated electron materials. *P*-wave pairing was first discovered in superfluid ^{3}He [38, 39] and the evidence suggesting its existence in superconductors was reported later in several compounds including the layered perovskite oxide Sr_2RuO_4 [40, 41]. *P*-wave pairing is sometimes referred to as the *odd parity superconductivity* or *triplet superconductivity* from the parity of the spatial part and the binding spin state of the order parameter which obeys an antisymmetry requirement. Generally, *p*-wave superconductors are highly anisotropic so the carriers in certain orientations cannot move freely (e.g. between layers). The

order parameter is then polarised within the *ab*-plane parallel to applied magnetic field [42]. Some *p*-wave states give very similar thermodynamic data to the *s*-wave and *d*-wave states. In order to confirm the existence of the *p*-wave pairing, sensitive probes must be coupled to either the odd parity or the spin part of the pairing. Many experiments have reported evidence suggesting the existence of the triplet pairing. These include the upper critical field higher than the Pauli limit in the organic superconductor $(TMTSF)_2PF_6$ [43], the unchanged spin susceptibility determined by Knight shift across T_c showing the odd parity superconducting state with parallel spin pairing in the heavy fermion superconductor UPt_3 [44, 45] and the layered oxide Sr_2RuO_4 [40] and also the lack of a coherence peak of the nuclear spin-lattice relaxation rate in the Sr_2RuO_4 [41].

D-wave pairing is found in the high-temperature superconducting cuprates [46, 47] where nodes in the energy gap are confirmed by measurements [48]. The ground state superconducting order parameter is strongly momentum dependent with the maximum value in the direction of the crystallographic axes *a* and *b* [49]. Figure 2.7 shows the shape of the order parameter in YBCO and BiSCCO where the region with a negative order parameter appears between two maxima. In BiSCCO, deviation from tetragonal symmetry is small so there are four maxima displaced by $\pi/2$ and the negative regions are in the vicinity of $\pi/4$. In YBCO, the chains destroy singularities in the *b*-direction so there are only two maxima displaced by π and the negative regions are expected in the *b*-direction [50]. Superconductivity in *d*-wave pairing materials is easily destroyed due to the small mean free paths and the sensitivity of superconductivity to non-magnetic impurity elastic scattering. The stability of the *d*-wave pairing depends on the details of band structure and the pairing potential [51-53]. The nodeless order parameter or finite energy gap (therefore no small energy excitation along the node) in *d*-wave pairing cuprates can be induced by doping or application of magnetic field along the *c*-axis. As a result, the symmetry of order parameter changes from pure $d_{x^2-y^2}$ to $d_{x^2-y^2}+is$ or $d_{x^2-y^2}+id_{xy}$ [49, 54, 55].

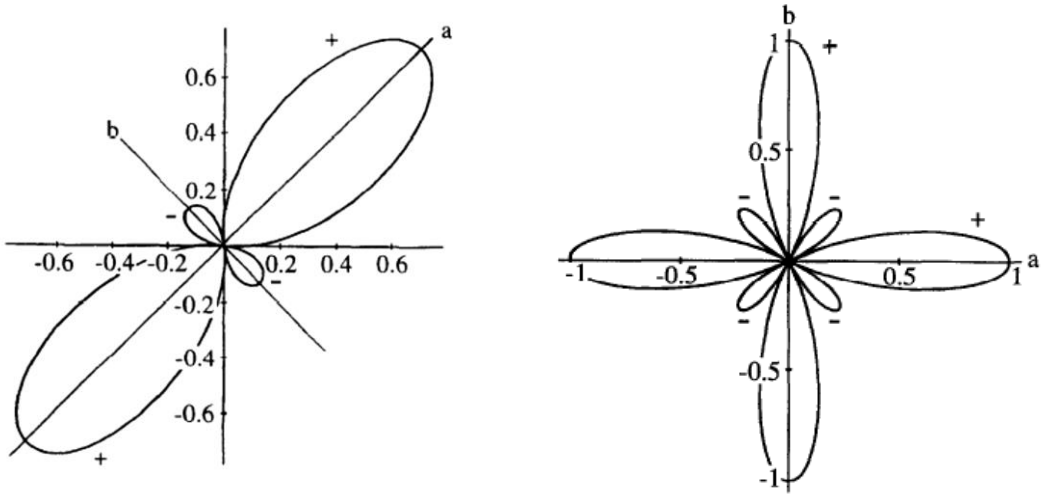

(a) (b)

Figure 2.7 Polar plot representing the shape of the order parameter in (a) YBCO and (b) BiSCCO [50].

2.5 Flux pinning

In the mixed state of type II superconductor, transport current can drive flux lines into motion due to the Lorentz force given by $\vec{F} = \vec{J} \times \vec{B}$ where $\vec{F}$ is the force per unit volume. It is worth noting that a *perfect* type II superconductor without pinning, will not be able to carry any current without dissipation so the critical current density (J_c) is zero. Figure 2.8 shows the flux-line lattice, the direction of transport current and the resulting Lorentz force. Once pinning is overcome, flux line motion will create a voltage in the direction of transport current and thus produce a resistance so there is the dissipation of energy.

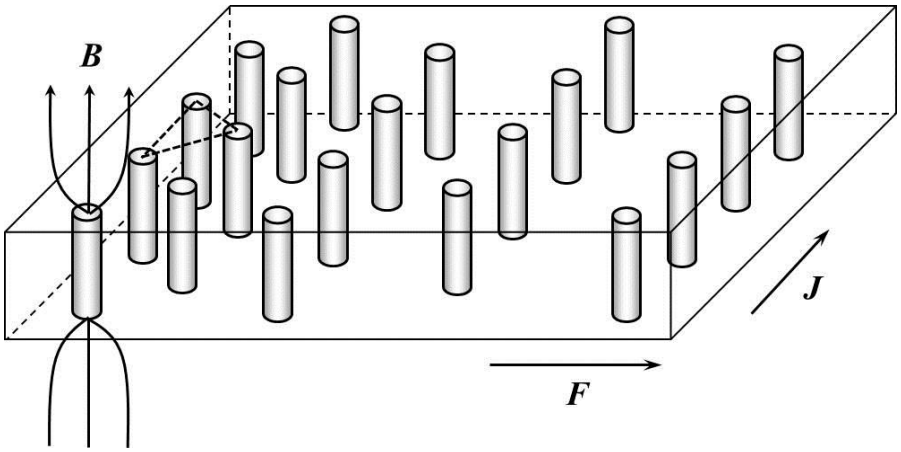

Figure 2.8 Flux lines in the mixed state of type II superconductor subject to the Lorentz force which is proportional to the current flow and drives flux lines into motion.

Defects in a dirty superconductor give rise to the local variation of the free energy and the vortices are trapped or *pinned* in the low-energy regions. These defects include non-superconducting particles, oxygen defects, cracks, dislocations and grain boundaries, which should have a dimension smaller than the coherence length for effective pinning. In order to move flux lines, an energy larger than the pinning energy or the Lorentz force larger than the pinning force must be used. The pinning force per unit volume is therefore given by $\vec{F}_p = \vec{J}_c \times \vec{B}$ which is found to follow the universal scaling law [56]:

$$F_p = \left[H_{c2}(T)\right]^{\nu} f'(\tilde{h}) \qquad (2.19)$$

where $\tilde{h}$ = H/H_{c2} is the reduced magnetic field strength. The exponent ν was originally found to be 2.5 but it could actually deviate from that value, depending on the temperature dependence of the Ginzburg-Landau parameter [57]. The shape of $f'(\tilde{h})$ was found to be sensitive to geometry of the pins although they exhibit a similar reduced-field dependence [58]. The reduced field $\tilde{h}_p$ at which the pinning

force is maximum occurs at high $\tilde{h}$ for weak (widely spaced) pinning superconductors and at low $\tilde{h}$ for the strong (closely spaced) pinning. However, the values of pinning force at high $\tilde{h}$ are not very different between weak pinning and strong pinning superconductors. Therefore, high-field critical current density has apparently limited scope for improvement. The critical current density, which is determined by the pinning force, is expressed as

$$J_c(\tilde{h},T) = \tilde{\Omega}[H_{c2}(T)]^{\nu}\tilde{h}^{p}(1-\tilde{h})^{q} \qquad (2.20)$$

where the constants $\tilde{\Omega}$, ν, p and q are dependent on geometry, strength and nature of the pinning. This last equation is the subject of much of the work in the later chapters of this thesis.

Chapter 3

High-temperature superconductivity

3.1 Introduction

It was not until ceramic copper oxide superconductor (Ba-La-Cu-O system) was discovered by Karl Müller and Johannes Bednorz in 1986 [5] that the transition temperature of a superconductor was found to be above 30 K and beyond the upper limit prediction of BCS theory. Higher T_c compounds in the same family were soon discovered with the T_c even higher than the boiling point of liquid nitrogen, making them recognised as high-temperature superconductors (HTS). This chapter provides general properties of various HTS materials, production techniques used to make them into a practical conductor and challenges in improving superconducting properties and understanding the mechanisms and processes behind making the superconductivity useful in these materials.

3.2 General properties

The most important property of HTS is the transition temperature above 30 K which is the upper limit predicted by BCS theory for conventional superconductors (cf Section 2.4). Therefore, the Cooper pairs in HTS are formed by different mechanism rather than phonon-mediated interaction. Table 3.1 shows transition temperature of some common known HTS materials. In early days of discovery, they were mostly

ceramic copper oxides (or cuprates) and the term cuprate superconductor was usually used to refer to HTS until iron-based superconductors were discovered in 2008. Included in the table are MgB_2, organic superconductors and heavy fermions with the T_c values that are not as high as the T_c of cuprates and iron-based superconductors and even below 30 K. They are considered as potential HTS materials (i.e. with potentially the same mechanism causing the superconductivity) because of their unconventional properties which are either similar to cuprates and iron-based superconductors, or basically just not predicted by the BCS theory.

HTS materials have type II magnetic response with high values of the upper critical field strength. When an applied magnetic field is between H_{c1} and H_{c2}, the field penetrates into material in the form of flux vortex. The vortices are trapped inside the (hard) superconductor when the field is removed and gives rise to an irreversible behaviour. This behaviour occurs up to the irreversible field (B_{irr}) before the magnetic flux can move reversibly ($J_c = 0$). To first order, irreversible line in the *B*-*T* phase diagram follows the vortex-lattice melting line which separates pinned vortex solid from unpinned vortex liquid [59]. For isotropic low-temperature superconductors (LTS), the vortex lattices are generally well pinned and the irreversible field is very close to their upper critical magnetic fields (B_{c2}). Figure 3.1 shows the *B*-*T* phase diagram of some superconductors, both LTS and HTS. For HTS, the effect of thermal fluctuation is strong and the vortices are soft. Irreversibility lines of MgB_2, YBCO and Bi-2223 are far below their upper critical magnetic fields and correlate with structural and electronic anisotropy of the materials. Bi-2223 has the highest degree of anisotropy so the vortex lattices are most likely to undulate. The irreversible field is very important in applications of HTS because it is the field (far below B_{c2}) at which the critical current density of the conductor becomes zero, even though it is still in the superconducting state.

Table 3.1 Symmetry of order parameter and typical values of transition temperature and upper critical magnetic field of high-temperature superconductors.

Material	Symmetry	T_c (K)	B_{c2} (T)		Ref.
			***c*-axis**	***ab*-plane**	
Copper oxide superconductors					
$(La,Ba)_2CuO_4$	*d*-wave	30			[5, 60]
$YBa_2Cu_4O_8$	*d*-wave	80	67 - 70		[60-62]
$YBa_2Cu_3O_7$	*d*-wave	93	120	250	[47, 63, 64]
$Bi_2Sr_2CuO_6$	*d*-wave	10	16 - 27	43	[60, 65, 66]
$Bi_2Sr_2CaCu_2O_8$	*d*-wave	85	> 60	> 250	[47, 65, 67]
$Bi_2Sr_2Ca_2Cu_3O_{10}$	*d*-wave	110	39	1210	[60, 65, 68]
$Tl_2Ba_2Ca_2Cu_3O_{10}$	*d*-wave	120	28	200	[60, 69, 70]
$HgBa_2Ca_2Cu_3O_8$	*d*-wave	133	108		[60, 71, 72]
Iron-based superconductors					
SmFeAs(O,F)	*s*(±)-wave	55	50 - 110	100 - 150	[73-75]
CeFeAs(O,F)	*s*(±)-wave	43	47	185	[73, 76, 77]
LaFeAs(O,F)	*s*(±)-wave	28	37.8	122	[73, 77, 78]
MgB_2	*s*-wave	39	3.5	17	[79-81]
Organic superconductors					
$(TMTSF)_2PF_6$ @ 12 kbar	*p*-wave	0.9	0.02		[43, 82]
κ-$(ET)_2Cu[N(CN)_2]Br$	*d*-wave	11.5	8 - 10	80	[70, 83, 84]
Cs_3C_{60} @ 15 kbar	*s*-wave	40			[85, 86]
Heavy fermions					
$CeCu_2Si_2$	*d*-wave	0.5	2.4	2.0	[87-89]
$CeCoIn_5$	*d*-wave	2.3	5.2	11.5	[90-92]
UPt_3	*p*-wave	0.5	2.6		[44, 93, 94]

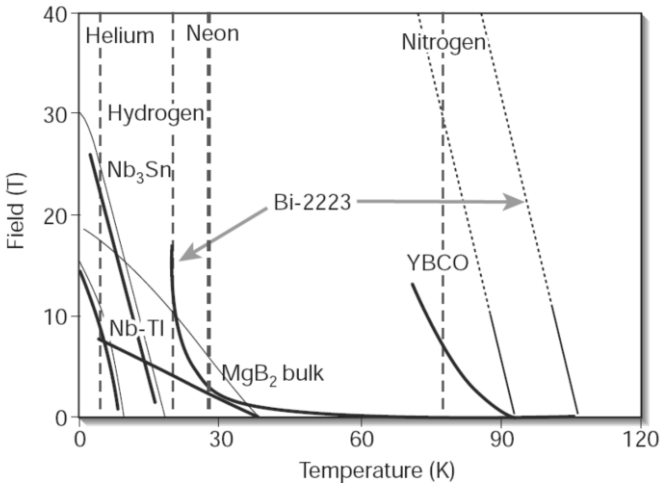

Figure 3.1 Magnetic field versus temperature phase diagram of some common HTS in comparison with some LTS [95]. The thick solid lines show irreversible fields. The thin ones show upper critical fields.

Most of the HTS are anisotropic and have layered structures, resulting in the anisotropy of their superconducting properties. The coherence lengths of the layered superconductors are typically short and superconductivity is confined in the two-dimensional plane. The HTS also usually exhibit the properties of unconventional pairing where the paring mechanism is still unknown. The following subsections provide information of general properties of some HTS groups previously shown in Table 3.1.

3.2.1 Cuprates

The term *cuprate superconductors* has been used since the discovery of LaBaCuO to refer to the HTS materials containing copper oxide (CuO_2) layers. There is a big family of them including the compounds of Y-Ba-Cu-O, Bi-Sr-Ca-Cu-O, Tl-Ba-Ca-Cu-O and Hg-Sr-Ca-Cu-O as summarised in Table 3.1. The key feature is superconducting CuO_2 layers which are weakly coupled along the *c*-axis and separated by charge reservoir layers. The parent compounds are typically Mott

insulators but become superconductors when doped with electrons (such as Nd-Ce-Cu-O, Pr-Ce-Cu-O, Sm-Ce-Cu-O and La-Pr-Ce-Cu-O compounds) or holes (such as Y-Ba-Cu-O, La-Sr-Cu-O and Bi-Sr-Ca-Cu-O compounds). Figure 3.2 shows doping dependent phase diagram of cuprate superconductors for hole doping ($La_{2-x}Sr_xCuO_4$) and electron doping ($Nd_{2-x}Ce_xCuO_4$). The superconducting phase only exists around optimal doping (between 0.1 and 0.2) where hole doping into the oxygen's *p*-orbitals in the CuO_2 plane breaks up antiferromagnetic order making the Cu^{2+} spins free to move and destroying the long-range antiferromagnetic correlations. The extra holes provide a vacancy for electron hopping and conductivity occurs.

For electron-doped materials, electrons are introduced to the copper's *d*-orbitals and the spinless Cu configuration dilutes the background antiferromagnetic order. Unlike hole-doped cuprates, the superconducting phase for electron doping exists at higher doping level and in narrower range. The antiferromagnetic phase is also very strong and still survives even when the doping level is close to the optimum. This can be explained by the dilution of Cu^{2+} spins which decreases the Néel temperature very slowly [96].

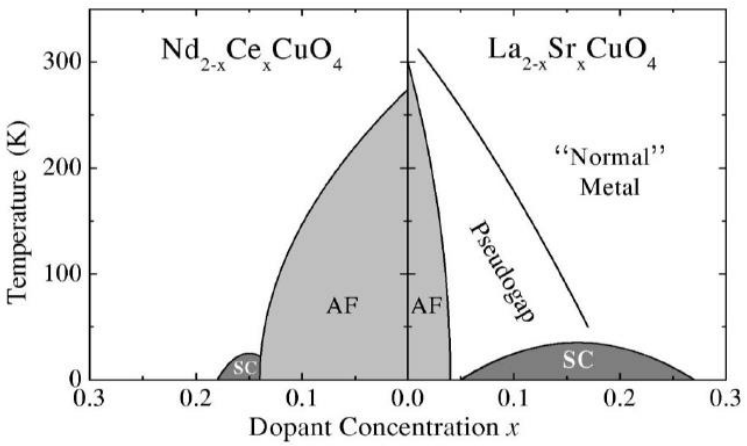

Figure 3.2 Doping dependent phase diagram of cuprate superconductors for electron doping (left) and hole doping (right) [97].

YBCO

Yttrium barium copper oxide or YBCO was discovered by Wu and his graduate students Ashburn and Torng, at the University of Alabama [63], only a year after the discovery of the first high T_c LaBaCuO. With the T_c of 93 K, it is the first material that becomes superconducting at the temperature above the boiling point of liquid nitrogen. This is very important since the cost of refrigerant for using these materials can be much lower. Figure 3.3 shows different crystal structures of YBCO; $YBa_2Cu_3O_7$ and $YBa_2Cu_3O_6$, both have orthorhombic perovskite-type structure consisting of two CuO_2 planes where the superconductivity takes place. The conductivity along the *ab*-plane is over 100 times higher than the conductivity along the *c*-axis. This may contribute to a single crystal having a J_c as high as 10^4 Acm^{-2} at 77 K [98] while the J_c of untextured polycrystalline sample is two orders of magnitude lower due to the existing of high-angle grain boundaries. It was reported that the intergrain J_c of YBCO is exponentially dependent on the grain orientation [6]. Therefore, controlling grain alignment has been found to be necessary in all techniques used to fabricate YBCO in order to achieve high critical current density. At present, the critical current density of epitaxial YBCO thin film (quasi-single crystal with pinning) is of the order of 10^6 Acm^{-2} at 77 K which is relatively high due to additional improvement of flux pinning.

BiSCCO

Bismuth-based superconducting material (bismuth strontium calcium copper oxide or BiSCCO) was discovered in Japan in 1988 by Maeda et al [99]. It was the first high temperature superconductor which does not include rare earth elements. With a higher critical temperature than that of YBCO, it has attracted much attention and has been developed continuously to enable its use in many applications. The generalised chemical compound BiSCCO has the form $Bi_2Sr_2Ca_{x-1}Cu_xO_{2x+4}$ with x = 1, 2 and 3 (the crystal structures are shown in Figure 3.3). The main difference

between them is the number of CuO_2 planes which is a factor determining T_c of BiSCCO. Commonly used high T_c phases are $Bi_2Sr_2CaCu_2O_8$ (Bi-2212) with the T_c of 85 K and $Bi_2Sr_2Ca_2Cu_3O_{10}$ (Bi-2223) with the T_c of 110 K.

Optimal doping for BiSCCO compounds is generally at 0.16 holes per Cu atom and the doping phase diagram follows parabolic curve $T_c / T_{cmax} = 1 - 82.6(y - 0.16)^2$ [100] where y is the number of holes per Cu atom. Partial substitution of Bi with Pb was found to improve the superconducting properties and increase the formation and stability of Bi-2223 phase which is difficult to grow [101, 102]. As a result, most of the Bi-2223 materials are now fabricated with Pb additions. They are usually made into conductors by the powder-in-tube method to solve the problem of their brittleness and also to improve the grain alignment (see Section 3.3.1).

BiSCCO has an even higher degree of structural and superconducting anisotropy than YBCO. The critical current density of a single crystal Bi-2223 is over 10^5 Acm^{-2} at 77 K [103] while the powder-in-tube polycrystalline tape achieves 10^4 Acm^{-2} which can be improved further by improvement of the grain alignment and homogeneity.

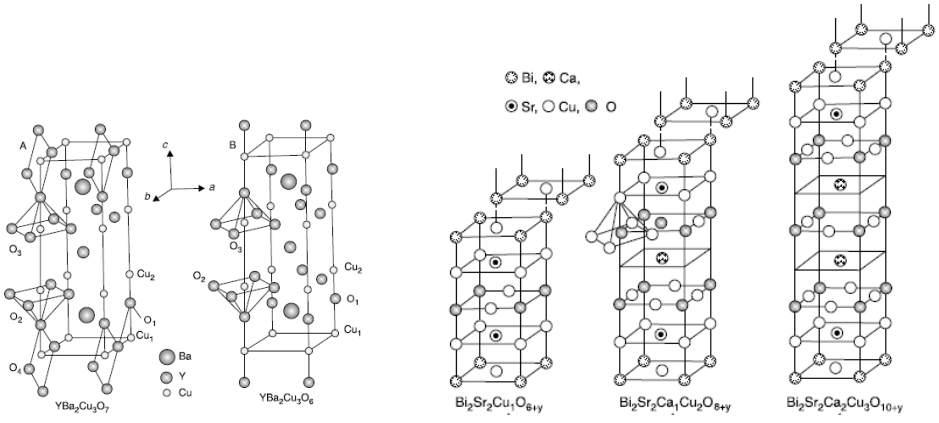

Figure 3.3 The crystal structures of YBCO and BiSCCO. YBCO has orthorhombic perovskite structure with two CuO_2 planes and perpendicular CuO chains. BiSCCO family has tetragonal structure with different number of CuO_2 planes for different phase members [104].

3.2.2 Iron-based superconductors

Iron-based superconductors or pnictide compounds are a new type of superconductor containing iron and pnictogen (group 15 element, typically arsenic and phosphorus). They were discovered in 2008 by Kamihara *et al* [105] who reported that LaOFeAs compounds became superconducting at a transition temperature up to 26 K when doping with F^- ions. Soon after the discovery, several pnictide superconductors were reported, such as FeSe, LiFeAs, $BaFe_2As_2$ and LiFeAsO. A T_c of over 50 K has been achieved either by doping or by pressure [106]. Figure 3.4 shows the doping dependent phase diagram of $CeFeAsO_{1-x}F_x$ with the existence of antiferromagnetic phase at low doping level as seen in the doping phase diagram of cuprates. There has been a rapidly increasing interest in these materials because they are the first known non-cuprate high T_c compounds that could help uncover the mystery behind the mechanism that causes superconductivity in the high-temperature superconductors.

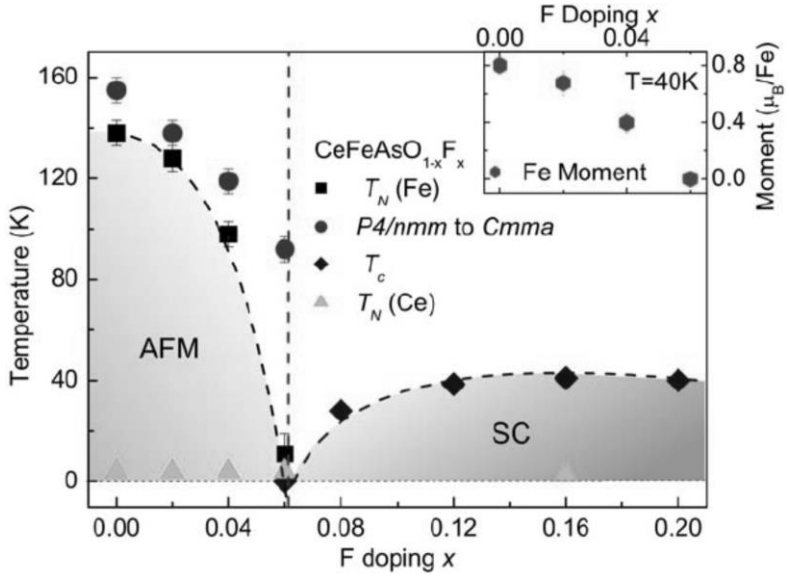

Figure 3.4 Doping dependent phase diagram of $CeFeAsO_{1-x}F_x$ iron-based superconductor determined from neutron measurements [107].

Like cuprates, iron-based superconductors have a layered structure but the iron and pnictogen plane (commonly FeAs) play an important role similar to the CuO_2 plane. The undoped parent compounds are poor metals with five conduction bands at the Fermi surface. The spins on the Fe atom have antiferromagnetic order and doping destroys the antiferromagnetism. This confirms the correlation between superconductivity and antiferromagnetism in HTS. Despite the similarity between them, pnictide compounds have a rather more complex electronic structure which leads to many unusual properties. For instance, the upper critical field shows nearly isotropic behaviour which arises from three-dimensional electronic structure of FeAs [108, 109]. Antiferromagnetism of the parent compound is a stripe-like pattern rather than checkerboard pattern due to alternation of Fe spins from one row to the other [110] and appears to incorporate spin-density-wave where electrons are delocalised [111].

3.2.3 Other unconventional superconductors

MgB_2

Magnesium diboride (MgB_2) is usually only included in the high-temperature superconductors for convenience since its T_c of 39 K can be explained by BCS theory. It is referred to as a conventional superconductor with the highest T_c among them because its structure and properties are closed to those of the low-temperature superconductors such as the isotope effect [112, 113], the large coherence length (ξ_{ab} ≈ 6.1 – 6.5 nm) [114] and temperature dependence of the upper critical field [115, 116]. However, electronic behaviour in MgB_2 is not as straightforward as in the conventional ones due to the two different band gaps at the Fermi energy which arises from different strengths of electron-phonon coupling in σ bands and π bands [117]. In addition, MgB_2 has graphite-type layered structure and T^2 temperature dependence of the penetration depth [118] which are characteristics of unconventional high T_c superconductors.

Although T_c of MgB_2 is about 2 - 3 times lower than the T_c of HTS, it is nevertheless a promising materials for applications (especially in high current, intermediate temperature and medium field applications) because it has lower anisotropy (Γ = 1.1 - 9) [114] and the grain boundaries do not limit the current flow [95, 119]. It is also relatively cheap and useful high J_c polycrystalline conductors can be fabricated in long lengths.

Organic superconductors

Most organic materials are electrically insulating. Nevertheless, some of them are not only conductive, but also exhibit superconductivity at low temperatures. Those materials include quasi one-dimensional and quasi two-dimensional salts such as Bechgaard salt $(TMTSF)_2PF_6$ and κ-$(BEDT\text{-}TTF)_2X$ (where BEDT-TTF is an organic molecule and X is an inorganic anion), alkali-doped fullerenes and carbon nanotubes. Bechgaard salts [82, 120] were the first organic superconductors synthesised by Klaus Bechgaard. It consists of stacked sheets of planar tetramethyltetraselenafulvalene (TMTSF) donors and monovalent anion acceptors PF_6. The conductivity of these charge transfer complexes occur only along the stacking axis where an intermolecular overlap of the π-orbitals takes place. The bigger molecule of bisethylenedithio-tetrathiafulvalene (BEDT-TTF or ET) in κ-$(BEDT\text{-}TTF)_2X$, consequently, allows packing with better orbital overlap between the stacks and provides quasi two-dimensional behaviour. Superconductivity in the alkali-doped fullerenes and carbon nanotubes, however, are different from those of charge transfer salts. Putting foreign molecules or atoms inside C_{60} leads to metallic crystals, while putting them between graphene sheets leads to ordered structures. The metallic crystals and ordered structure are eventually superconductors at low temperatures.

There is a special interest in organic superconductors not only because they are organic, but they also exhibit several common features with cuprates. κ-(BEDT-

TTF)$_2$X salts have layered structures, anisotropic electronic properties and pressure-dependent phase diagrams [121, 122]. Intensive studies of these molecular materials by tuning of their physical properties could provide a better understanding of electronic correlation in quasi two-dimensional superconductors.

Heavy fermion compounds

Heavy fermion superconductors are found in the metallic compounds based on Ce and U. The first one discovered was $CeCu_2Si_2$ with a T_c of 0.5 K [87]. The transition temperature of this type of superconductor is generally 1 - 2 K or less. However, their properties cannot be explained by the BCS theory. Competition between the Kondo effect (antiferromagnetic interaction between conduction electrons in metal and magnetic impurities) and the interaction between localised *f*-electrons and electrons in the other conduction band in the heavy fermion systems gives rise to a very large effective mass of the charged quasiparticles. This can be seen from specific heat (c_p) measurement near T_c [123]. The effective mass can be more than 100 times larger than the mass of bare electron [124] and results in the low-energy excitations. There is also evidence of a non *s*-wave pairing symmetry (existence of nodes in the energy gap from the power-law dependence of c_p below T_c) and interplay of spin fluctuations and electronic correlations with the pairing mechanism [125, 126].

3.3 Conductor technologies

HTS materials that can be used nowadays are mostly cuprates and they are brittle. Therefore, turning superconductors into a useful shape for applications is not easy. This is a major problem that can limit the use of them especially on the large scale. The most successful manufacturing of high-temperature superconductor is probably

the second generation superconducting tapes/wires based on YBCO coated conductors. However, the powder-in-tube processing under pressure is still important for Bi-based materials which are more difficult to grow and control phase homogeneity.

3.3.1 Powder-in-tube method

Powder-in-tube (PIT) method has been successfully used to fabricate the low T_c Nb_3Sn wires, MgB_2 wires, Bi-2212 wires and Bi-2223 tapes. The process starts with filling the powder of superconducting material into a metal tube then drawing into wire with smaller cross-sectional area. For multifilament conductor, a construction that helps improving strain tolerance [127], a number of wires are then assembled into an outer tube before the second stage drawing and final heat treatment are performed. Figure 3.5 shows manufacturing process of Bi-2223 wire via the PIT technique [128]. In manufacturing Bi-2223, the tubes are typically silver or silver alloy. Silver is not only permeable to oxygen and nonreactive to Bi-2223, it also plays an important role in encouraging the grain alignment of the plate-like orthorhombic Bi-2223 grains and reducing the melting point of Bi-2223. The result is Bi-2223 grains growing and aligning onto the silver interfaces with the *ab*-plane parallel to them [129]. Due to the anisotropic properties of Bi-2223 with weak coupling between layers, the round wire is eventually rolled into flat tape to enhance the grain alignment parallel to the tape surface.

Nevertheless, the silver sheathed Bi-2223 tapes produced by the early PIT method still faced some serious problems such as residual cracks, porosity and volume fraction of secondary phase occurring in the sintering process and ‘ballooning’ occurring from the gasification of the trapped liquid nitrogen during warming up to room temperature. In order to solve these problems and improve the quality of the tapes, the controlled overpressure sintering (CT-OP), a novel technique introduced in 2004, has been used [130, 131]. It improves the important properties of the tapes

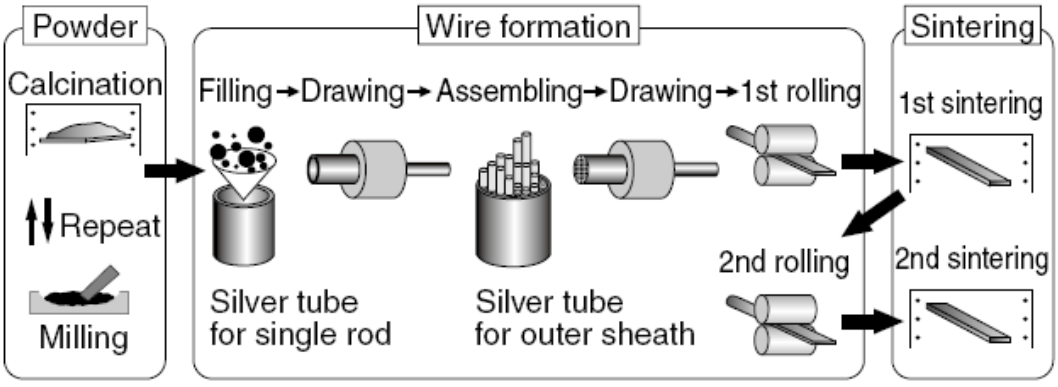

Figure 3.5 Bi-2223 wire manufacturing process with PIT technique [128].

such as the critical current density, *n*-value and mechanical strength resulting from the improvement of relative density, homogenisation and bonding strength between the grains [132, 133]. The densification also prevents liquid nitrogen penetration so no 'ballooning' occurs [134].

Bi-2223 tapes have been used successfully for the LHC current leads and power cable projects. The round wire of Bi-2212 is also a good candidate for cable-based magnets. However, the in-field performance of BiSCCO is not as good as YBCO and the production cost is quite high due to the cost of silver. In response to the application and economical concerns, coated conductors based on YBCO have been developed.

3.3.2 Coated conductor

Architecture of the YBCO coated conductors is totally different from the PIT conductors. The coated conductor production involves preparing textured substrate (as a template) and deposition of YBCO material. The textured template can be achieved either by ion beam assisted deposition (IBAD) process or rolling-assisted biaxial textured substrate (RABiTS) technique. Polycrystalline YBCO

superconductor is then deposited epitaxially by metal organic chemical vapour deposition (MOCVD) onto the template followed by deposition of stabilising layers.

Figure 3.6 demonstrates manufacturing process of YBCO coated conductors by IBAD and RABiTS techniques. IBAD has been used by SuperPower to sputter a stack of buffer layers on polished hastelloy-based substrate [135] while RABiTS has been used by American Superconductor Corporation (AMSC) to form biaxially orientated nickel substrate using thermomechanical processing [136]. The YBCO tape produced by the coated conductor technique is strongly aligned with the *ab*-plane parallel to the tape surface. There exist only low-angle grain boundaries in the structure providing the high value of critical current density. Although the production cost is not low, good in-field performance even at high temperature (above 77 K) and high mechanical strength means that YBCO coated conductors have become preferable for use in cable, magnet and coil applications.

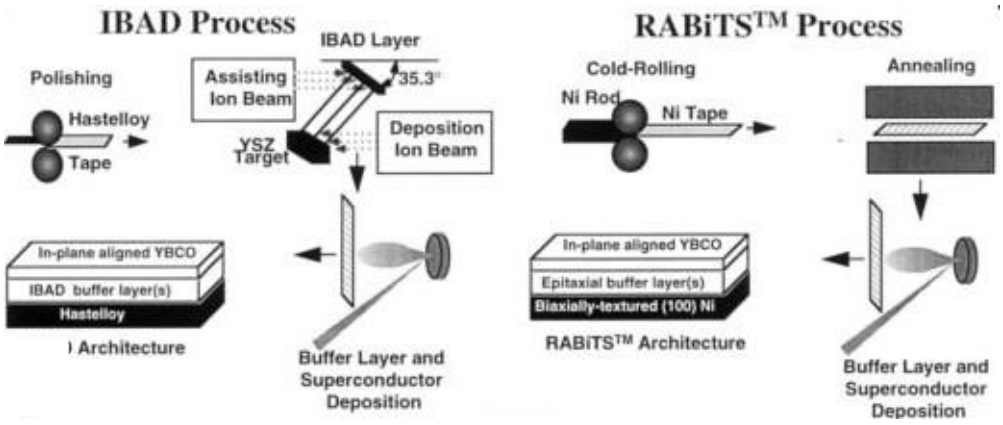

Figure 3.6 Coated conductor manufacturing process where the textured substrates are prepared by IBAD (left) and RABiTS (right) [137].

3.4 Challenges in HTS

3.4.1 Pairing mechanisms

After much intensive research on many HTS materials, many common features in their properties have been found, yet there is no widely accepted theory to explain their properties. One example of data that need explanation is Uemura's muon-spin-relaxation measurements (μSR) data [138, 139] on various systems such as bismuthate (BKBO), cuprates, heavy fermions and Chevrel-phase compounds. The plots of T_c versus relaxation rate (which is proportional to the ratio between carrier density and effective mass) in these systems are similar. The T_c initially increases with increasing relaxation rate, shows saturation and then suppression in higher-carrier regions as shown in Figure 3.7. They also have relatively high upper critical field, short coherence length and highly correlated electronic structures. These features suggest that the systems possibly share a common condensation mechanism and/or thermodynamic description which is not consistent with the BCS theory.

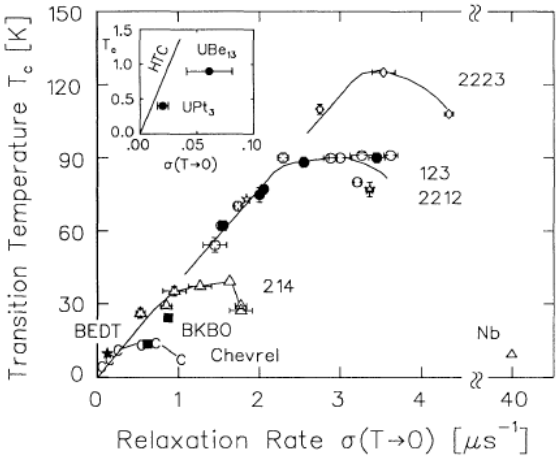

Figure 3.7 Plot of T_c versus relaxation rate of cuprates, BKBO (solid squares), Chevrel-phase (C) and BEDT (solid star) systems based on μSR measurements; and of Nb and heavy fermion systems (inset) with the values of relaxation rate estimated from the bulk penetration depth measurements [140].

There have been many studies on the coexistence of high-temperature superconductivity and magnetic ordering. In the copper oxide compounds, the magnetic ordering is antiferromagnetic from Cu^{2+} spins in the CuO_2 layers. Normally, the copper ion has one hole with spin ½ in the 3*d* shell. A strong interaction between the hole spins gives rise to three-dimensional long-range antiferromagnetic order with a high value of Néel temperature. The long-range order disappears in the metallic and superconducting phases but some strong dynamical spin fluctuations with a wide spectrum of excitations are still observed even at temperatures above 100 K [141]. This has led to a number of hypotheses on magnetic mechanisms of superconductivity and it has been found that antiferromagnetic spin fluctuations may be vitally important in explaining many of the anomalous properties of the HTS in the normal phase [142]. Other possibilities include interlayer tunnelling mechanism, where superconductivity within the layers of a layered superconductor is explained by BCS theory and superconductivity between layers results from tunnelling of the Cooper pairs [143]. At present, the exact mechanism that causes the electrons to form pairs in HTS is still unclear. Some experimental results support the importance of *d*-wave pairing while others support the *s*-wave symmetry. The question of how superconductivity arises in the HTS is still one of the major ongoing research in this field.

3.4.2 Superconducting properties and applications

Superconducting properties, such as critical temperature, upper critical magnetic field, critical current density and mechanical tolerance are important factors determining the quality and use of superconductors. For the LTS, understanding in many aspects of these properties has been established. The *J*-*B*-*T* critical surface phase diagram and reversible strain effect have been revealed and understood. This has been a key success that provided appropriate strategies for improving their superconducting properties and thus optimised their use in applications. Table 3.2

shows conductor performance requirements for various applications [95]. In addition to magnetic field, temperature and current density, the superconductors should be able to be made into a minimum length, withstand the strain limit provided and deform up to a minimum bending radius. For the HTS, an advantage over the LTS is the lower cooling cost due to higher operating temperature. Fundamentally, T_c at ambient pressure can be improved by doping which should in turn improve B_{c2} and make the superconductor usable over a larger phase space.

The critical current density or the current carrying capacity of superconductors, on the other hand, is traditionally considered to be affected by flux pinning. In order to improve the intra-grain J_c, effective defects must be introduced. In YBCO, artificial columnar defects have been introduced into the system (in addition to natural dislocation defects) by various techniques such as irradiation and substrate decoration with nano-particles [144-146]. J_c has been increased to 10^6 Acm^{-2} and even larger where the grain alignment is well controlled. This increase in pinning approach has successfully been used for the LTS such as Nb_3Sn where fabrication techniques have been adjusted to reduce the grain size, so increase the number of grain boundaries which act as pinning centres [147]. However, this is not the case for HTS. Grain boundaries in YBCO were found to limit the current flow [6, 148] and to date we have avoided making high J_c polycrystalline HTS. A model based on flux flow along the grain boundaries is presented in Chapter 6 which could provide insight into the critical current density in polycrystalline superconductors and thus lead to possible improvement.

Brittleness and J_c degradation under strain for HTS cuprates might be overcome by introducing other metallic layers into the wire architecture of superconductors. For BiSCCO in particular (and reported in Chapter 4), irreversible degradation has been found in compression [149, 150]. The reason behind this behaviour is still unclear but remains important because superconductors unavoidably experience the compressive strains in applications.

Table 3.2 Requirements of conductor's performance for various applications [95].

Application	J_c **(Acm^{-2})**	***B* (T)**	***T* (K)**	**Length (m)**	**Maximum Strain (%)**	**Minimum bend radius (m)**
Fault current limiter	10^4 - 10^5	0.1 - 3	20 - 77	1000	0.2	0.1
Large motor	10^5	4 - 5	20 - 77	1000	0.2 - 0.3	0.05
Generator	10^5	4 - 5	20 - 50	1000	0.2	0.1
SMES	10^5	5 - 10	20 - 77	1000	0.2	1
Transmission cable	10^4 - 10^5	< 0.2	65 - 77	100	0.4	2
Transformer	10^5	0.1 - 0.5	65 - 77	1000	0.2	1

Enabling the use of iron-based superconductors and other high-T_c materials is another challenge in HTS. We are in very early stage of iron-based superconductors since they were just discovered in 2008 and there exist many aspects to improve and understand. However, the number of studies on iron-based superconductors has increased rapidly. So far the PIT pnictide wires of the 122 type ($BaFe_2As_2$ series) have been made with the in-field J_c of 10^4 Acm^{-2} at 4.2 K and 10 T [151] which makes it a very good candidate for high-field applications. In response to concerns of toxicity of arsenic, iron-based superconductors containing less-toxic elements such as phosphorus and selenium have also been studied. A T_c of about 10 K has been obtained for FeSe wires with the J_c of 10^1 - 10^2 Acm^{-2} at 4.2 K and 10 T [152], two orders of magnitude lower than the J_c of the 122-type wires. Further improvement of FeSe conductors and also the search for a new class of iron-based superconductors without toxicity problem are still challenging.

3.5 Concluding comments

It has been more than 25 years since the discovery of high-temperature superconductors. They activated the search for a new pairing mechanism since the electron-phonon interaction, found in the BCS-type conventional superconductors, did not appear to explain the new materials. Although the new mechanism is believed to involve magnetic interactions, it is still not certain. Despite the uncertainty in the theoretical models, new classes of superconductors have been continuously discovered and the superconducting properties and fabrication techniques of HTS have been studied and successfully improved. Although the use of HTS is not as prevalent as LTS at the moment, these continuous studies could change this in the near future.

Chapter 4

Preliminary measurements on DI-BiSCCO tapes

4.1 Introduction

This chapter provides general description of the BiSCCO tapes (the main material studied in this thesis) supplied by Sumitomo Electric Industries (SEI). The critical current density, which is a key property of the tapes, was measured as a function of magnetic field, field orientation and strain. Preliminary results of the J_c measurements are presented in this chapter that led to two conference papers [153, 154] which includes the field, angle and strain effects on BiSCCO (predominantly 77 K measurements). The development of the probes that followed this work is shown in Chapter 5 and the more comprehensive data obtained in subsequent chapters. This chapter describes a simple model and explanation of the J_c results which provides a basic understanding of the properties of BiSCCO.

4.2 DI-BiSCCO samples

The so-called Drastically Innovative Bi-2223 superconducting tapes (DI-BiSCCO) have been developed by Sumitomo Electric Industries (SEI) using the powder-in-tube (PIT) process together with the controlled overpressure (CT-OP) technique at the final heat treatment. It was shown that the critical current (I_c) was enhanced by more than 60 %, the critical tensile stress improved by more than 70 % and no

ballooning was found in the full length of several kilometre-long DI-BiSCCO tapes after 24 hours immersion in liquid nitrogen [155, 156]. The critical current has recently been increased to more than 200 A at 77 K and self-field [131, 157, 158].

Nevertheless, high critical current alone does not satisfy all the needs of most applications. High mechanical strength and low ac losses are also important. For this reason, SEI has manufactured multifilamentary DI-BiSCCO tapes with various geometries. *Type H* has the same structure as the conventional wire with higher critical current. *Type S* is manufactured with a half cross-sectional area of type H while maintaining the engineering critical current density (J_e). It has been developed for low operating current applications. *Type HT* and *type ST* are the high strength tapes made by reinforcing type H and type S tapes with metallic lamination layers such as stainless steel and copper alloy. The lamination produces a higher reversible strain limit which is a result of increased compressive residual strain exerted on the filaments (due to difference in the coefficients of thermal expansion of various components in the laminated composite) and suppressed fracture of the superconducting filaments [159, 160]. Strengthening the tapes with the metallic laminations is very helpful for high field applications where the Lorentz force creates stress within the tapes. In addition, SEI has also produced *type AC* tapes for ac uses. It has been made by subdividing the superconducting filaments and shortening the twist pitch of the filaments to make the hysteresis loop smaller and reduce the coupling losses [131]. Typical specifications of the DI-BiSCCO type H and type HT tapes which are used in this work are shown in Table 4.1. Although most of the superconducting properties shown here are at 77 K, the high field performance of the tapes at low temperatures has also been investigated [157, 161]. The critical current of a 200A-class DI-BiSCCO tapes (I_c = 200 A at 77 K and self-field) is 430 A at 4.2 K and 12 T, and is up to over 600 A at lower fields [157]. The tapes have anisotropic critical current which is likely to be larger when the grain alignment is improved [162, 163].

Table 4.1 Typical specifications of the DI-BiSCCO type H and type HT tapes.

Item	Specifications	
	Type H	**Type HT**
Width (average)	4.3 ± 0.3 mm	4.5 ± 0.3 mm
Thickness (average)	0.23 ± 0.03 mm	0.30 and 0.36 ± 0.04 mm
Critical current [a]	160 - 200 A	160 - 200 A
Lamination	No	Yes
Critical wire tension (RT) [b]	80 N	230 - 280 N
Critical tensile strength (77 K) [b]	130 MPa	250 - 270 MPa
Critical tensile strain (77 K) [b]	0.2 %	0.3 - 0.4 %
Critical double bend diameter (RT) [b]	70 mm	60 mm

[a] 100 μVm^{-1}, 77 K and self-field, end-to-end

[b] 95 % I_c retention

The DI-BiSCCO tapes used in this work are of XM375 series. Their descriptions are summarised in Table 4.2. The samples are called bare, SS20, Ag20 and CA50 for type H tape, type HT tapes with 20-μm stainless steel, 20-μm copper-silver alloy and 50-μm copper alloy laminations, respectively. A transverse cross-section of a DI-BiSCCO SS20 tape is shown using scanning electron microscope (SEM) image in Figure 4.1 where the outermost layers (dark grey) are stainless steel laminations which were soldered directly onto the standard bare tape.

Table 4.2 Description of XM375 series DI-BiSCCO tapes.

Sample	Type	Average width (mm)	Average thickness (mm)	Lamination	
				Material	Thickness (μm)
1. Bare	H	4.3 ± 0.3	0.23 ± 0.03	-	-
2. SS20	HT	4.5 ± 0.3	0.30 ± 0.04	Stainless steel	20
3. Ag20	HT	4.5 ± 0.3	0.30 ± 0.04	Cu-Ag alloy	20
4. CA50	HT	4.5 ± 0.3	0.36 ± 0.04	Cu alloy	50

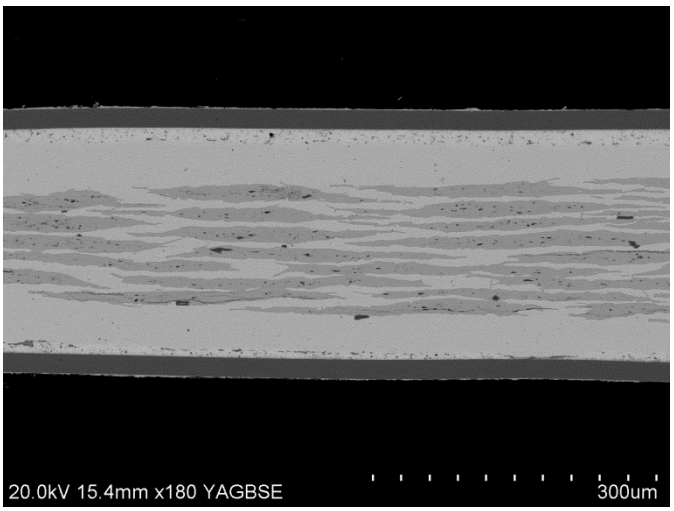

Figure 4.1 SEM image of the transverse cross-section of a DI-BiSCCO SS20 tape. The tape consists of (in order, from outer surface) stainless steel lamination layers (dark grey), solder layers (light grey with black spots), silver/silver alloy matrix (light grey) and BiSCCO filaments.

4.3 Experimental methods

Critical current measurements on the tapes were carried out using a standard four-terminal technique and the critical currents were determined using a 100 μVm^{-1} electric field criterion. In the measurements, a computer interface was used to control the 2000 A sample power supply and collect the electric field versus current data. The current from the power supply passed through a standard resistor for direct measurements of the sample current. The split-current-lead design was implemented and used - as discussed in Chapter 5 on probe design. This ensures that to first order: the magnetic field produced by the current in the leads is minimised at the tape position and hence the tape only experiences the magnetic field from the magnet and its own self-field; the torque associated with currents flowing in the leads and the sample is minimised so the probe should not progressively twist (or rotate) while the current is increasing during the measurement [153].

All critical current densities in this chapter were calculated using the critical current divided by the unstrained cross-sectional area of the superconducting filaments which was estimated from SEM images taken in Durham to be 4.8×10^{-7} m^2. The measurements were performed at 77 K in a conventional iron-cored electromagnet in magnetic fields up to 0.7 T and at 4.2 K in the 15 T horizontal superconducting split-pair magnet at different angles (θ) between the field and the tape surface. For strain measurements, the tapes were mounted on a springboard-shaped copper beryllium sample holder, which is attached at one end to a moveable stainless steel tube and has another end locked by a stationary support outer tube. The compressive and tensile strains were applied to the tapes by pushing or pulling the inner tube. The strains were measured with a Vishay strain gauge attached on the surface of the sample holder. Schematic of the experimental apparatus for the strain measurements is shown in Chapter 5.

In addition, an HGCT-3020 Hall sensor from Lake Shore Cryogenic, Inc. was used to align the probe in a required orientation with respect to the magnetic field and to investigate whether the sample rotated during the J_c measurement while the top of the probe was fixed. The sensor was attached directly on to the sample and the component of the magnetic field normal to the sample surface was monitored. The sensor has the maximum linearity error of ±1.0 % for fields less than 3 T and ±2.0 % for fields up to 15 T.

4.4 Experimental results

4.4.1 Magnetic field dependence of J_c

Figure 4.2 and Figure 4.3 show electric field versus current characteristics of a DI-BiSCCO CA50 tape at 77 K as a function of magnetic field applied normal and parallel to the tape surface. The critical current determined at a 100 μVm^{-1} electric field criterion at the transition is 174.5 A in self-field. The applied magnetic fields reduce the current carrying capacity of the tape. The effect of the magnetic field on the critical current is stronger when the field is applied normal to the tape surface. Figure 4.4 shows the critical current density of the DI-BiSCCO CA50 tape at 77 K as a function of magnetic field applied at different orientations with respect to the flat surface of the tape. Those orientations include 0° (field parallel to the tape surface), 30°, 60° and 90° (field normal to the tape surface). The very weak field-dependence for the critical current density occurs in magnetic fields less than 0.1 T parallel to the tape surface when the self-field generated from the current flowing in the tape is larger than the external magnetic field.

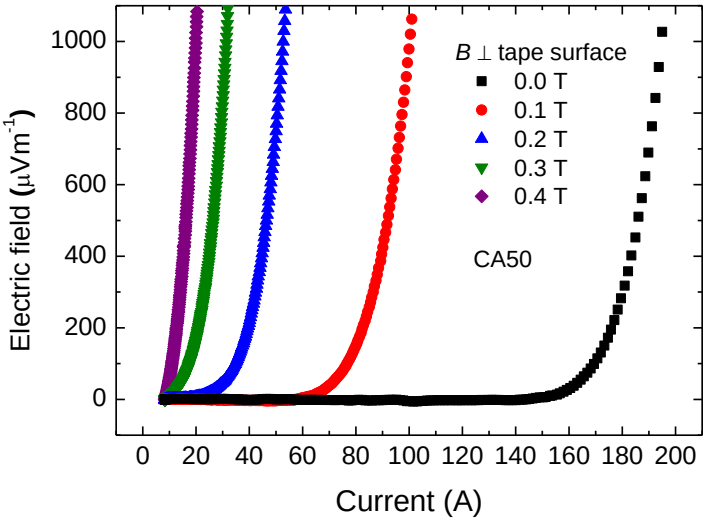

Figure 4.2 Electric field versus current as a function of applied magnetic field normal to the tape surface for the DI-BiSCCO CA50 tape at 77 K.

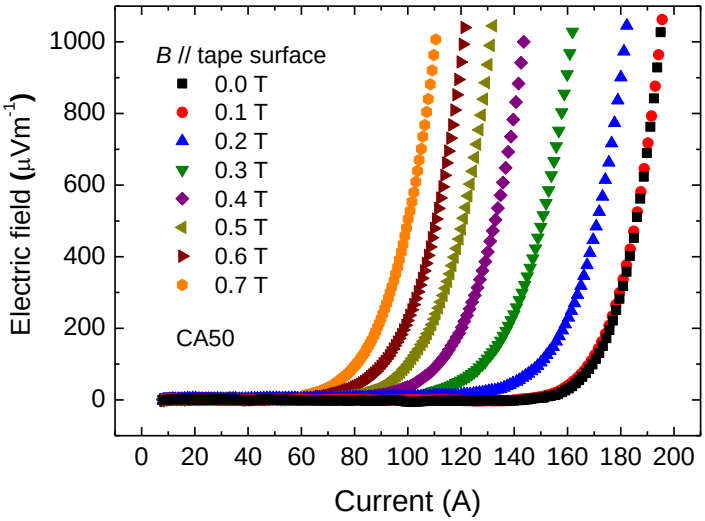

Figure 4.3 Electric field versus current as a function of applied magnetic field parallel to the tape surface for the DI-BiSCCO CA50 tape at 77 K.

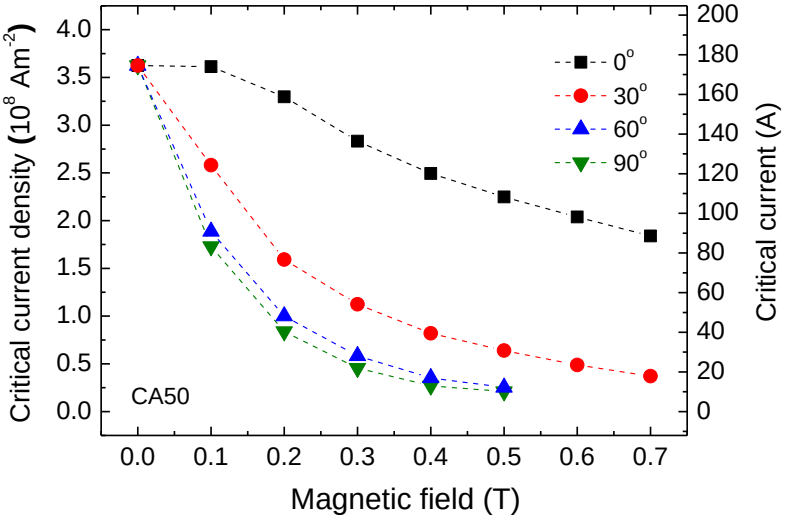

Figure 4.4 Critical current density as a function of applied magnetic field at different orientations for the DI-BiSCCO CA50 tape at 77 K. The critical current density decreases more drastically when the fields are applied normal to the tape surface.

4.4.2 Angular dependence of J_c

The anisotropic properties of the DI-BiSCCO CA50 tape are shown in Figure 4.4, with more detail shown in Figure 4.5. The results from the other three samples are similar. J_c is maximum when the field is applied parallel to the tape surface because of the intrinsic pinning associated with the CuO_2 planes and the higher upper critical field [21, 164]. The intrinsic peaks are shown clearly in Figure 4.5 for magnetic fields up to 0.7 T at 77 K. The in-field decrease of J_c (at any orientation) can be explained by the effect of the local component of magnetic field along the *c*-axis ($B\sin\theta$ - assuming all grains are well aligned with *ab*-plane // tape surface), given BiSCCO has strong two-dimensional (2D) properties [165]. Definitions of the field angle and grain misalignment (as discussed below) are illustrated in Figure 4.6.

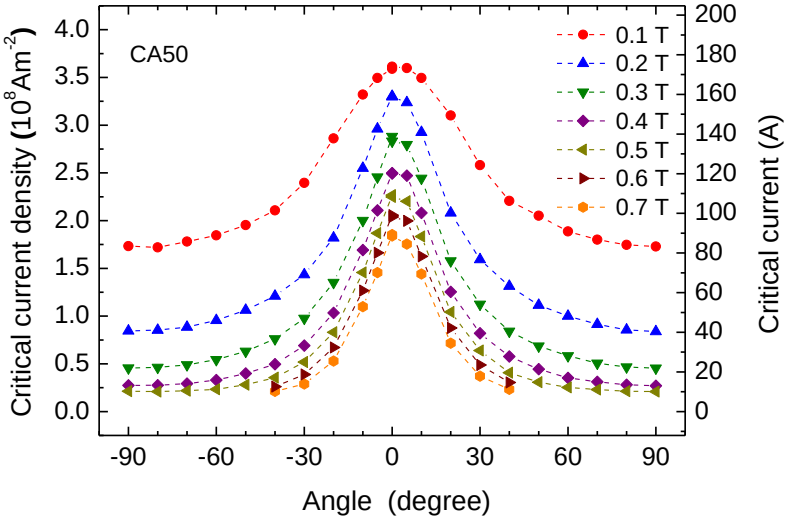

Figure 4.5 Critical current density as a function of the angle between applied magnetic field and the surface of the DI-BiSCCO CA50 tape at 77 K at different applied magnetic fields.

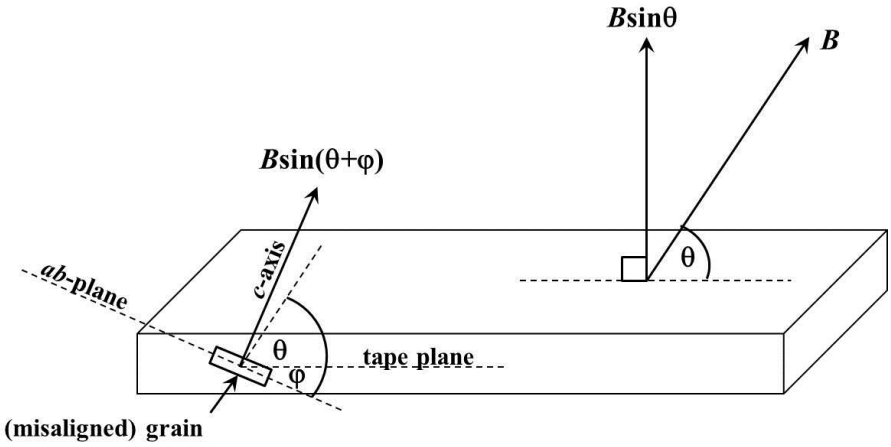

Figure 4.6 Definitions of the field angle, misalignment angle of a local grain in the DI-BiSCCO tape and normal component of magnetic field.

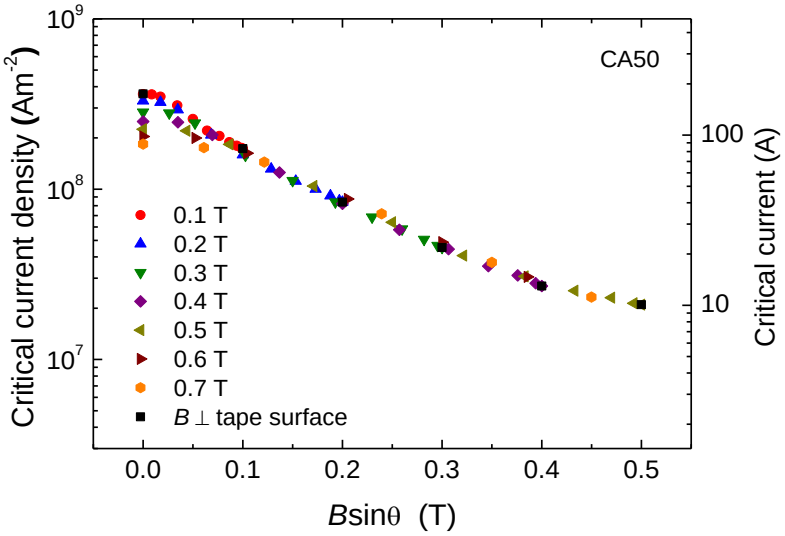

Figure 4.7 Critical current density as a function of the field component normal to the surface (Bsinθ) of the DI-BiSCCO CA50 tape at 77 K. Data for the field applied normal to the tape surface are made more explicit for clarity. Deviation from the universal relation occurs at low fields due to the grain misalignment.

Figure 4.7 shows J_c of the tape as a function of Bsinθ. Data for the field applied normal to the tape surface are made more explicit for clarity. J_c(Bsinθ) coincides with the data set of J_c(B ⊥ tape surface) in high fields but deviates from that in low fields, consistent with the importance of the grain misalignment [166, 167]. DI-BiSCCO tapes produced by the PIT technique generally contains grains that are misaligned from the desirable *ab*-plane // tape surface alignment. As shown in Figure 4.1, the BiSCCO filament itself is not uniform and the interface between BiSCCO and silver matrix is not always parallel to the tape surface. As a result, some grains are misorientated.

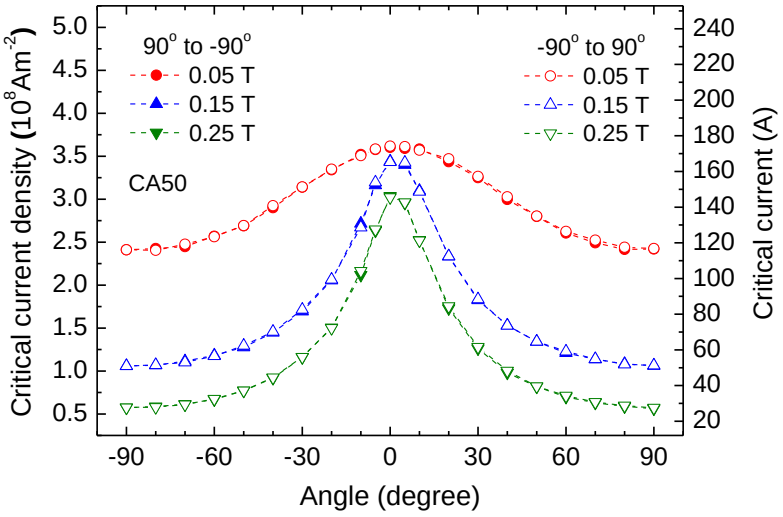

Figure 4.8 Critical current density as a function of the angle between applied magnetic field and the surface of the DI-BiSCCO CA50 tape at 77 K at two different directions of changing the angle. No angular hysteresis was observed.

Figure 4.8 shows the angular dependence of J_c for two different directions of changing the angle (from 90° to -90° and from -90° to 90°). No hysteretic behaviour was observed in the DI-BiSCCO CA50 tape (and also in three other tapes measured). The angular hysteresis is typically found in low fields and low temperatures (thus high critical current density) [168, 169] from trapping of magnetic flux around the grain boundaries. The magnetic fields and temperatures here are not low enough to see such effect.

The work of van der Meer *et al* considers a Gaussian distribution function to describe the grain misalignment of the form [166]:

$$G(\varphi) = \frac{1}{\sigma_{2D}\sqrt{2\pi}} \exp\left(\frac{-\varphi^2}{2\sigma_{2D}^2}\right) \qquad (4.1)$$

where σ_{2D} is the standard deviation of misalignment angle (subscript 2D denotes the assumed 2D properties of BiSCCO). This distribution accounts for a small angle

between the tape surface and the local *ab*-plane of the grains within the tape. $G(\varphi)d\varphi$ is the fraction of grains that have a misalignment angle between φ and $d\varphi$ where $-90° \le \varphi < 90°$. If a magnetic field is applied at an angle θ with respect to the tape surface and the grains locally have a misalignment angle φ, the local orientation of the magnetic field with respect to the *ab*-plane becomes $\theta + \varphi$. As a result, the local magnetic field parallel to the *c*-axis is $B\sin(\theta + \varphi)$ as shown in Figure 4.6. The average magnetic field normal to the *ab*-plane is

$$B_{\perp}(\theta) = B\int_{-90°}^{90°} G(\varphi)\left|\sin(\theta+\varphi)\right|d\varphi. \qquad (4.2)$$

Shevchenko [170] introduced a scaling function $f(\theta)$ by normalising $B_{\perp}(\theta)$ with respect to $B_{\perp}(90°)$ which is independent on magnitude of the magnetic field. For any magnetic field applied at an angle θ with respect to the tape surface, the scaled field amplitude of the effective normal magnetic field (B_{eff}) is written as $B \times f(\theta)$. Therefore, $f(\theta)$ is the corrected version of $\sin\theta$ that includes the grain misalignment. The value of $f(0°)$ is determined from the experimental results where J_c is a function of magnetic field at the angles 0° and 90° by using the relation $J_c(B,0°) = J_c(B \times f(0°),90°)$. The value of σ_{2D} is then calculated using [166]

$$\sigma_{2D} = 70.9 f(0°), \qquad (4.3)$$

which is accurate to 1 % and is in principle not dependent on the magnetic field [166]. Figure 4.9 shows the calculated values of σ_{2D} for the four different types of the DI-BiSCCO tapes measured. The scaling function $f(\theta)$ for any given θ is then obtained using the calculated σ_{2D} from (4.3), which is 12° for the Ag20 tape, 10° for the SS20 tape, 9° for the CA50 tape and 9° for the bare tape. Figure 4.10 shows $f(\theta)$ for the four samples which is generally equal to $\sin\theta$ except for $\theta < 20°$ where a tail appears. The tail is due to the misalignment of the grains - the larger misalignment, the larger the deviation from the $\sin\theta$ function.

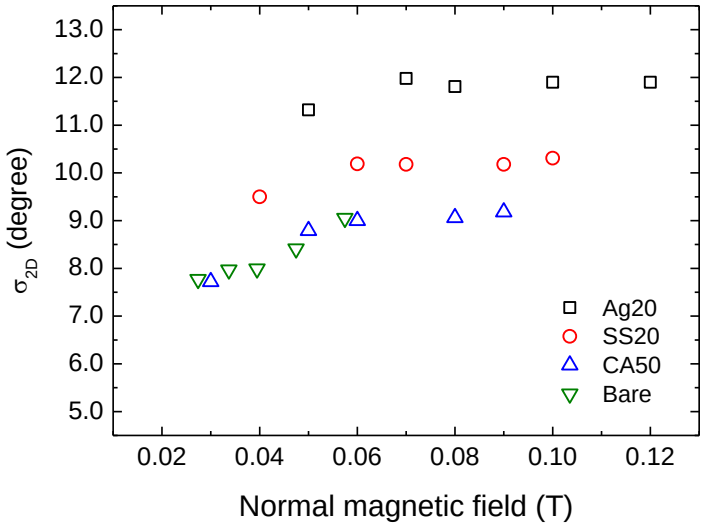

Figure 4.9 Standard deviation of the misalignment angle as a function of magnetic field normal to the tape surface for four different types of the DI-BiSCCO tapes. To first order, the standard deviation is not dependent on magnetic field.

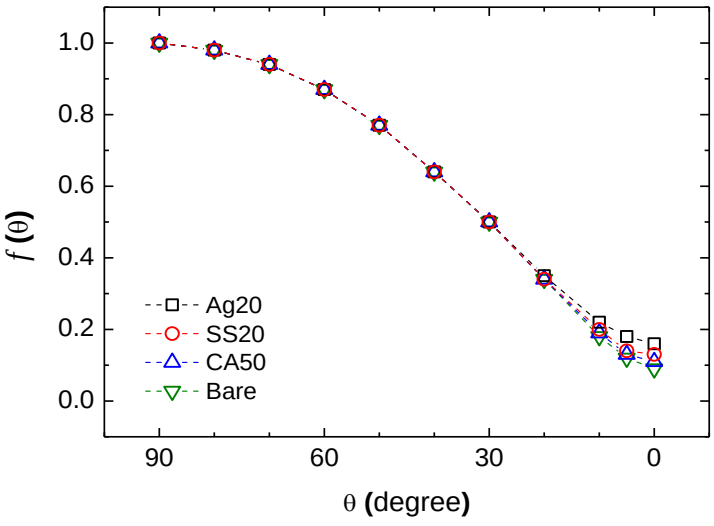

Figure 4.10 The scaling function $f(\theta)$ for four different types of the DI-BiSCCO tapes calculated by normalising $B_{\perp}(\theta)$ with respect to $B_{\perp}(90°)$. The scaling function generally follows sinθ except at the low angles ($\theta < 20°$).

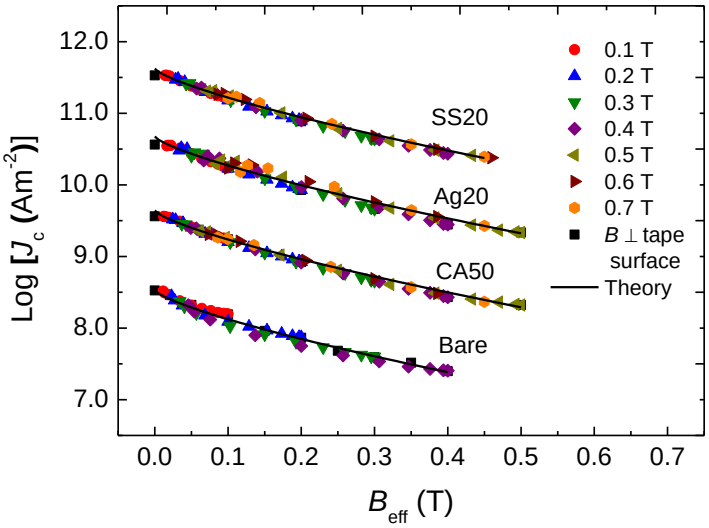

Figure 4.11 Critical current density as a function of the effective normal magnetic field for the DI-BiSCCO tapes at 77 K. The data for each tape are increased sequentially by 1 from the bare tape for clarity. Solid lines are plots of (4.4).

Figure 4.11 shows J_c for the DI-BiSCCO tapes as a function of the effective normal magnetic field $B \times f(\theta)$ at 77 K. The log(J_c) data of CA50, Ag20 and SS20 tapes are increased sequentially by 1 from the bare tape for clarity. The deviation, associated with the grain misalignment seen in Figure 4.7 in the low field region has disappeared and the J_c can be described using a rather simple model derived for polycrystalline superconductors [171]:

$$J_c(B,T,\theta) = \alpha'(T)\left(1-\frac{B_{\text{eff}}(\theta)}{B_{c2}(T,\varepsilon_a=0,\theta=90°)}\right) \times \exp\left[-\left(\frac{B_{\text{eff}}(\theta)}{\beta'(T,\varepsilon_a=0,\theta=90°)}\right)^k\right] \quad (4.4)$$

where the parameter k is added to account for the non-exponential behaviour at low fields, ε_a is the applied strain, α' is a parameter representing the depairing current density and β' characterises the suppression of the order parameter by the magnetic

field across the grain boundaries. A more sophisticated model to analyse such data is presented in Chapter 6. Equation (4.4) accounts for the reduction in the depairing current density due to the depression of the order parameter by the magnetic field at the grain boundaries and the suppression of the order parameter within the grains themselves [171]. Solid lines in Figure 4.11 are plots of (4.4) with the parameters β´ = 0.11 T and k = 0.75. $\alpha'(T = 77\,\mathrm{K})$ varies from sample to sample and is 4.2×10^{8} Am^{-2} for the SS20 tape, 4.7×10^{8} Am^{-2} for the Ag20 tape, 4.4×10^{8} Am^{-2} for the CA50 tape and 3.4×10^{8} Am^{-2} for the bare tape. Empirically we have found that the value of B_{c2} is much higher than B_{eff} consistent with significant depression of the order parameter across the grains [172].

4.4.3 Strain dependence of J_c

Preliminary data showing the variation in the J_c caused by the tensile and compressive strains are shown in Figure 4.12 for the DI-BiSCCO CA50 tape at 77 K at different magnetic fields applied normal to the tape surface. The J_c-strain characteristics for different fields are similar. The strain was initially applied in tension causing the J_c to reduce reversibly. This behaviour in Bi-2223 superconducting tapes in zero field at 77 K has been reported before [159, 160, 173]. Note that the measurements in this work were performed up to 0.2 % in tension to ensure that the tensile strain was below the critical limit of 0.3 % for the CA50 tape and prevent the tape from being damaged.

Figure 4.13 shows the strain dependence of J_c for the DI-BiSCCO CA50 tape at 77 K for zero field alone and Figure 4.14 shows the data at 4.2 K for applied magnetic field of 10 T. Both data sets show similar behaviour namely that initially although J_c is reversible in tension (below the critical strain limit), there is no reversibility in compression (compressive strains larger than 0.1 %). On applying increased compression there is an irreversible degradation. Thereafter on reducing the compressive strain, one finds an increased reversible range stretching over both

tensile and compressive strains. Figure 4.13 and Figure 4.14 each show three different reversible ranges. Note that (a new) reversibility in tension still occurs after degradation of J_c and that the reversibility is extended into the compressive regime. In the reversible strain regime the variation in the normalised J_c with respect to the strain is linear, both at 77 K and at 4.2 K, and can be described by

$$J_c(B,T,\theta,\varepsilon_a) = (1 - c_1\varepsilon_a) \times J_c(B,T,\theta), \tag{4.5}$$

where c_1 is equal to 0.073 ± 0.020 independent of temperature and magnetic field. Osamura's data at 77 K in zero field [160] are more precise (using Nyilas extensometers [174]) and show that c_1 has a weak function of strain (i.e. the variation in the normalised J_c with respect to strain is not entirely linear). Nevertheless, to within the error of our measurements, c_1 is similar here to Osamura's work ($c_1 \approx 0.075$) as shown in Figure 4.13 and Figure 4.14. Consistency between (4.4) and (4.5) leads to

$$\begin{aligned} J_c(B,T,\theta,\varepsilon_a) = (1 - c_1\,\varepsilon_a)\alpha'(T)\left(1 - \frac{B_{\text{eff}}(\theta)}{B_{c2}(T,\varepsilon_a = 0,\theta = 90°)}\right) \\ \times \exp\left[-\left(\frac{B_{\text{eff}}(\theta)}{\beta'(T,\varepsilon_a = 0,\theta = 90°)}\right)^k\right]. \end{aligned} \tag{4.6}$$

Usually the changes in the critical current caused by strain that are associated with geometrical changes are ignored because they are smaller than the effect of strain on the superconducting parameters (gauge factor calculated from the Poisson ratio of 0.2 - 0.4 [175] is between 0.014 to 0.018, comparing to 0.073 extracted from the experiments). We have observed a strain dependence for the critical current that has a functional form that resembles a strong geometrical factor with a gauge parameter c_1. This suggests that at fields and temperatures well below B_{c2} and T_c, the strain dependence measured is a combination of the intrinsic strain dependence and a gauge factor term which is of similar order of magnitude.

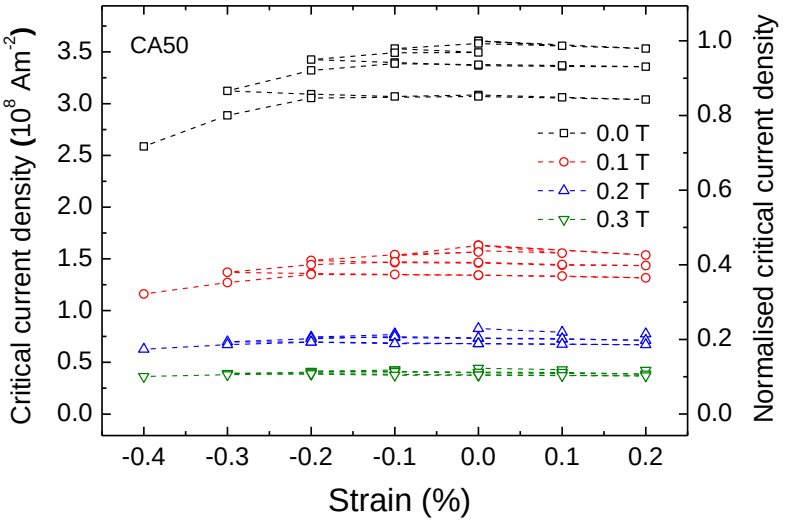

Figure 4.12 Critical current density as a function of strain for the DI-BiSCCO CA50 tape at 77 K at different applied magnetic fields normal to the tape surface. The critical current densities were also normalised with the normalisation constant of 173.7 A.

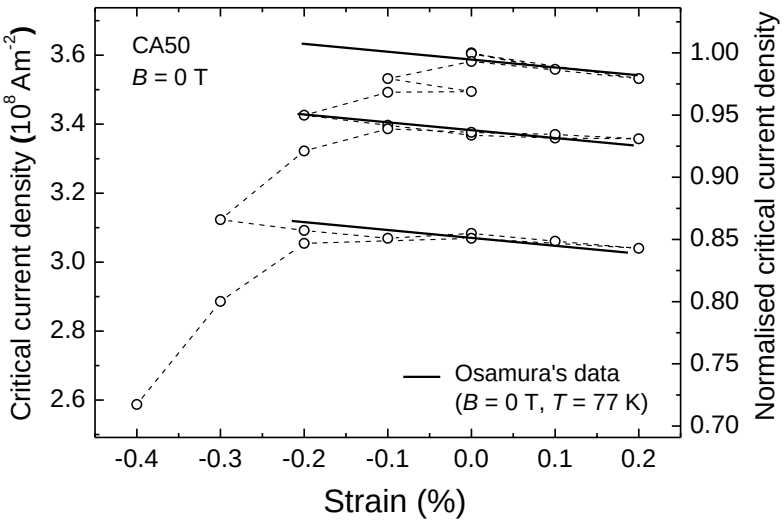

Figure 4.13 Critical current density as a function of strain for the DI-BiSCCO CA50 tape at 77 K for zero field alone. The solid lines are similar to Osamura's data at 77 K in self-field [160]. The normalisation constant is 173.7 A.

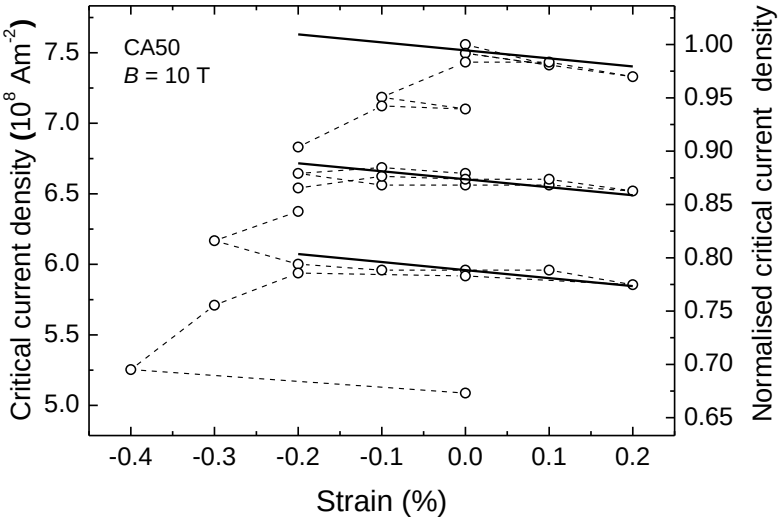

Figure 4.14 Critical current density as a function of strain for the DI-BiSCCO CA50 tape at 4.2 K for the applied magnetic field of 10 T normal to the tape surface. The solid lines have constant gradient which is equal to the gradient in Figure 4.13. The normalisation constant is 364.0 A.

The irreversibility of J_c under compression for BiSCCO tapes has been observed before [149, 150]. A natural concern is whether this behaviour is intrinsic associated with the strongly two-dimensionality of BiSCCO leading to filament buckling or intragranular cracking under strain. This seems unlikely since the elastic constants and limits of BiSCCO are only about a factor of 2 - 3 different from the LTS (e.g. Nb_3Sn). Certainly the (high) porosity of standard BiSCCO conductors can lead to internal cracks and once the mechanical integrity of the composite is compromised, one can expect the full panoply of further damage including cracking and separation (or delamination) of the filaments from the matrix in both tension and compression [176, 177]. The world-class CT-OP BiSCCO composites measured in this work have very low porosity but still show irreversible behaviour of J_c at relatively small compressive strain compared to the LTS materials. Given the low Poisson ratio for BiSCCO compared to metals and the difficulty of achieving strong bonding between metals and oxides, the irreversible behaviour of J_c in these materials for small

compression may be explained by separation between the matrix and the filaments. Given the non-uniform (sausaged) nature of the filaments, irreversibility need not necessarily to be associated with damaged filaments rather initially it may be due to the change in the interfilamentary current flow.

4.5 Concluding comments

The structural anisotropy of Bi-2223 leads to an anisotropy in the critical current density. J_c is dependent on the magnetic field and field orientation as well as the temperature and strain. The field and angular dependence of J_c can be described with the exponential decrease in J_c due to the effective normal magnetic field based on quasi-two-dimensional or anisotropic behaviour.

The variation in the normalised J_c with respect to strain is linear over the reversible range of strain (to within the error bar of our measurement). In addition, the reversibility of J_c of the DI-BiSCCO tapes is extended further into the compressive regime after an irreversible J_c degradation. More detailed analysis and comprehensive J_c measurements are given in Chapter 6 and Chapter 7.

Chapter 5

Probes for investigating the effect of magnetic field, field orientation, temperature and strain on the critical current density of anisotropic high-temperature superconducting tapes in a split-pair 15 T horizontal magnet

5.1 Introduction

Critical current density is probably the most important property of a superconductor from the perspective of technological applications. LTS have been studied intensively as a function of magnetic field, temperature and strain [178-180] with dedicated probes. LTS are broadly isotropic and either ductile or can be produced using wind-and-react techniques so that helical-shaped samples can be formed for measuring J_c in vertical superconducting magnets in high fields. The helical configuration ensures that the heat and voltage generated near the current-lead joints are far from the voltage taps. However most HTS are anisotropic so magnet engineers require knowledge of the anisotropy of J_c - in particular the anisotropy associated with how the angle of the magnetic field with respect to tape surface affects J_c while the transport current remains orthogonal to the field - so helical sample holders are not practical. Furthermore many HTS materials cannot be obtained in unstrained helical form (e.g. 2G $YBa_2Cu_3O_7$ tapes) but are only available as unstrained *straight* conductors. For transport measurements using small currents, these straight materials can be rotated in standard vertical magnets using ingenious experimental design. However as sample currents required for measurement

approach 1000 A in high magnetic fields, low *E*-field high-J_c measurements are best done in a horizontal split-pair magnet. In this chapter we present the important design features of a $J_c(B,T,\theta,\varepsilon)$ probe for making critical current measurements on anisotropic high-temperature superconducting tapes as a function of field, field angle between the magnetic field and surface of the tape (in quasi single crystal tapes this is usually the crystallographic *ab*-plane), temperature and strain for use in our split-pair 15 T (40 mm bore) horizontal superconducting magnet. Our approach was to build and optimise a $J_c(B,T,\theta)$ probe and then optimise the design of a $J_c(B,T,\theta,\varepsilon)$ probe - both are presented in this chapter.

The broad themes of this chapter are structured as follows: Section 5.2 provides a broad description of the $J_c(B,T,\theta)$ probe with some of the guiding principles for design; Section 5.3 considers optimisation of current leads for use in liquid helium. An important aspect of this chapter is optimisation of helium consumption because scarcity of helium gas is currently a serious issue [3]. Wilson [181] has analysed magnet current leads and demonstrated that the minimum heat leak is about 3.0×10^{-3} $Lhr^{-1}A^{-1}$ independent of material used, although the optimum *LI*/*A* varies from material to material. For high-conductivity copper, the optimum *LI*/*A* is 26×10^{6} Am^{-1}. Wilson work considers steady state conditions for magnet current leads where the current is constant and the current leads are in thermal equilibrium. It shows that at optimum design the temperature of the leads remains below room temperature. Operation of hot current leads has been studied in several systems including the pulse mode operation of poloidal field coils of tokamak and low-duty cycling of magnets [182, 183]. Such studies minimise the time-averaged heat leak to reduce helium consumption. In this work, we investigate behaviour of current leads for J_c measurements, where the current is not constant but linearly increased with time over about 3 minutes up to J_c and then rapidly reduced to zero. The effects of duty cycle, maximum current to be measured, static boil-off and the incorporation of additional superconducting tapes as part of the leads are all considered; Section 5.4 considers the design and operation of a variable temperature enclosure. Fixed temperature J_c

measurements are routinely completed in a cryogen such as liquid helium (at 4.2 K) and liquid nitrogen (at 77 K). Standard techniques used to vary and control the temperature include cryogenic vapour pressure control (i.e. liquid refrigerant pumping) [184, 185], use of cryocoolers [186-188] and use of resistance heaters [178, 189, 190]. We require a variable-temperature system that provides a large temperature range and is simple and cheap to operate. The inverted cup was pioneered at the University of Twente [179, 191] to provide a variable-temperature gas environment for J_c measurements of superconductors. This technique provides a large temperature range (above 4.2 K for measurements in liquid helium and above 77 K for measurements in liquid nitrogen) and is also simple to operate. The design and optimisation of the inverted cup is discussed along with calculations of heat transfer from all component parts as well as temperature stability inside the cup; Section 5.5 considers the broad design of the $J_c(B,T,\theta,\varepsilon)$ probe; Section 5.6 considers applying and controlling the axial strain on a superconductor while J_c is measured. Axial strain has long been of interest in the study of LTS and inevitably this interest has followed to HTS wires and tapes. In general, tensile measurements are probably best carried out using Nyilas extensometers [159, 174, 192] which are now commercially available. However, understanding superconductivity in compression is also necessary. Ekin completed a detailed study of the effect of tensile strain on commercial high J_c conductors [193]. Walters introduced a spring design [194] (WASP) to investigate long-length samples at low *E*-field (high sensitivity) under both compression and tension, in high fields. Cheggour *et al* developed a variable temperature WASP [178, 195] that eventually resolved the apparent contradiction between strain and temperature scaling to produce a general scaling law [196, 197]. A variable temperature bending beam apparatus, which allowed (high *E*-field) measurements on short samples of LTS wires and HTS tapes [198-200] in compression as well as in tension, was developed at the University of Twente. The basic principle of the WASP/bending beam is that the sample is soldered to a sample holder and either compressive and tensile strain applied by twisting or bending it and

strain gauges used to determine the strain in the sample. For the HTS materials considered here, a helical WASP is not practical. In order to enable the J_c measurements at low *E*-fields as function of magnetic field orientation as well as temperature and strain, we present the design and operation of a long vertical bending beam (springboard-shaped sample holder) that is used for straight samples in our 40 mm bore horizontal magnet; In Section 5.7, the performance of the $J_c(B,T,\theta,\varepsilon)$ probe is demonstrated by presenting a range of J_c data obtained from YBCO tapes.

All the work on current leads and variable-temperature cup as well as the measurements on DI-BiSCCO tapes in this chapter were completed by the author of this thesis. Design of the springboard-shaped sample holder and measurements on YBCO tapes at 4.2 K in liquid helium were completed by Dr Joshua Higgins.

5.2 Description of $J_c(B,T,\theta)$ probe

Figure 5.1 shows a diagram of the probe designed for investigating the effects of magnetic field, field orientation and temperature on the critical current density of HTS tapes. In operation, the upper part becomes the hottest part of the probe and is most likely to burn out because the heat from the room temperature environment and the Joule heating from the current leads are at their maxima. The head of the probe is designed so that when the current terminals and the upper part of the current leads become hot there are no contiguous components that are likely to fail when hot (e.g. melt).

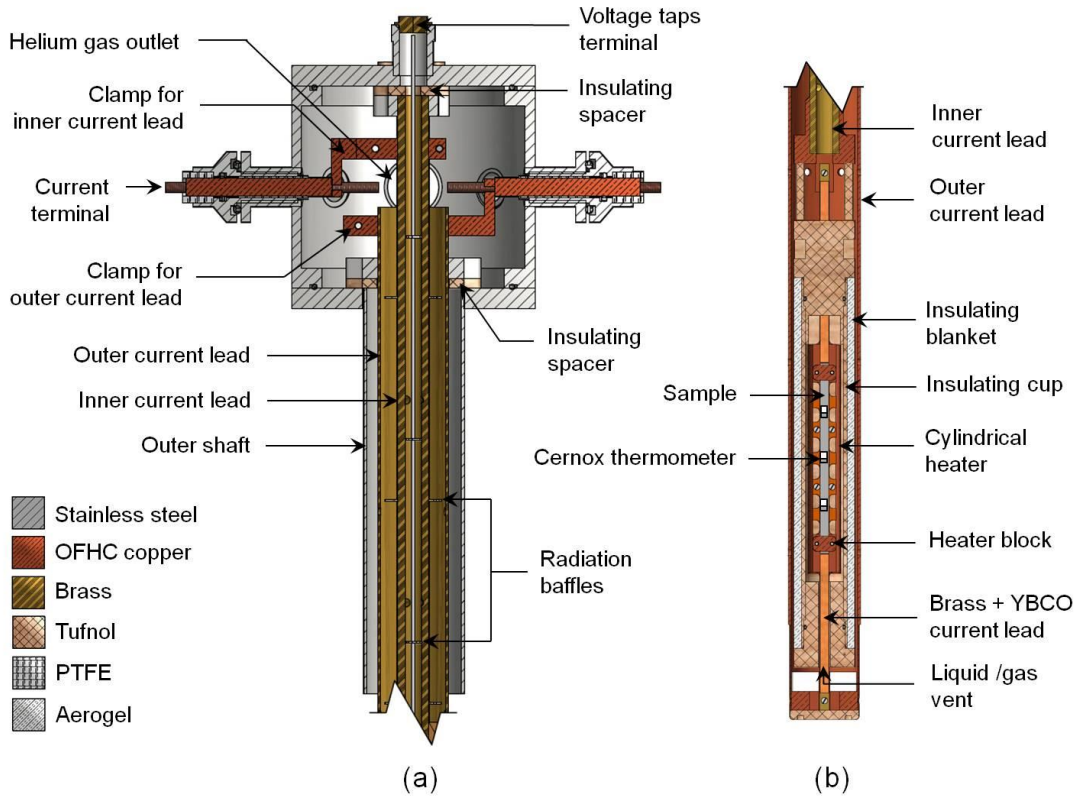

Figure 5.1 Diagram of $J_c(B,T,\theta)$ probe (a) the top part of the probe including (cylindrical) current leads and (b) the final design of the variable-temperature insulating cup.

The current leads themselves are made from two cylindrical brass tubes with different wall thicknesses. Brass was chosen because it has a much lower thermal conductivity than copper at low temperature (two orders of magnitude lower at temperatures below 30 K) and its resistivity is less temperature dependent than an alternative such as high-purity copper [181], which in practice means that current leads can be reasonably robust for a given low heat leak and make it a common choice for magnet current leads. The thermal conductivity and other important properties of materials and gases used in this work are summarised in Table 5.1.

Table 5.1 Density, thermal conductivity and specific heat capacity of materials and gases.

Material/gas	Density (kgm^{-3})			Thermal conductivity ($Wm^{-1}K^{-1}$)			Specific heat capacity ($Jkg^{-1}K^{-1}$)		
	4.2 K	77 K	293 K	4.2 K	77 K	293 K	4.2 K	77 K	293 K
Copper (RRR=50) [a,b]			8950	334	515	393	0.11	196	389
Brass [a,b]			8520	2.08	39.8	109	0.15	216	377
Copper beryllium [a,b]			8330	1.97	36.3	105			419
Stainless steel (304) [a,b]			7860	0.272	7.92	15.1	2	204	470
Polyimide [a,b]			1430	0.011	0.126	0.191	1	338	747
Phenolic [b]			1100	~0.1	0.184	0.281			1260
Tufnol [c]			1350			0.37			1500
Aerogel [d]			150	~0.01	0.010	0.014			1000
Helium (gas) [e,f]	16.76	0.632	0.166	0.009	0.063	0.154	9080	5190	5190
Nitrogen (gas) [e,g]	-	4.612	1.165	-	0.007	0.025	-	1120	1040

[a] Reference [190].

[b] Reference [201].

[c] The properties shown are for Carp Brand Tufnol which is made from phenolic resin and cotton fabric [202].

[d] Reference [203].

[e] Reference [204].

[f] Boiling point of helium is 4.230 K. Latent heat of vapourisation is 20.75 $kJkg^{-1}$ [190] so 1W is equivalent to 1.4 Lhr^{-1}.

[g] Boiling point of nitrogen is 77.35 K. Latent heat of vapourisation is 199.2 $kJkg^{-1}$ [190] so 1W is equivalent to 22 $mLhr^{-1}$

The cylindrical shape of the leads was chosen to provide good mechanical strength and a large surface area for gas cooling. The current leads each have a 2-mm slit along the length (not shown here) to prevent large Eddy currents occurring while sweeping the magnet (wasting cryogen) and in the event that the magnet quenches, to avoid melting the leads. Not shown are Tufnol reinforcing structures that hold the cylindrical current leads in shape. An inverted cup was used to provide a variable-temperature environment for the sample. The outer diameter of the cup was 32 mm so the probe can be inserted vertically into the 40 mm bore of our horizontal magnet system. The angular measurements were performed by rotating the probe to change the relative orientation between the horizontal field and the sample's flat surface. A schematic diagram of Durham's 15 T split-pair horizontal magnet is shown in Figure 5.2 including the split-current-lead design for measurements in such high-field systems. Most parts of the probe were made from stainless steel, oxygen-free high thermal conductivity (OFHC) copper, brass, Tufnol and aerogel as discussed below.

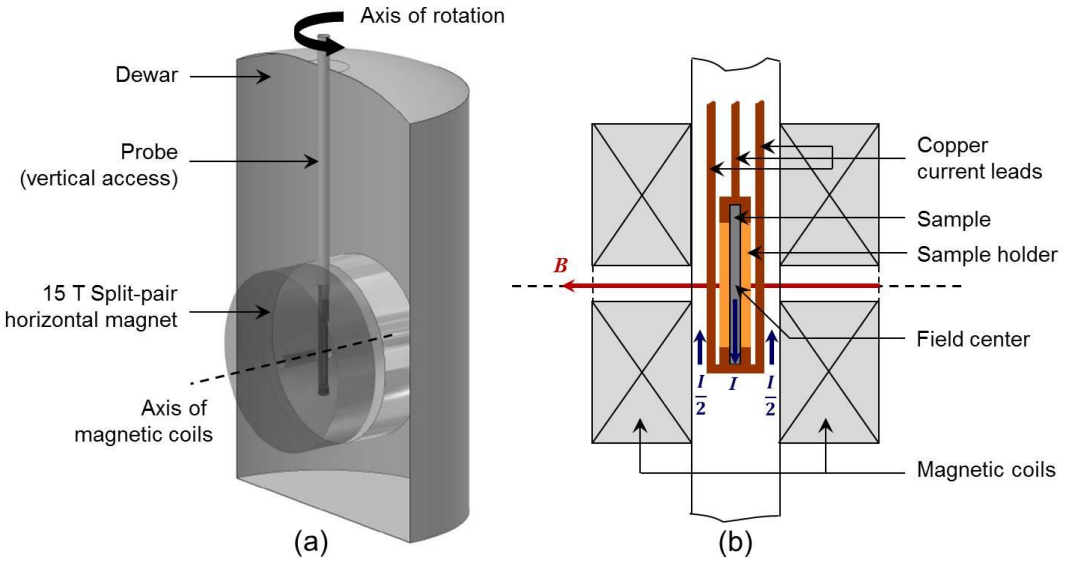

Figure 5.2 Schematic diagram of (a) the 15 T split-pair horizontal magnet system and (b) the split-current-lead design.

5.3 High-current leads

5.3.1 Split-current-lead design

Measurements on isotropic LTS are usually made in vertical magnets where the current leads are parallel to the stray field of the magnet and hence there is no force on them [205]. In contrast, the current leads of probes in horizontal magnets are orthogonal to the stray field so the forces on them can be large and the torque associated with the large Lorentz force can twist the bottom part of the probe even when the top part of the probe is fixed. The split-current-lead design has been used in our group [153] to minimise the torque as well as the magnetic field produced at the sample. The experimental apparatus is illustrated in Figure 5.2 (b). The current lead that is attached to the bottom of the sample is split into two parts while the other (central) lead attached to the top of the sample remains a single lead. Figure 5.3 and Figure 5.4 show the performance of the split-current-lead design we originally used [153] and the design implemented for the $J_c(B,T,\theta,\varepsilon)$ probe. The angular measurements in both probes were performed on DI-BiSCCO tapes at 4.2 K and the data are plotted up to values of current which generated electric fields of 100 μVm^{-1} across the voltage taps (i.e. where J_c is determined). The angle was calculated from the normal field component (B_n) at the sample and was monitored by a Hall sensor during the J_c measurements. Figure 5.3 shows that in the first design the probe twisted up to 3.8° at a starting angle of θ = 10° due to the torque associated with unbalanced currents in the two parts (which in principle can be reduced by actively balancing the currents). These data can be reduced to a single universal curve consistent with a torque twisting the probe. However, the calculated change in the angle of the $J_c(B,T,\theta,\varepsilon)$ probe (i.e. final design in Fig. 5.4) during J_c measurements was found not to be due to a torque (no universal behaviour). We attribute the reduction in twisting achieved to better balancing of the current in the split leads, the increased stiffness of the $J_c(B,T,\theta,\varepsilon)$ probe and the flexibility of the split-current leads (so that the current leads were deformed rather than rotating the probe).

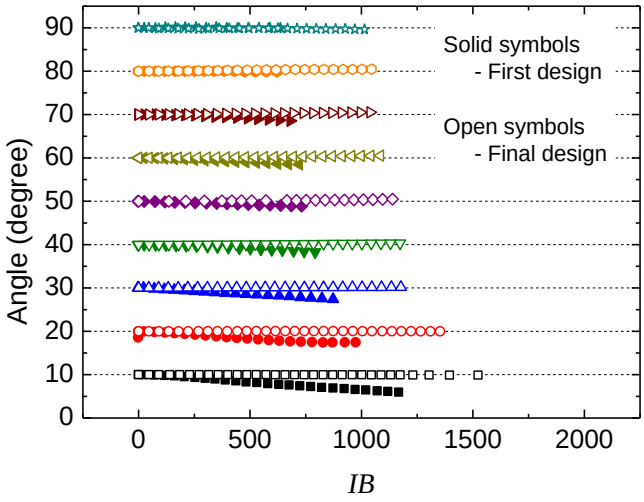

Figure 5.3 Instantaneous angle between magnetic field and the sample's surface as a function of the product of the current and the applied magnetic field for J_c measurements on a DI-BiSCCO tape at 4.2 K at different starting angles. The applied magnetic field was 3 T for the first design and 14 T for the final design.

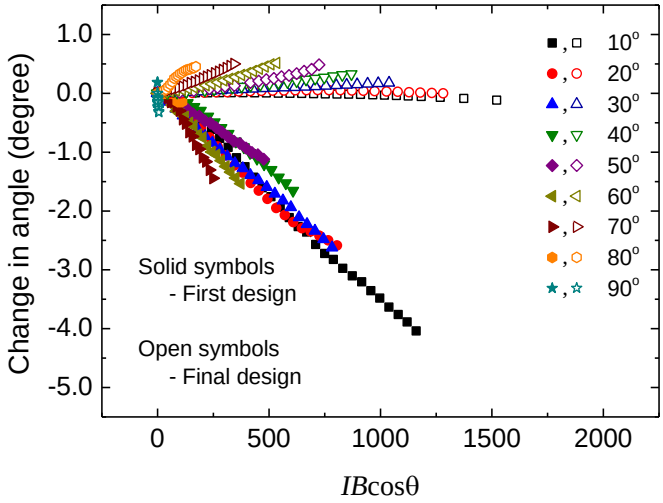

Figure 5.4 Data from Figure 5.3 replotted as the change in the angle during the J_c measurement as a function of the product of the current (I), the applied magnetic field (B) and the cosine of the instantaneous angle between magnetic field and the sample's surface at different starting angles.

Figure 5.5 shows the change in the measured component of the field normal to the sample surface for different starting angles at 80 A which is a result of the Lorentz force associated with current flowing in the sample itself. B_n decreased when the angle was less than ~15° and increased otherwise. The maximum increase was found at ~50°. We attribute these changes to the Lorentz force moving the sample in a plane which has a spatial field variation (inset).

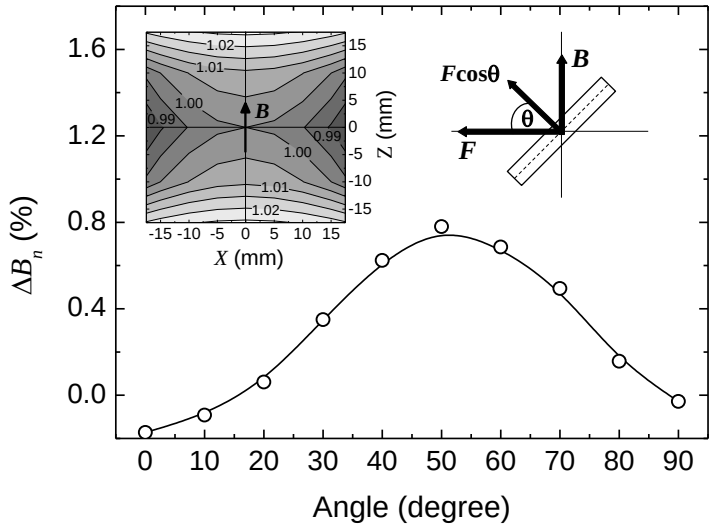

Figure 5.5 Change in the normal field component at the sample when the current is at 80 A as a function of the starting angle between magnetic field and the sample's surface for the J_c measurements using $J_c(B,T,\theta,\varepsilon)$ probe. The inset shows the normalised magnetic field profile of Durham's split-pair horizontal magnet along the *x*-*z* plane which is the plane of the sample's cross-section. Movement of the sample (i.e. change in the normal field component) is attributed to effects of the normal force component ($F\cos\theta$).

5.3.2 Optimisation of the critical-current leads

The cross-sectional area of the current leads which have one end at room temperature and the other end at cryogenic temperatures can be optimised by considering all means of heat transfer. The generalised one-dimensional transient heat transfer equation for *one* vapour-cooled current lead is given by [206]:

$$\frac{\mathrm{d}}{\mathrm{d}x}\left(\kappa(T)A\frac{\mathrm{d}T}{\mathrm{d}x}\right)-fm(t)c_p\frac{\mathrm{d}T}{\mathrm{d}x}+\frac{I^2(t)L_0T}{A\kappa(T)}=A\tilde{\rho}c(T)\frac{\mathrm{d}T}{\mathrm{d}t} \qquad (5.1)$$

where T is the temperature in kelvin, x is the distance in metres along the current lead, κ is thermal conductivity of the current lead in $\mathrm{Wm^{-1}K^{-1}}$, m is the mass flow of cryogen gas in $\mathrm{kgs^{-1}}$, I is the current flowing in amperes, f is the efficiency of heat transfer between the current lead and the gas, c_p is the specific heat capacity of the cryogen gas at constant pressure in $\mathrm{Jkg^{-1}K^{-1}}$, $L_0 = 2.44\times10^{-8}\ \mathrm{W\Omega K^{-2}}$ is the Lorentz number, and $\tilde{\rho}$ and c are the density and specific heat capacity of the current leads in $\mathrm{kgm^{-3}}$ and $\mathrm{Jkg^{-1}K^{-1}}$ respectively. Equation (5.1) includes the effects of heat conduction along the current lead, heat transfer from the current lead to the gas and Joule heating of the current lead carrying the current I. Radiative heat transfer inside cryostat has been ignored [182, 183]. A schematic diagram of a current lead and the heat transfer mechanisms is provided in Figure 5.6. The mass flow is found from the conductive heat transfer into the cryogen at the bottom end, $m(t) = (\kappa A/c_l)\mathrm{d}T/\mathrm{d}x\big|_{x=0}$, where c_l is the latent heat of vapourisation in $\mathrm{Jkg^{-1}}$. However, accurate calculation also requires the inclusion of static boil-off of the cryostat (m_{sta}) and any additional Joule heating from elements directly immersed (below) in the cryogen. An expression for the total cryogen boil-off for one current lead is therefore

$$m(t)=\frac{\kappa A}{c_l}\frac{\mathrm{d}T}{\mathrm{d}x}\bigg|_{x=0}+\frac{1}{2}\left(\frac{I^2(t)R}{c_l}+m_{\mathrm{sta}}\right), \qquad (5.2)$$

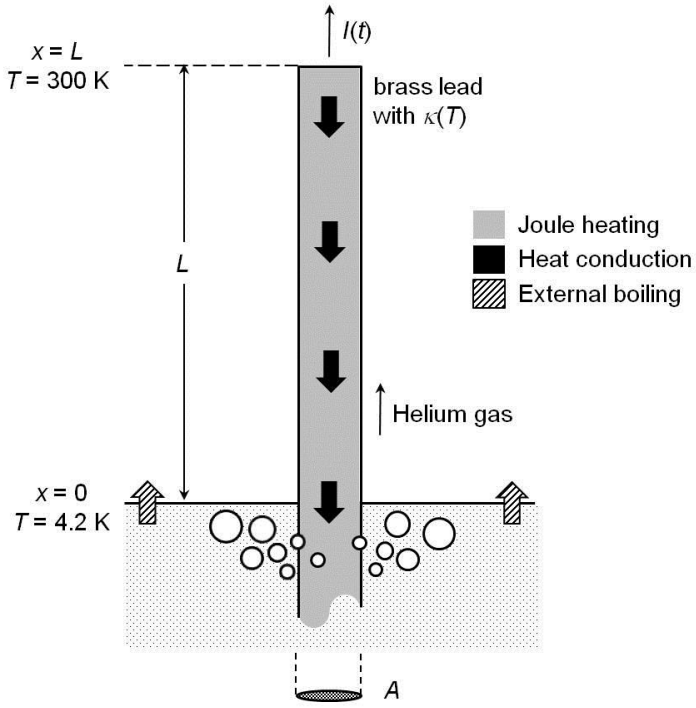

Figure 5.6 Schematic diagram of a vapour-cooled brass current lead and heat transfer considerations for measurements in liquid helium.

where R is the total resistance of all parts immersed in the cryogen (in ohms). The contribution of all static (primarily heat conduction into the Dewar) or sample boil-off (Joule heating) is assumed to be equally distributed among the two current leads. For best practice, R is generally minimised by using the high purity copper or adding superconducting material as part of the electrical circuit so in the rest of this chapter we shall set R to zero.

The efficiency of heat transfer is by definition given by $f = (T\text{-}\Delta T)/T$ where ΔT is the difference between the temperature of the gas and the current lead at the same height [181]. It is physically dependent on the geometry of the current leads, the mass flow of the cryogen and the physical properties of the gas itself which vary along the current leads because of their temperature dependence. By taking into account the shape of the current leads, the cooling term can be written as a convective heat transfer term, $hP'(T\text{-}T_g)$, which includes gas temperature (T_g) and cooled perimeter

(P'). h is the heat transfer coefficient which is $\cong 4\kappa_g/D'$ for a cylindrical pipe where κ_g is the thermal conductivity of the gas, $D' \cong 4A'/P'$ is the hydraulic diameter and A' is the cross-sectional area of the pipe. Taken together, f can be written as a function of h where

$$f = \left[1 + \frac{m(t)c_p(\mathrm{d}T/\mathrm{d}x)}{hP'T}\right]^{-1}. \qquad (5.3)$$

Equation (5.3) describes the effects of gas properties, temperature variation and geometry of the current lead on the efficiency of heat transfer. By having P' and A' in the relation, f is inevitable system dependent. A typical value for f from our measurements is between 0.8 - 1.0 which suggests efficient heat transfer. Hence in order to simplify our analysis, we have set f =1 (perfect heat transfer) in the optimisation. Cylindrical current leads were used to try to ensure that this condition was achieved.

Numerical calculations of the temperature profile of the critical-current leads for measurements in liquid helium and the helium boil-off were performed using FlexPDE. The boundary conditions used in the time-dependent analyses were: $T(x = 0, t)$ = 4.2 K and $T(x = L, t)$ = 300 K where L is the current lead's length. A J_c measurement is typically performed by ramping the current from zero up to above the transition, where the measured voltage is rapidly increasing. One measurement generally takes ~200 s before the current is set to zero and the probe is ready for the next measurement. The ratio between the measuring time and the total time in one cycle is defined as a duty cycle (D). In this work, we consider the effects of duty cycle on the temperature profile and the average helium boil-off of the current lead by using the measuring time of 200 s at which the applied current reaches the maximum value of $I_{\max}$.

Without static or sample boil-off

Figure 5.7 illustrates the temperature profile of a brass current lead at 0 s, 200 s and 1200 s (i.e. before the measurement, at the end of the measurement and 1000 seconds after the measurement has finished) and the instantaneous helium boil-off (inset) during the first cycle where A = 60 mm^2, L = 1.0 m, I_{max}= 1000 A and there is no static or sample boil-off, i.e. $b' = (I^2R/c_l + m_{sta})/\tilde{\rho}_{liquid}$ = 0 where $\tilde{\rho}_{liquid}$ is the density of liquid helium. We have used $b = m/\tilde{\rho}_{liquid}$ to represent helium boil-off measured in (useful experimental units of) Lhr^{-1}. To first order, b increases linearly with increasing current up to I_{max} and then slowly decays once the current is switched to zero due to the slow decrease in temperature back to equilibrium. The high temperature near the top end is up to 745 K. Hot current leads are not found for magnet current leads carrying a constant current in thermal equilibrium when helium boil-off is correctly minimised [181].

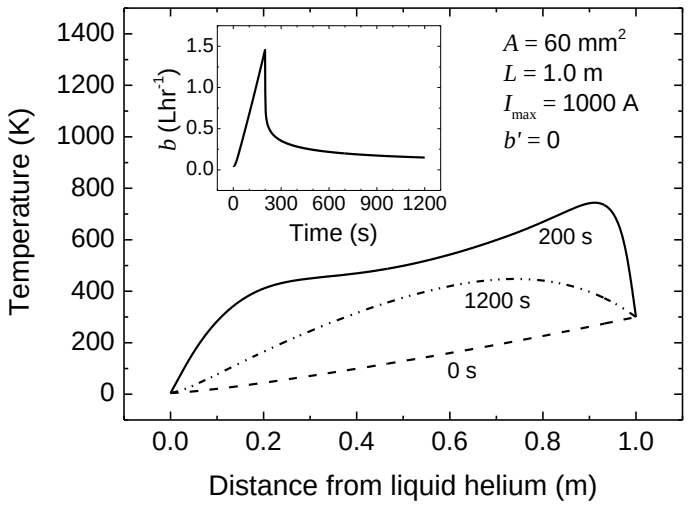

Figure 5.7 Calculated temperature profile of a vapour-cooled brass current lead with the bottom end immersed in liquid helium while ramping current up to a maximum current of 1000 A in 200 s and then reducing the current to zero without any static or sample boiling (b' = 0). The current lead's length is 1.0 m and the cross-sectional area is 60 mm^2. The inset shows calculated helium boil-off as a function of time.

Figure 5.8 shows the calculated average helium boil-off over 10 cycles for two current leads versus cross-sectional area as a function of applied current and duty cycle for L = 1.0 m. The average helium boil-off is approximately proportional to the maximum applied current. The data for D = 0.5 are re-plotted in Figure 5.9 as b/I_{max} versus I_{max}/A, together with the calculated data for L = 0.6 m and 0.8 m. The optimised operation obtained at the minimum helium boil-off is at I_{max}/A = 5×10^6 Am^{-2} for L = 1.0 m and at larger numbers for shorter current leads. The resulting maximum temperature (T_{max}) of the current lead is ~350 K as shown by the inset.

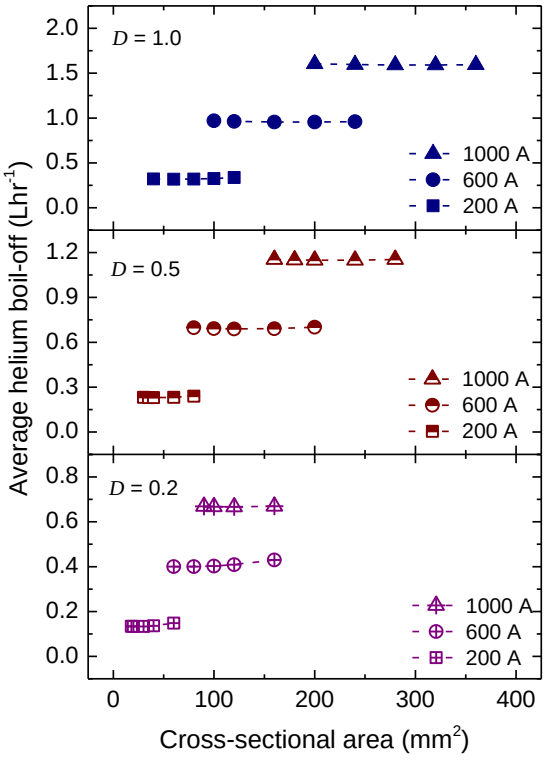

Figure 5.8 Calculated average helium boil-off (averaged over 10 cycles) for two vapour-cooled brass current leads as a function of the cross-sectional area of each lead carrying a current up to 200, 600 and 1000 A for duty cycles of 0.2, 0.5 and 1.0. The system has no static or sample boil-off and the length of all current leads is 1.0 m.

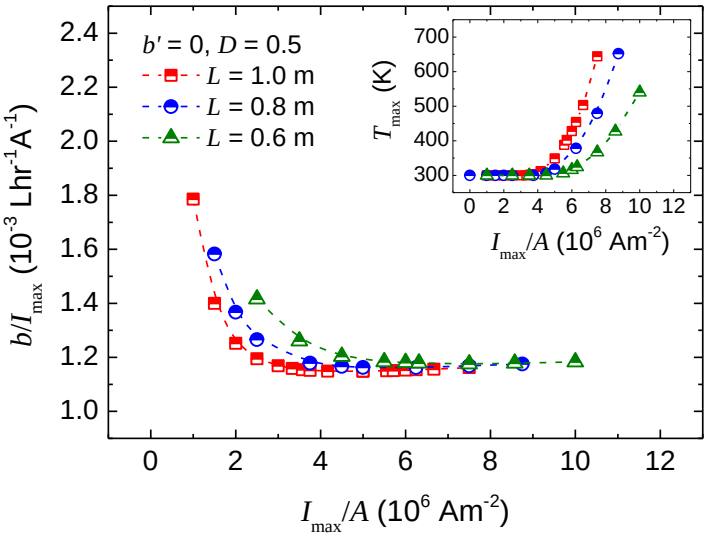

Figure 5.9 Calculated average helium boil-off per unit current (b/I_{max}) for two vapour-cooled brass current leads and maximum temperature (inset) as a function of the ratio between maximum current and cross-sectional area (I_{max}/A) of each lead without any static or sample boiling for the duty cycle of 0.5 and the current lead's lengths of 0.6, 0.8 and 1.0 m. The maximum current investigated was 1000 A.

Tapered current leads

Since the heat leak into the liquid helium is a function of *A*, as given in Equation (5.2), we investigated the effects of making *A* smaller at the bottom end of the current leads by modelling heat flow in tapered current leads. The positional dependence of *A* was taken to be $A(x) = A_{min} + Cx$ where *C* ranges from 20 to 80 mm^2 per meter and A_{min} is the cross-sectional area at the bottom end. A range of calculated results are shown in Figure 5.10 where b/I_{max} is plotted as a function of the maximum temperature. Calculated values for uniform *A* are also shown for comparison. Figure 5.10 shows that there is little difference between the uniform current leads and tapered current leads in terms of helium boil-off for any given maximum temperature. The different is discernible only when *D* = 1.0 where the tapered current leads create higher helium boil-off at a given T_{max}. We conclude that

reducing *A* increases the thermal resistance so that less heat is conducted into liquid helium when no current flows. However, once the current is applied, the consequent increase in the electrical resistance leads to a larger heating especially at the bottom end which compensates for the effect of cross-sectional area reduction. We conclude that making the current lead smaller at the bottom end to reduce the boil-off is not productive.

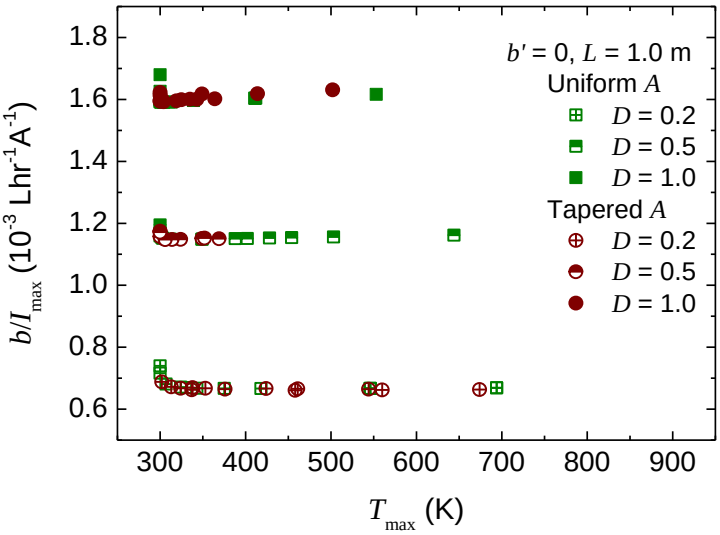

Figure 5.10 Calculated average helium boil-off per unit current (b/I_{max}) for two vapour-cooled brass current leads as a function of maximum temperature with uniform cross-sectional area and tapered cross-sectional area. The system has no static or sample boiling and the length of all current leads is 1.0 m. The maximum current investigated was 1000 A.

Non-zero static boil-off

In most systems, there exists a static or sample boil-off which can be exploited in optimising *A*. Figure 5.11 shows the average helium boil-off and maximum temperature (inset) as a function of I_{max}/A with and without static boil-off which is typically from the cryostat - although one could optimise further by considering the boil-off from the cryostat and magnet at the lowest field (lowest boil-off) at which J_c is to be measured. The average static helium boil-off obtained from our horizontal magnet system is 0.3 Lhr^{-1} which has been included in the calculations. Figure 5.11 shows that for all duty cycles when $b' \geq 0.3$ Lhr^{-1}, T_{max} is larger than 750 K while the helium boil-off does not even reach its minimum value. These results show that quite generally, T_{max} of the current leads becomes the important limiting factor that determines the optimum *A* although the helium boil-off is not minimised.

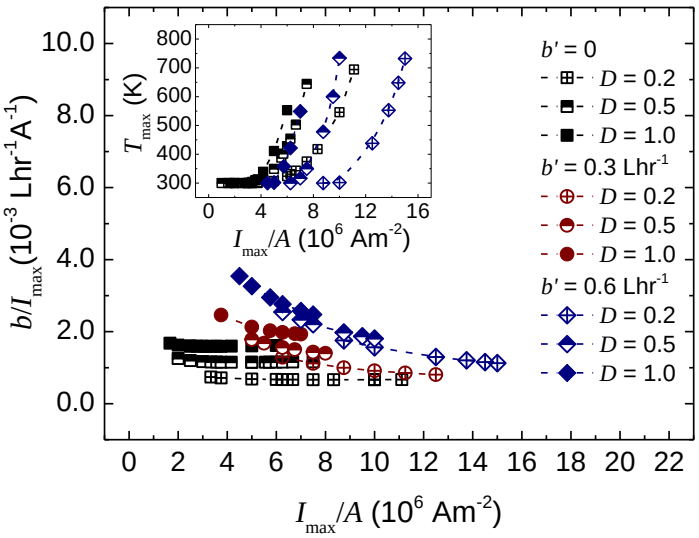

Figure 5.11 Calculated average helium boil-off per unit current (b/I_{max}) for two vapour-cooled brass current leads and maximum temperature (inset) as a function of the ratio between maximum current and cross-sectional area (I_{max}/A) of each lead with and without static or sample boiling. The length of all current leads is 1.0 m. The maximum current investigated was 1000 A.

Superconducting components of current leads

Adding some HTS along the current leads is useful in order to reduce Joule heating. Because in practice the amount of cryogen changes during experiments, it is not straightforward attaching the HTS tapes to the current leads whilst ensuring the temperature is always below the critical temperature of the component superconductor. Typically, one is conservative and the HTS is soldered to the current lead only near the bottom end. We have used YBCO coated conductor tape which has low thermal conductivity materials in its structure. The standard YBCO tape from SuperPower (SCS-type) has two 20-μm copper stabilising layers and one 2-μm silver overlayer. The stabiliser-free tape (SF-type) has no copper which is useful for current lead applications. Five YBCO (SF4050) tapes were added into the calculations for L = 1.0 m from x = 0 m to x = 0.5 m, which is the position that the temperature is below the T_c of 93 K [63] in zero-current operation. The calculated average helium boil-off and maximum temperature for the hybrid current lead (brass and YBCO tapes) are shown in Figure 5.12. The optimum A and resulting $T_{\max}$ are within ~20% of the brass current lead alone. Nevertheless, the helium boil-off is 50 % lower because the smaller Joule heating at the bottom end leads to a lower temperature gradient at x = 0 m.

Optimisation equation

The optimum A for vapour-cooled brass current leads, where the helium boil-off is minimised, is strongly dependent on the duty cycle of the measurement. The optimum A decreases with decreasing duty cycle as shown by dotted line in Figure 5.13 which is a plot of the optimised shape factor ($LI_{\max}/A$) as a function of duty cycle. For D = 1.0, the optimisation of the brass critical-current lead is

$$\frac{LI_{\max}}{A} = 3.2\times10^{6}\ \ \mathrm{Am^{-1}} \qquad (5.4)$$

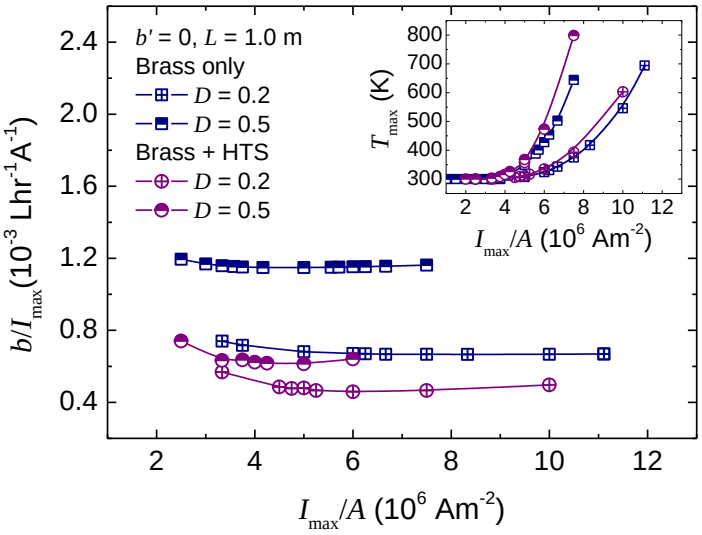

Figure 5.12 Calculated average helium boil-off per unit current ($b/I_{\max}$) for two vapour-cooled brass current leads and maximum temperature (inset) as a function of the ratio between maximum current and cross-sectional area ($I_{\max}/A$) of each lead with and without HTS tapes at x = 0 m to x = 0.5 m from the total length of 1.0 m. The system has no static or sample boiling.

and the helium boil-off from two current leads is

$$\frac{b}{I_{\max}} = 1.6\times10^{-3}\ \text{Lhr}^{-1}\text{A}^{-1}. \tag{5.5}$$

Equation (5.5) is about half the boil-off of that for brass magnet current leads which is 3.0×10^{-3} $\text{Lhr}^{-1}\text{A}^{-1}$. For D < 1.0, the optimised critical-current lead runs hot - the temperature is above room temperature near the top end. Eventually $T_{\max}$ of the critical-current leads becomes the critical optimisation factor as shown by dashed and solid lines in Figure 5.13 which are calculated using the empirical relation

$$\frac{LI_{\max}}{A} = \frac{\left(5.56\times10^{6}\right)\cdot L^{0.4}\cdot\left(T_{\max}-300\right)^{0.22\exp(-b')}}{D+2\exp\left(-2b'\right)}\ \text{Am}^{-1} \tag{5.6}$$

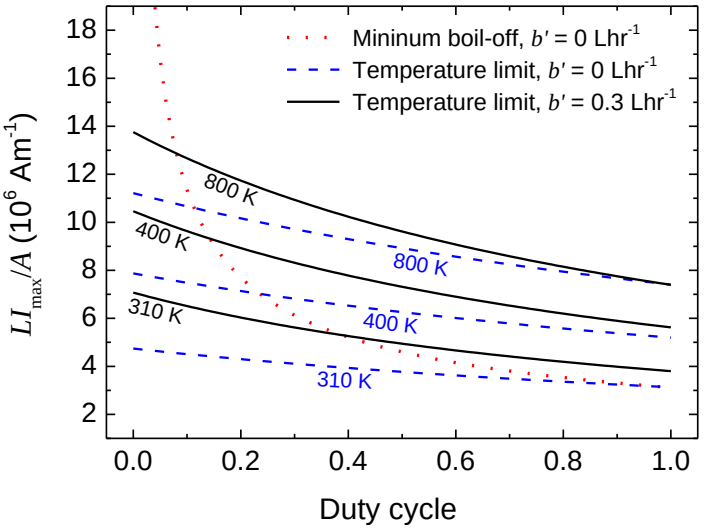

Figure 5.13 Optimum shape factor ($LI_{\max} / A$) of the current lead for critical current measurements as a function of duty cycle calculated from (5.6) where the maximum temperature of the current lead is a limiting factor (dash and solid lines), in comparison with the optimum shape factor obtained at the minimum average helium boil-off for the current lead's length of 1.0 m (dotted line). For b' = 0.3 Lhr^{-1}, the minimum boil-off gives a maximum temperature larger than 800 K.

which is accurate within 10 % for $D > 0.2$ and within 30 % for $0.1 < D < 0.2$ where $T_{\max} > 310$ K and $b' < 0.6$ Lhr^{-1}. At high duty cycles, the calculated optimum $LI_{\max} / A$ determined by $T_{\max}$ from (5.6) is higher than the optimum $LI_{\max} / A$ that gives the minimum helium boil-off. However the helium consumption is only 5 % higher than the actual minimum value. A general empirical expression for boil-off accurate to ~15 % is given by

$$\frac{b}{I_{\max}} = \frac{D+0.5}{1000} + \frac{b'}{1000}\left[2.3(D+0.75) - 0.2(D+1)\cdot\ln(T_{\max} - 300)\right] \text{ Lhr}^{-1}\text{A}^{-1}. \quad (5.7)$$

Assuming L = 1.0 m for our magnet system with b' = 0.3 Lhr^{-1}, D = 0.2 and $T_{\max}$ = 400 K, the calculated optimum $LI_{\max} / A$ is 9.08×10^6 Am^{-1}. Optimal dimension of the

current leads is shown in Table 5.2. Comparing to the optimum value of LI/A from steady state calculation for magnet current leads of 1.54×10^6 Am^{-1} where the static boiling and the duty cycle are not considered, the current leads optimised in this work reduce helium consumption from 4.8 Lhr^{-1} to 1.0 Lhr^{-1} for J_c measurements up to 1000 A.

In addition, HTS tapes are used at the lower part of the current lead to further reduce helium boil-off from Joule heating above and below helium level. One can calculate the optimum A using an L value at the minimum helium level (longest L) and put the HTS tapes above that level to the maximum helium level (shortest L).

Table 5.2 Optimal dimension of the brass current leads for critical current measurements up to 1000 A in Durham's split-pair 15 T horizontal magnet.

Parameter/dimension	Value
Duty cycle	0.2
Static boil-off (Lhr^{-1})	0.3
Maximum temperature (K)	400
Current lead's length (m)	1.0
Maximum current (A)	1000
Cross-sectional area (each, mm^2)	110
Calculated helium consumption (average, Lhr^{-1})	1.0

5.3.3 Temperature profile and gas flow measurements

Temperature profile measurements were performed along one of the vapour-cooled brass current lead to investigate to what degree the calculations agree with the experiments. The temperature profile was measured using five platinum resistance thermometers (standard PT 100) attached along the current lead every 20 cm from the top end, that is, the thermometers were at $x = L$, L - 0.2, L - 0.4, L - 0.6 and L - 0.8 m from helium level. The thermometers were calibrated above 12 K in a Quantum Design Physical Properties Measurement System© and at 4.2 K in liquid helium. The effective length of the current lead was estimated from measuring the helium level in the cryostat using a cryogen level meter and the average helium gas flow along the current lead was monitored using a Techniquip MGF-420 gas flow meter calibrated for helium with the accuracy of 1.5 %. The meter was an insertion-type so the pressure drop across it was negligible.

Figure 5.14 shows the temperature of a 10-mm^2 vapour-cooled brass current lead at x = 0.18, 0.38, 0.58, 0.78 and 0.98 m from liquid helium as a function of instantaneous current while it was ramped at 6 As^{-1}. The inset shows the temperature profile of the current lead when the current was at 300 A. The dashed lines are calculated values which are in good agreement with the experimental data except for x = 0.98 m where the calculated temperature is higher. The data in Figure 5.14 show a high helium boil-off due to the large Joule heating under the helium level which corresponds to a resistance R (cf Eqn. 5.2) of 4 mΩ. We attribute the differences between calculation and experiment at the head of the probe to the role of the terminal box (shown in Fig. 5.1(a)), the complex thermal sinking of the leads at room temperature and the helium gas convectively flowing within the terminal box before leaving the system. We expect the top end of the current lead to experience more cooling than is accounted for computationally.

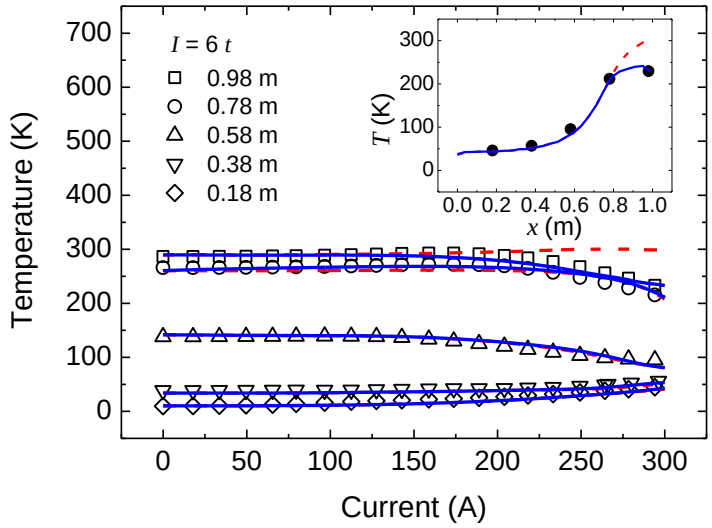

Figure 5.14 Temperature of a 10-mm^2 current lead as a function of applied current ramping at 6 As^{-1} up to 300 A. The inset shows temperature profile at the current of 300 A. Dashed lines are calculations using Equations (5.1) - (5.3) with $m = \tilde{\rho}_{\text{liquid}} b$ from the experiment. Solid lines are calculations including the convective-like cooling effect near the top end.

The solid lines of Figure 5.14 account for this additional cooling by assuming that the convectional cooling in the box is proportional to x and b with an additional proportionality constant as a free parameter. It was found that the additional cooling term added from $x = L$ - 0.2 m to $x = L$ m was $34.6bx$ which can be considered a characterising convective heat transfer between the helium gas and the current lead as h and ΔT are proportional to b and x, respectively. The calculated efficiency of heat transfer is between 0.8 and 1.0 at low current and decreases as the current increases. The calculated Reynolds number is up to 3500 at 300 A which is in the transition region from laminar to turbulent flow [207]. Figure 5.14 shows the broad features of the temperature profile from computation and experiment which are in broad agreement for the vapour-cooled current lead in this work.

5.4 Variable-temperature cup

5.4.1 Design and calculations

Two designs of the variable-temperature cup were produced and tested. The first one was made from Tufnol alone with the wall thickness of 6 mm. In the second design, the wall thickness of the Tufnol cup was reduced to 2 mm and a Spacetherm® aerogel blanket was used. In the latter case, the Tufnol helps provide mechanical support for the aerogel insulation. The thermal conductivity of the aerogel is as low as 0.014 $Wm^{-1}K^{-1}$ [203] at room temperature while the thermal conductivity of Tufnol is 0.37 $Wm^{-1}K^{-1}$ [202]. The outer diameter of the cup was fixed to 32 mm. The design parameters are listed in Table 5.3 and a schematic of the second design (Tufnol + aerogel) of the variable-temperature cup is illustrated in Figure 5.1(b). As shown in Figure 5.1(b), the current leads passed through the cup at the top (which was sealed with epoxy) and at the bottom (through a vent for gas to escape when the temperature is increased [191]). The temperature along the sample was measured with three Cernox thermometers (CX-1050-SD-1.4L) calibrated from 1.4 K to 325 K. The magnetic field dependence of the thermometers was up to -0.16 % at 20 K and 14 T and accounted for in setting the temperature. The temperature was controlled by two LakeShore 336 cryogenic temperature controllers with the resistive heater outputs. Three heaters were used to vary the sample's temperature. Two of them were made from a constantan wire noninductively wound on the OFHC copper block which was attached to the sample holder. The resistance of the two heaters was 51.2 Ω and 53.4 Ω. Another heater with the resistance of 79.5 Ω was made by winding a constantan wire on a thin-wall cylindrical OFHC copper support which was placed around the sample. Six layers of aluminised Mylar superinsulation were wrapped around the cylindrical heater in order to reduce the heat transfer by radiation.

Table 5.3 Design parameters of the variable-temperature cups.

Parameter	1st design	2nd design
Tufnol thickness (mm)	6	2
Aerogel thickness (mm)	-	4
Internal CSA (mm^2)		
Cup	314	314
Vent	78	38
Current lead		
Brass CSA (mm^2)	5	5
No. of YBCO tapes	5	3

Heat transfer from the cup to the liquid cryogen reservoir is via conduction through the wall of the insulating cup as well as the current leads, together with heat leak through the liquid/gas vent (cf Fig. 5.1(b)). Heat transfer through the vent is complex. We have calculated it using a film boiling heat transfer coefficient (h_b) to calculate a convective-like heat transfer. The film boiling heat transfer coefficient is given by [208]

$$h_b = 0.37\left(\frac{g(\tilde{\rho}_L - \tilde{\rho}_V)}{\gamma'}\right)^{1/8}\left(\frac{\kappa_V{}^3\tilde{\rho}_V(\tilde{\rho}_L - \tilde{\rho}_V)gc_{\text{eff}}}{\eta_V \Delta T}\right)^{1/4} \tag{5.8}$$

where $c_{\text{eff}} = (c_l + 0.34c_p\Delta T)^2 / c_l$ is the effective latent heat of vapourisation in Jkg^{-1}, g is the standard gravity, γ' is the surface tension in kgs^{-2}, η is the viscosity in $kgm^{-1}s^{-1}$, $\tilde{\rho}$ is the density in kgm^{-3} and ΔT is the temperature difference between liquid and vapour. Subscripts L and V represent the liquid and vapour properties

respectively. The total heat load or power consumption of the variable-temperature cup in liquid helium is given by

$$P = \left(\kappa_t A_t \frac{\Delta T}{\Delta x}\right)_{\text{cup}} + \left(\kappa_t A_t \frac{\Delta T}{\Delta x}\right)_{\text{current leads}} + h_b A_b (T - 4.2) \qquad (5.9)$$

where A_b is the effective area of the vent. The calculated values are compared to the measured values in Figure 5.15 as a function of operating temperature. We attribute the differences, especially at higher temperature, to uncertainties in the temperature dependence of thermal conductivity of component materials and the uncertain boiling level and effective area of the vent. Table 5.4 shows the calculated heat load of the two designs of the cup at 50 K operating in liquid helium. The contribution from each type of heat transfer is also shown as a percentage of the total heat load. The major source of the heat transfer in the Tufnol design is conduction through the walls of the cup, which led to the use of the aerogel insulation in the second design. Other improvements include the reduction in the size of the vent and number of YBCO (SCS4050) tapes soldered on the bus bar current leads. All improvements

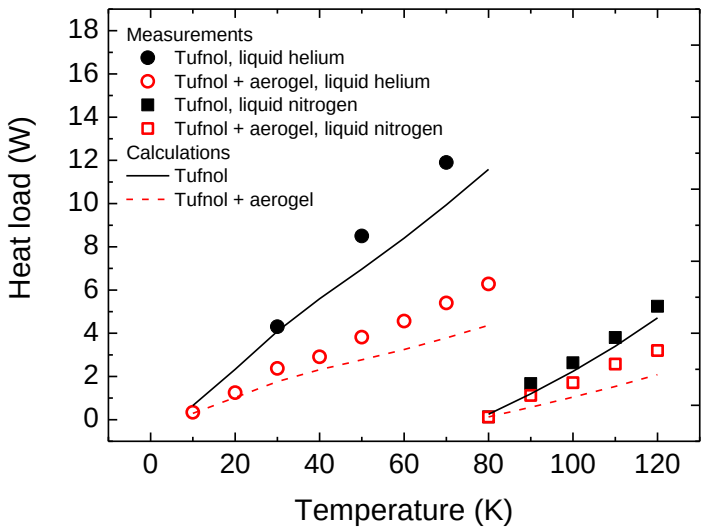

Figure 5.15 Heat load in operation of the variable-temperature cup as a function of the set-point temperature for measurements in liquid helium and liquid nitrogen.

Table 5.4 Calculated heat load of the variable-temperature cups in liquid helium.

Calculated heat load	1st design	2nd design
Average percentage (%)		
Cup	56.2	37.5
Current leads	25.9	41.0
Boiling	17.8	21.5
At 50 K (W)	7.0	2.7

together reduce the total heat load from 7.0 W to 2.7 W at 50 K. (equivalent to reducing helium consumption from 9.8 Lhr^{-1} to 3.8 Lhr^{-1}). The major heat source in the optimised design is conduction through the current leads, which is difficult to improve further.

5.4.2 Variable-temperature measurements

The Tufnol + Spacetherm® aerogel variable-temperature cup was used to provide a variable-temperature environment for the J_c measurements on a DI-BiSCCO tape manufactured by Sumitomo Electric Industries. The J_c measurements were carried out using a standard four-terminal technique with a pair of voltage taps 10-mm apart. The measurements were performed in liquid nitrogen in a conventional iron-cored electromagnet and in liquid helium in our 15 T vertical superconducting magnet. The temperature along the sample was monitored during the measurement to investigate the stability and variability of the temperature along the sample.

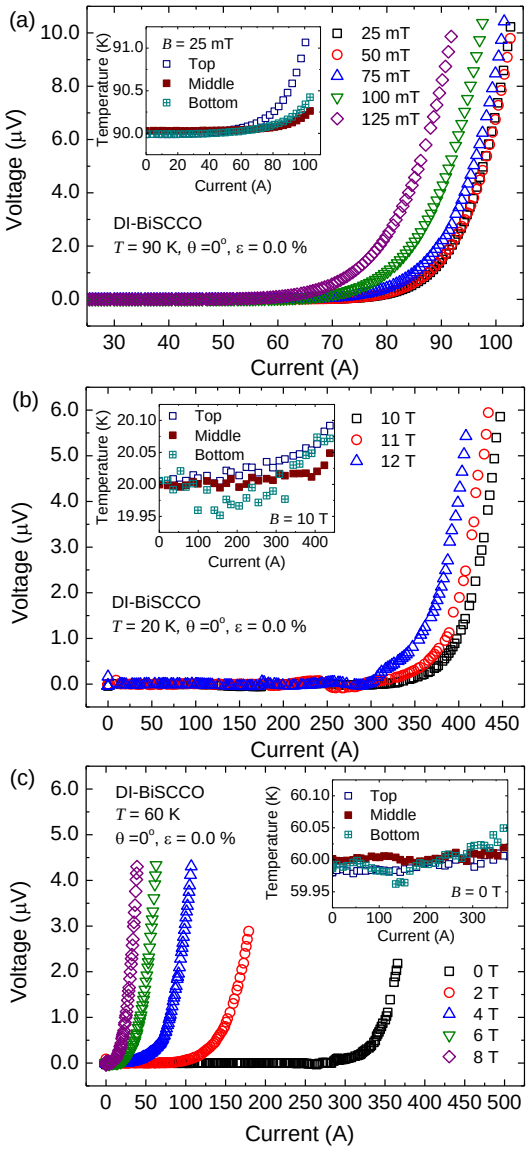

Figure 5.16 (a) Voltage-current characteristics of a DI-BiSCCO tape at 90 K as a function of applied magnetic field parallel to the tape surface for measurements in nitrogen. The inset shows the temperature rising during the transition for the data taken at 25 mT where the critical current is 88 A at 100 μVm^{-1}. Temperature increase across the voltage taps is 130 mK. (b) and (c) Similar plots at 20 K and 60 K for measurements in helium. The insets are data taken at 10 T at 20 K and 0 T at 60 K where the critical currents were 398 A and 352 A, respectively. In both cases, temperature increase across the voltage taps is ~30 mK.

Figure 5.16 shows the voltage-current characteristics of the DI-BiSCCO tape as a function of magnetic field applied parallel to the tape surface for measurements in nitrogen at 90 K and in helium at 20 K and 60 K. The insets show the sample temperature measured at the top, the middle and the bottom region of the sample during the J_c measurements. The initial temperatures are typically within 50 mK of the set point at the start of the measurements. Feedback control is such that at J_c there is an additional uncertainty of ~30 mK across the voltage taps for measurements in liquid helium. The difference between the temperature and set point is higher at the top and the bottom parts of the sample especially for measurements at 90 K in liquid nitrogen where the temperature increase across the voltage taps is 130 mK. We attribute this to resistive heating in the YBCO current leads which enter the normal state at 93 K. Below 60 A, because one end of the YBCO current leads is at 77 K, resistive losses and hence the heating is relatively small. Once the current exceeds the temperature-dependent critical current of the YBCO tapes, Joule heating is enhanced. The inset in Figure 5.16(a) shows this effect occurs sooner for the top current lead than the bottom because it is totally surrounded by Tufnol and the cooling relies only on the heat transfer by conduction. We note that the current leads can be re-optimised for J_c measurements above 90 K using DI-BiSCCO tapes if required.

5.5 Description of $J_c(B,T,\theta,\varepsilon)$ probe

The $J_c(B,T,\theta,\varepsilon)$ probe was designed with the current leads optimised for our horizontal magnet system. The top and bottom parts of the probe are shown in Figure 5.17 where the variable-temperature cup was modified to fit with the springboard-shaped sample holder. Figure 5.18 shows detailed apparatus of the springboard-shaped sample holder and thermometry.

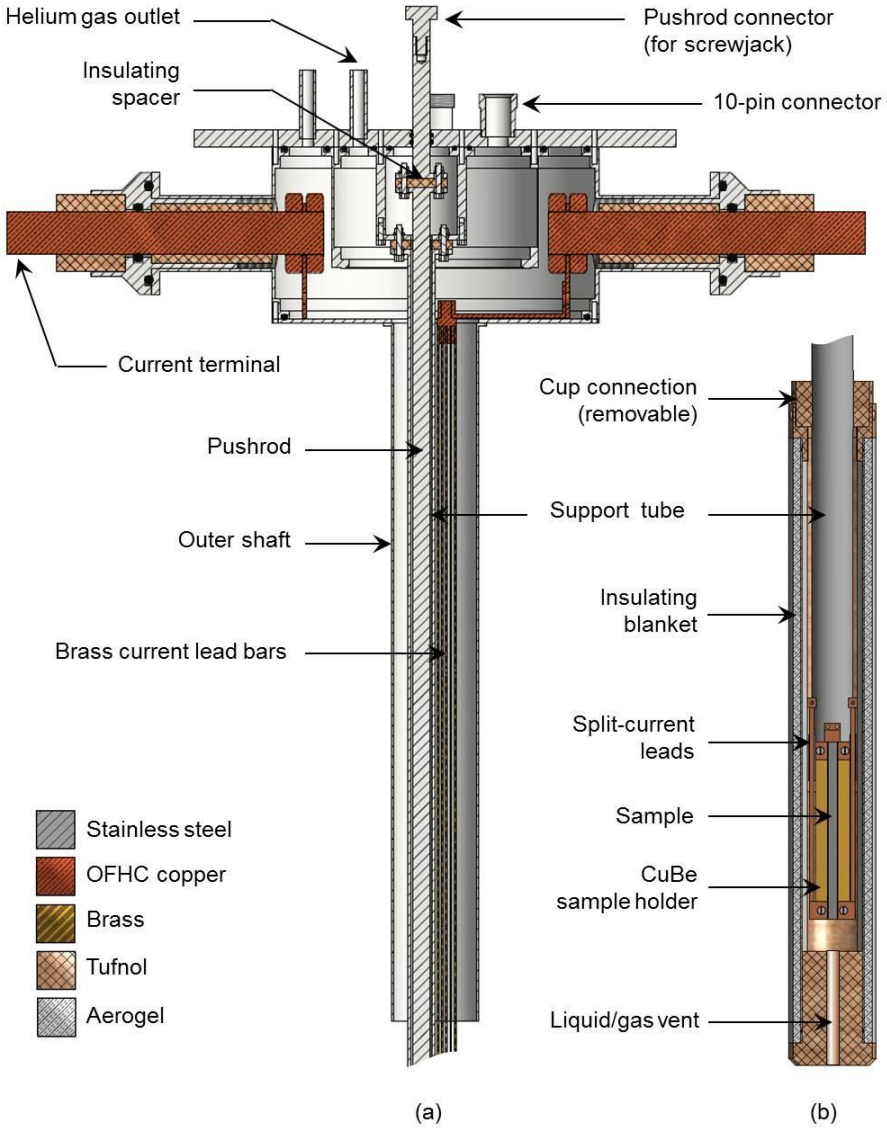

Figure 5.17 Diagram of $J_c(B,T,\theta,\varepsilon)$ probe (a) the top part of the probe including a stack of brass current lead bars and (b) the variable-temperature insulating cup.

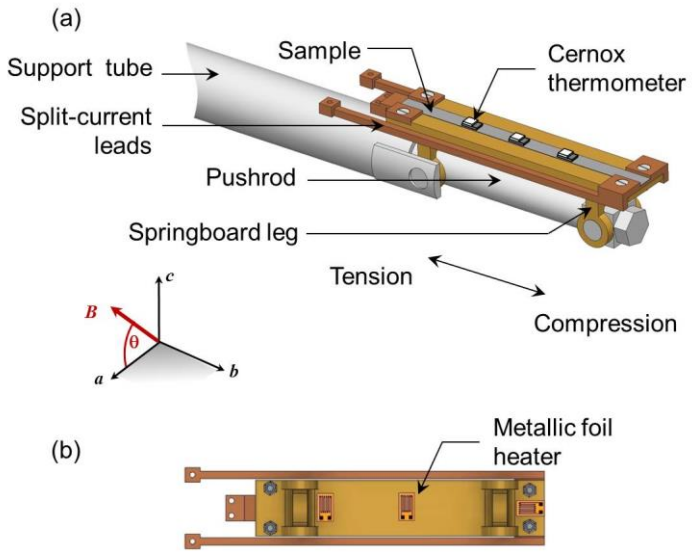

Figure 5.18 (a) Diagram of the springboard-shaped sample holder and thermometry. (b) Metallic foil heaters underneath the sample holder.

Split-current leads and heaters were made flexible due to a requirement of the strain measurements. All heaters were made from a metallic foil-type strain gauge on polyimide substrate and were installed underneath the sample holder. The resistances of the as supplied gauges were 120 Ω. Because of the existence of stainless steel tubes for strain application, cylindrical shape was not an appropriate design for the vapour-cooled current leads. While brass was still used with all the benefits discussed above, the cylindrical shape was changed to a stack of brass bars. Each current lead for the $J_c(B,T,\theta,\varepsilon)$ probe was made from five of 1 mm × 10 mm × 1.0 m brass bars with 1.5-mm gaps between them. Four YBCO (SF4050) tapes were soldered to each current lead from the bottom end up to x = 0.4 m. The total cross-sectional area of each current lead was 50 mm^2 which was the optimum for measurements up to 450 A with D = 0.2, T_{max} = 400 K and b' = 0.3 Lhr^{-1}. The current lead's length at the minimum helium level was 1.0 m. The observed static helium consumption of the probe alone was 0.5 Lhr^{-1}.

5.6 Strain sample holder

Strain is applied to the sample using the modified bending beam apparatus with the springboard-shaped sample holder. The sample holder was made from a copper beryllium alloy (Berylco 25) with good elastic properties, solderability and relatively high resistivity [178]. It was 78 mm in length, 15 mm in width and 2.5 mm in thickness, as shown in Figure 5.19. The sample is soldered directly into a groove that runs along the length of the sample holder and ensures the superconducting component of the sample is parallel to the top surface of the springboard and in the plane of the strain gauges. The final design ensures the springboard is long enough that we do not get current transfer voltages in our measurements. The wide surface of the springboard provides space for the strain gauge, Hall sensor and thermometry. The split-current leads were made from OFHC copper for measurements at liquid helium temperature. Four YBCO (SCS4050) tapes were used for each current lead for measurements in the variable-temperature cup. The pairs of legs at each end were pulled/pushed to adjust the strain on the top surface of the sample holder with the use of JVL's MAC servo motor. The top pair was fixed to the support tube and the second pair to the pushrod. Uniaxial strains of -1.4 % to 1.0 % can be applied to the sample. Finite element analysis of the springboard-shaped sample holder with the applied strain of -1.08 % is shown in Figure 5.20. Strain homogeneities are better than 1 part in 10^5 across the thickness of the superconducting layer and also along the length of the sample between 10-mm voltage taps. In the strain measurements, strain gauges (Vishay WK series) are mounted on the sample holder next to the sample. This allows direct control and monitoring of the strain during initial setup and measurements. At liquid helium temperature, the strain gauges exhibited a positive magnetoresistance of ~180 mΩ at 14 T which corresponds to the effective measured tensile strain of ~0.025 % relative to zero field. This magnetoresistance has been characterised and the measured strain has been corrected. The total uncertainty in the measured strain is better than ±0.02 % for all data taken.

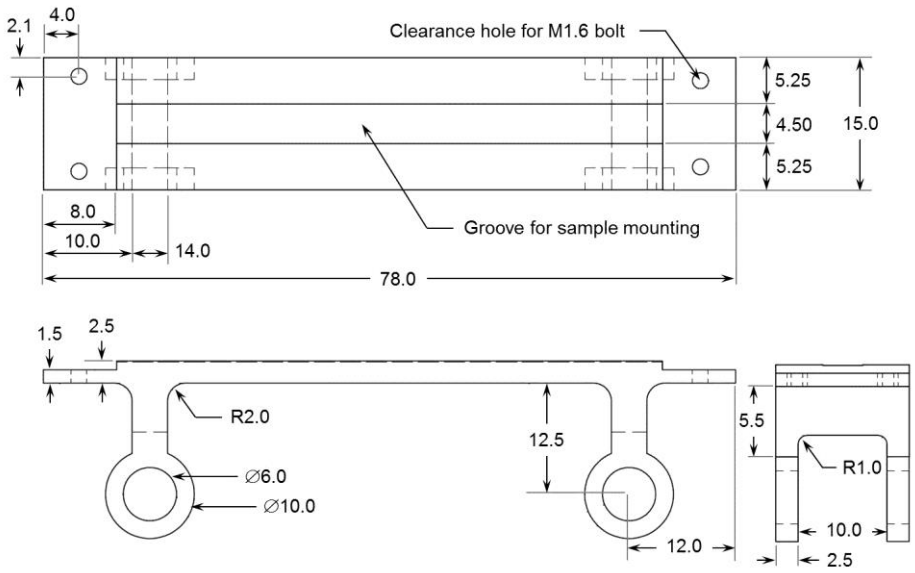

Figure 5.19 Technical drawings of the springboard-shaped sample holder.

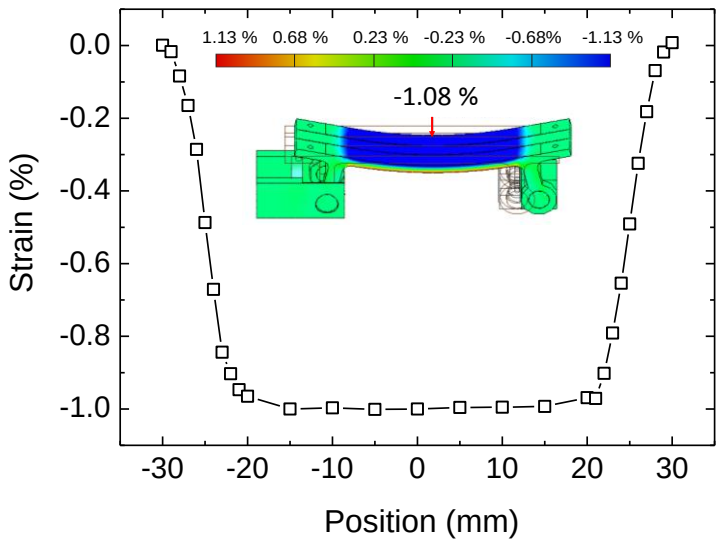

Figure 5.20 Computational data of the strain homogeneity on the top surface of the 2.5-mm-thick springboard-shaped sample holder with an applied strain of -1.08 %. The inset shows a colour plot of the data from finite element analysis.

5.7 Investigation of HTS tapes

J_c measurements were performed on YBCO (SCS4050) tapes using the $J_c(B,T,\theta,\varepsilon)$ probe. The critical currents were defined using a 100 μVm^{-1} electric field criterion. Strain effects on the critical current density of the YBCO tape are presented in Figure 5.21 for measurements in liquid helium and magnetic fields applied normal to the tape surface. At 4.2 K, the effects of strain on YBCO are weak and J_c is reversible over the strain range of -0.6 % in compression to 0.3 % in tension. We present J_c as a function of applied strain extended to -1.3 % to illustrate the capability of our strain apparatus in measuring J_c in compression.

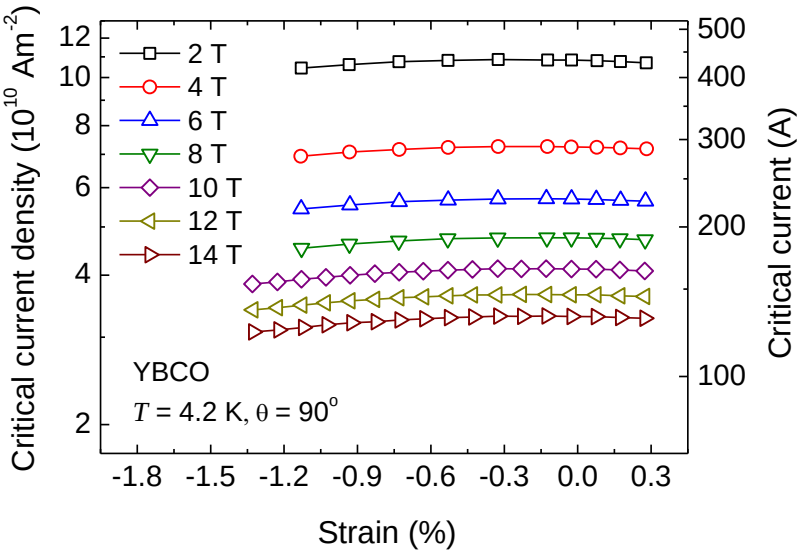

Figure 5.21 Critical current density of a YBCO tape at 4.2 K as a function of applied strain for different magnetic fields normal to the tape surface.

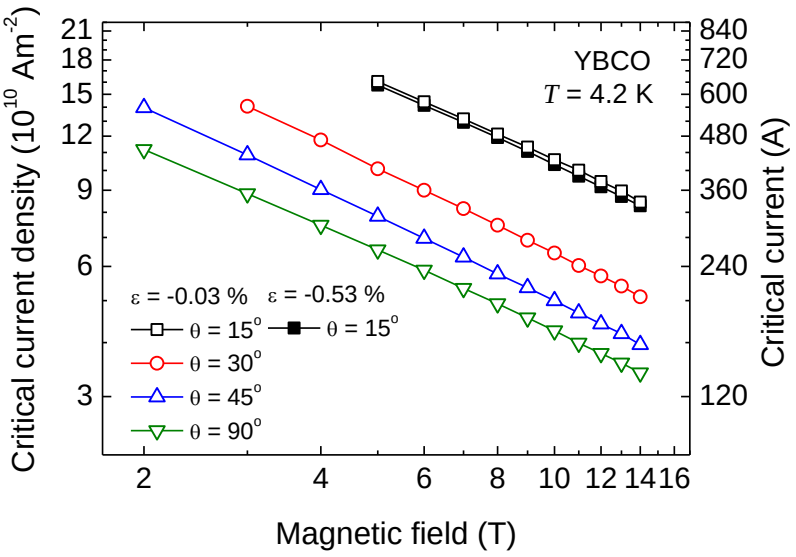

Figure 5.22 Critical current density of a YBCO tape at 4.2 K as a function of applied magnetic field for different strains and angles between the magnetic field and the tape surface.

Figure 5.22 shows the magnetic field dependence of the critical current density for various angles between the fields and the tape surface at ε = -0.03 %. Data for ε = -0.53 % and θ = 15° are also included. J_c of YBCO increases by a factor of 3 when θ changes from 90° to 15°. The anisotropy of YBCO has been analysed based on anisotropic Ginzburg-Landau theory and the anisotropy of 7.0 was found [209].

In Figure 5.23, voltage-current characteristics of the YBCO sample are shown at 20 K and 40 K for different magnetic fields applied normal to the tape surface when ε = 0.0 %. The inset data show that the temperature stability is sufficiently good that no significant change in temperature occurred during the transitions, either from heating of the sample or heating of the current leads made from YBCO tapes. However, the temperature variations are around ±150 mK which is higher than the $J_c(B,T,\theta)$ probe probably due to the larger volume of sample space.

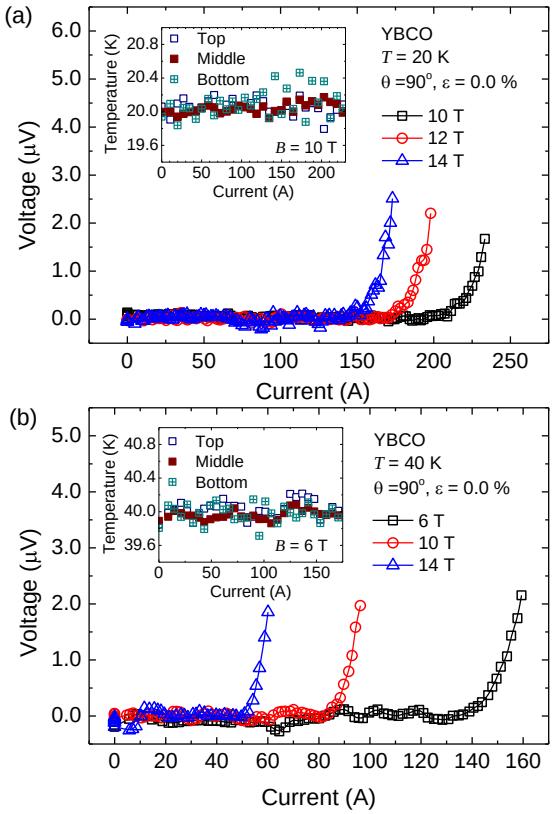

Figure 5.23 (a) Voltage-current characteristics of a YBCO tape at 20 K as a function of applied magnetic field normal to the tape surface for measurements in liquid helium. (b) Similar plots at 40 K. The insets show temperature rising during the transition for data taken at 10 T at 20 K and 6 T at 40 K where the critical currents at 100 μVm^{-1} were 229 A and 153 A, respectively. In both cases, no temperature increase was observed. The temperature deviation was about ±150 mK.

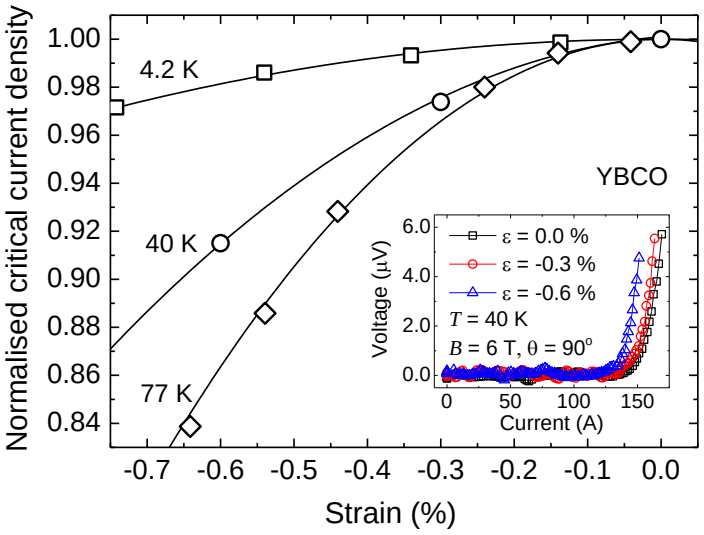

Figure 5.24 Normalised critical current density of YBCO tapes as a function of strain at 4.2 K, 40 K and 77 K. The inset shows voltage-current characteristics of a YBCO tape at 40 K as a function of applied strain with the magnetic field applied normal to the tape surface.

Measurements using the variable-temperature cup were also performed as a function of strain at 40 K in the applied magnetic field of 6 T normal to the tape surface. Voltage-current characteristics are shown in Figure 5.24 (inset) for the applied strains of 0.0 %, -0.3 % and -0.6 %. The noise in the base line of the measurements was several hundred nanovolts peak-to-peak and was a result of the stability of the temperature control. The critical current density obtained as a function of strain has been normalised and plotted in Figure 5.24, together with two other temperatures for comparison. Table 5.5 summarises the measurement uncertainty for critical current measurements using the $J_c(B,T,\theta)$ and $J_c(B,T,\theta,\varepsilon)$ probes operated in liquid nitrogen and liquid helium. Uncertainty of the measured critical current is predominantly due to the temperature variation. The proportional (P), integral (I) and derivative (D) values of the temperature controllers were the same for all measurements and were equal to 50, 20 and 0 respectively. We are confident that the variations in

temperature can be reduced if necessary with further optimisation of the feedback circuit (i.e. PID parameters). These J_c results confirm the probe operates successfully.

5.8 Concluding comments

We have successfully designed, constructed and commissioned a probe for $J_c(B,T,\theta,\varepsilon)$ measurements on high temperature superconductors. The probe was designed and optimised for Durham's split-pair horizontal magnet system, however, design considerations and detailed calculations were discussed and we have produced a generalised solution for optimisation of the vapour-cooled brass current leads. The optimum cross-sectional area of the current leads has been calculated which include consideration of the duty cycle of the measurements, the static helium consumption of the cryostat and the maximum safe temperature of the leads since over-current operation consumes less cryogen. This work shows that beyond the special case of magnet currents leads continuously running at constant current, more generally one can expect that 'hot' current leads will be most efficient for cryogenic applications. The probe used an insulating enclosure for the variable-temperature measurements. The total uncertainty of the sample's temperature during J_c measurements was typically ~0.2 K. This was influenced by the design and thermometry of the probe and the control system. Uniaxial compressive and tensile strains were obtained using the springboard-shaped sample holder. Strains of -1.4 % to 1.0 % can be applied with a total uncertainty of the measured strain better than ±0.02 %.

Table 5.5 Measurement uncertainty in operation of the $J_c(B,T,\theta)$ and $J_c(B,T,\theta,\varepsilon)$ probes in liquid nitrogen and liquid helium.

Quantity	**Maximum uncertainty**	
	Liquid nitrogen	**Liquid helium**
$J_c(B,T,\theta)$ probe		
Temperature	180 mK	80 mK
Critical current	1.1 % mv [a]	0.5 % mv
$J_c(B,T,\theta,\varepsilon)$ probe		
Temperature	200 mK	150 mK
Critical current	1.2 % mv	0.9 % mv
Strain	0.02 % [b]	0.02 %

[a] Percentage of the measured value.

[b] Percentage strain as from the definition $\varepsilon = \Delta L/L_0 \times 100$ %.

Chapter 6

Critical current density in polycrystalline superconductors

6.1 Introduction

Following the preliminary measurements of the critical current density on the DI-BiSCCO tapes in Chapter 4, detailed experimental and theoretical studies were performed, not only for BiSCCO but also for HTS YBCO and LTS Nb_3Sn. All the variable-strain transport measurements on BiSCCO in this chapter were completed by the author of this thesis as well as all of the analysis. The measurements on YBCO and Nb_3Sn were completed by Mark Raine and Drs Yeekin Tsui and Joshua Higgins. The central idea or hypothesis in this chapter is that a single mechanism, based on flux flow along the grain boundaries, can explain the functional form of J_c in polycrystalline LTS and HTS regardless of the pairing mechanism operating.

The next two sections in this chapter provide reviews of topics in the literature relevant for the analysis and interpretation of the J_c data presented. Sections 6.2 and 6.3 consider: Grain boundaries and Theoretical analysis of SNS junctions. Section 6.4 considers Samples and experimental methods. Thereafter, J_c data is presented in Section 6.5 as a function of magnetic field, field orientation, temperature and strain for BiSCCO, YBCO and Nb_3Sn and analysed using the SNS model. Finally we provide comment and conclusions.

6.2 Grain boundaries: review of structure and properties

It is well known from experimental work and theoretical considerations that perfect single crystals of superconductors carry no bulk critical current density [58, 210]. Grain boundaries control materials properties since their atomic configurations are locally different from that of the grains so many physical properties are locally quite different to the bulk. In LTS, it has long been known that decreasing the grain size or equivalently increasing the density of grain boundaries increases J_c [181, 211]. For polycrystalline HTS the strong effect on J_c of the misorientation of the grains has led to the idea that grain boundaries are weak-links [6, 212, 213], not pinning centres as found in the LTS. In general, the rotation of a crystal around an axis parallel to the plane of the grain boundary leads to a *tilt* grain boundary and a rotation around an axis normal to the plane leads to a *twist* grain boundary. For example, [001]-tilt grain boundary has the rotation around the *c*-axis so the misorientation occurs along the *ab*-plane (where superconductivity takes place) and is called the *in-plane misorientation*. On the other hand, the *out-of-plane misorientation* occurs in the *c*-direction such as [100]-tilt grain boundary. Given the negligible anisotropy of the HTS in the *ab*-plane, we expect that the in-plane misorientation will not affect the anisotropic properties of polycrystalline samples as strongly as out-of-plane misorientation does.

A grain boundary with low-angle in-plane misorientation angle consists of arrays of separated dislocations which are clean (from impurities and defects) and well-defined as seen from the transmission electron microscopy (TEM) studies [214]. The transition from low-angle to high-angle grain boundaries, at which the separated dislocations are so close and overlap, is around 10° [215] depending on material and the temperature. An important difference between low-angle and high-angle grain boundaries is the strength of coupling across the boundary [215] and hence leads to significantly different physical properties. For YBCO and BiSCCO, the presence of the grain boundary faceting with the size of ~100 nm has been reported [216-218]

which is dependent on the different growth modes. Therefore, grain boundaries in these materials can have large local variations in properties.

In order to investigate the local properties of the grain boundaries in HTS, several approaches have been used to prepare a single grain boundary such as bicrystal technology, biepitaxial process and step-edge junctions [214]. Current-voltage characteristic of the grain boundaries clearly shows the superconducting-normal-superconducting (SNS) Josephson junction behaviour [148] which can be described with the Time-Dependent Ginzburg-Landau (TDGL) equations [219] where the critical current density is determined by flux flow along the grain boundaries. Magneto-optical images of YBCO samples and light microscopy images of the underlying Ni substrate together reveal flux penetration into the grain boundary regions where the superconducting order parameter is depressed [220]. Although an accurate thickness of the grain boundary is ambiguous, grain boundaries with higher angle are considered thicker than the grain boundaries with lower angle so there exists a larger suppression of the superconducting properties and the critical current density is lower. An exponential decrease in J_c as a function of misorientation angle has been found [6, 212, 213], consistent with this correlation.

6.3 Flux flow along an SNS junction

Recent theoretical work on J_c in an SNS junction in high magnetic fields has been published by Carty and Hampshire [221] (members of the Durham group) and is summarised here. In low magnetic fields, J_c through a narrow SNS Josephson junction is given by the familiar sinc function [18, 222]:

$$J_c = \frac{\hbar J^*(0)}{2ew(d+\lambda_{(S)})B}\left|\sin\frac{2ew(d+\lambda_{(S)})B}{\hbar}\right| \qquad (6.1)$$

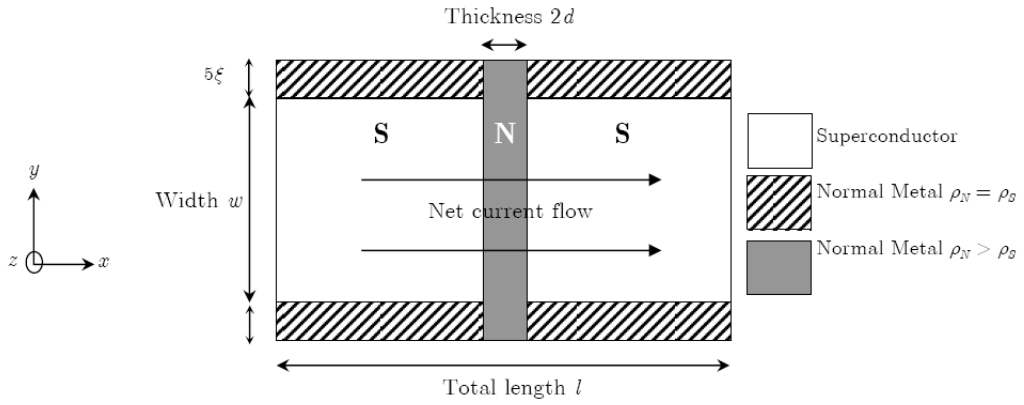

Figure 6.1 Schematic diagram of the SNS junction model [221]. The junction consists of two superconducting components separated by a normal metal barrier that limits the current flow. This barrier represents the grain boundary in polycrystalline superconductor.

where *w* is the width of the junction, $(d + \lambda_{(S)})$ is known as the effective half-thickness of the junction, $\lambda_{(S)}$ is the penetration depth of the superconducting component and *B* is the applied magnetic field. Figure 6.1 shows a diagram of an SNS junction where the normal metal barrier limits the current flow from one superconducting component to another.

For anisotropic materials, parameters that are determined by the direction of current flow (associated with the effective mass of the carriers) are distinguished by an uppercase star (e.g. B_{c2}^{*}) from those determined by the angle of the applied field with respect to the crystallographic axes (e.g. B_{c2}). Equation (6.1) does not consider the complex spatial variation of the order parameter in the mixed state where fluxon formation occurs in the junction and in the superconductor. TDGL computation has confirmed that for wide junctions or in high magnetic fields where many fluxons are in the junction, the sine term which is associated with phase of the superelectrons is averaged out to $1/\sqrt{2}$ [221]. When the superconductor is in the mixed state and the magnetic field produces many fluxons in the junction, the factor $(d + \lambda_{(S)})$ is replaced by $(d + \xi_{(S)})$ where $\xi_{(S)}$ is the coherence length of the superconducting

component. The general solution for the depairing current density (J_{D-J}) through a one-dimensional SNS junction that accounts for the depression of the order parameter by magnetic field is given by [221]

$$J_{D-J} = \frac{\rho_{(S)}}{\rho_{(N)}} \frac{B_{c2}^{*}}{\mu_0 \lambda_{(S)}^{*} \kappa_{GL}^{*}} \hat{\psi}_{\infty}^{2} \left(\frac{B}{B_{c2}} \right)^{1/2} \left(\frac{2B}{B_{c2}} \frac{d^2}{\xi_{(S)}^2} + \frac{1}{\gamma} \right)^{1/2} \tilde{F}^2 \exp\left(-\frac{B\gamma}{B_{c2}} \frac{d^2}{\xi_{(S)}^2} \right), \quad (6.2)$$

where

$$\tilde{F} = \sqrt{\left[\frac{\rho_{(S)}}{\sqrt{2}\rho_{(N)}} \frac{B\gamma}{B_{c2}} \frac{d}{\xi_{(S)}} \left(1 - \frac{1}{(2B\gamma / B_{c2})(d^2 / \xi_{(S)}^2) + 1} \right) \right]^2 + 1} - \frac{\rho_{(S)}}{\sqrt{2}\rho_{(N)}} \frac{B\gamma}{B_{c2}} \frac{d}{\xi_{(S)}} \left(1 - \frac{1}{(2B\gamma / B_{c2})(d^2 / \xi_{(S)}^2) + 1} \right), \quad (6.3)$$

$\hat{\psi}_{\infty}^{2} = (1 - B/B_{c2})$, $\gamma^2 = (1 + eBd^2/\hbar)/(6 + eBd^2/\hbar)$, $\rho_{(S)}$ and $\rho_{(N)}$ are normal state resistivities of the superconducting component and the normal component, respectively [223]. In conclusion $J^{*}(0)$ in (6.1) can be equated to J_{D-J} of the junction which gives

$$J_c(B) \approx \frac{1}{\sqrt{2}} \frac{B_{c2}^{*}}{\mu_0 \xi_{(S)}^{*} (\kappa_{GL}^{*})^2} \frac{r\xi_{(S)}^2}{w(d + \xi_{(S)})} \left(\frac{1}{\tilde{b}} \right)^{1/2} \left(\frac{2\tilde{b}d^2}{\xi_{(S)}^2} + \frac{1}{\gamma} \right)^{1/2} \times \tilde{F}^2 (1 - \tilde{b}) \exp\left(-\frac{\tilde{b}\gamma d^2}{\xi_{(S)}^2} \right) \quad (6.4)$$

with the dimensionless units $r = \rho_{(S)}/\rho_{(N)}$ and $\tilde{b} = B/B_{c2}$.

6.4 Samples and experimental methods

Three different types of samples were measured:

i) Nb_3Sn wires manufactured by Bruker EAS using the multifilamentary bronze-route process. The average diameter of the wires was 0.81 mm;
ii) YBCO tapes from SuperPower (SCS4050). The superconducting layer was approximately 4 mm wide and 1 μm thick;
iii) Multifilamentary DI-BiSCCO CA50 tapes supplied by SEI. Detailed description of the tapes was presented in Chapter 4.

6.4.1 Magnetic measurements and Bean's model

Dc magnetisation is measured using a dc magnetometer where the sample is magnetised by a constant magnetic field and a set of pickup coils is used to measure an induced voltage as the sample is moving through the coils [224]. The induced voltage is proportional to the change of flux which can be integrated to give the value of sample's magnetisation (M), typically as a function of the applied magnetic field strength (H). The magnetisation of a hard Type II superconductor exhibits irreversible behaviour. The critical state model, first introduced by Bean [225, 226], provides a picture of how irreversible bulk critical current density flows to create the magnetisation in response to the change of external magnetic field strength. The screening critical current density can be extracted from the $M(H)$ data by using the relation $J_c \propto \Delta M$ with the proportional constant depending on geometry of the sample. ΔM is the difference in magnetisations at increasing field and decreasing field of the hysteresis loop.

The ac susceptibility, on the other hand, is obtained by inductively measuring ac magnetic moment of the sample which is created under a small ac field in the large applied field without any sample motion. The ac moment contains information on

dynamic effects of magnetisation and yields two components of susceptibility: a real component (χ') and an imaginary component (χ''). Ac susceptibility measurements have been used to characterise B_{c2} of the superconductors investigated which characterises the onset of the transition [227].

The magnetisation measurements and ac magnetic susceptibility measurements of Nb_3Sn, YBCO and BiSCCO were completed in the Quantum Design Physical Properties Measurement System© in magnetic fields up to 8.5 T at different temperatures. In the magnetisation measurements, hysteresis loops were obtained in order to calculate the magnetisation J_c using Bean's critical state model [226]. The ac magnetic susceptibility data were used to find $B_{c2}(T)$.

6.4.2 Transport measurements

Transport measurements rely on current flow between the measuring contacts. The measurements are usually performed using the standard four-terminal technique, with two current contacts and two voltage taps, to ensure that only the sample's resistance is measured [190]. Transport J_c measurements are carried out by passing an increasing current to the sample while the voltage across the sample is monitored. A resulting voltage-current characteristic is obtained and the critical current is defined by applying an arbitrary electric field or resistivity criterion [228]. J_c obtained from transport measurement therefore reflects the real current carrying capacity of the sample although it is dependent on the criterion used to define the non-dissipative state.

Transport technique is also useful for T_c measurements where resistivity of the sample is measured as a function of temperature. T_c is normally determined at the temperature that sample's resistivity drops to zero. However, broadening of the resistive transition in magnetic field usually occurs especially in HTS [229-233], therefore the ac susceptibility measurements are more convenient in terms of

determining T_c. Other limitation of the transport measurements includes the requirement to fabricate electrical contacts which makes them difficult for a small sample and impossible for sample in powder form. Moreover, measuring J_c in low magnetic fields can be restricted in high-J_c superconductors due to the heating problem. In these cases, the magnetic measurements are preferable.

The transport J_c measurements of Nb_3Sn were made using the standard four-terminal technique and the critical currents determined using a 10 μVm^{-1} electric field criterion. J_c of YBCO and BiSCCO were determined at 100 μVm^{-1}. The critical current densities were calculated using the critical currents divided by the unstrained cross-sectional area of the superconducting components. The transport J_c measurements on Nb_3Sn wires were performed at 4.2 K in magnetic fields up to 14.5 T in our vertical superconducting magnet using the purpose-built strain probe which includes a copper beryllium spring sample holder [178, 194]. The measurements on YBCO and BiSCCO tapes were performed at 77 K in magnetic fields up to 0.7 T in our conventional iron-cored electromagnet and at 4.2 K in magnetic fields up to 14 T in a 40 mm bore horizontal split-pair superconducting magnet at different angles between the field and the surface of YBCO and BiSCCO tapes. The strain measurements were carried out using the springboard-shaped copper beryllium sample holder (as shown in Fig. 5.18) for applying strains up to 0.3 % in tension and -1.4 % in compression [154, 234].

6.5 Experimental results and discussion

Here we consider polycrystalline superconductors as a collection of SNS junctions. The superconducting components represent the grains of the superconducting material and the normal junctions represent the grain boundaries.

6.5.1 Temperature and magnetic field dependence of J_c

Figure 6.2 shows the magnetisation J_c as a function of applied magnetic field and identifies the self-field regime, the power-law regime and the exponential regime where the product of $\tilde{F}^2$, $(1-\tilde{b})$ and the exponential field-dependent term is important. The solid lines are fits to the data using (6.4) where the Ginzburg-Landau parameter is 33, 94 and 139 for Nb_3Sn, YBCO and BiSCCO respectively [171]. At the very lowest fields, the (log-log) insets show that J_c is almost field-independent, consistent with the self-field produced by the flowing current being much higher than the external magnetic field. At low fields, $J_c(B)$ shows power-law behaviour with an exponent of -0.5, consistent with (6.4). The power-law behaviour occurs over a wider range of fields and temperatures for YBCO than Nb_3Sn and BiSCCO and is attributed to thinner grain boundaries. At sufficiently high fields, there is a cross-over from power-law behaviour to exponential behaviour which has been observed before [235-238]. Note that in other (lower J_c) YBCO samples, $J_c(B)$ is exponential over several orders of magnitude/a much larger range of field and temperature phase space [239] than shown here, which is consistent with attributing the field dependence to the nature of the grain boundaries and not the intrinsic properties of any specific superconducting material. For BiSCCO, J_c is a significantly smaller fraction of the depairing current density than in say YBCO. When fitting the J_c data of BiSCCO at low fields, there is a very much stronger temperature dependence than that found in Nb_3Sn or YBCO which cannot be explained by the temperature dependence of B_{c2}. This temperature dependence is attributed to the normal state property r as shown in the additional inset of Figure 6.2(c) and described empirically by

$$r(T) = r_0 \exp(T/T_0), \tag{6.5}$$

where $r_0 = 3.6\times10^{-2}$ and T_0 = 36 K in the fit to the data.

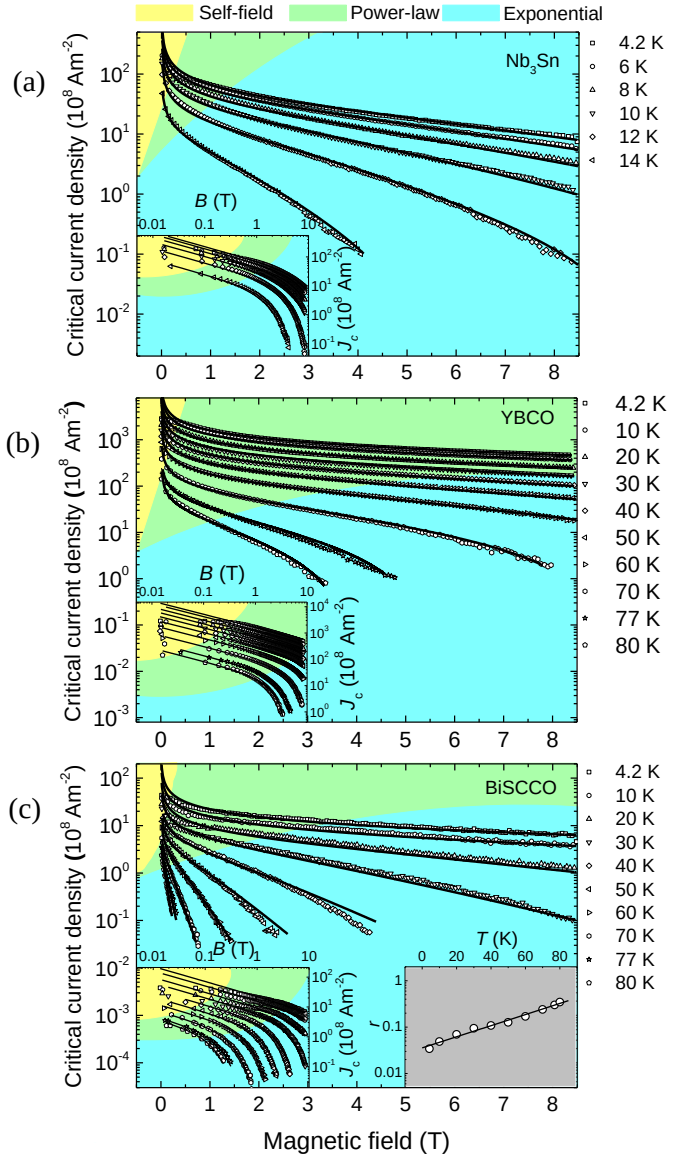

Figure 6.2 (a) Log-linear plots of magnetisation critical current density calculated using Bean's critical state model [226] as a function of magnetic field for a Nb_3Sn wire, showing the self-field regime (yellow), power-law regime (green) and exponential regime (blue). The inset is the J_c data in log-log plots showing the power-law behaviour in low fields. The solid lines are fits to (6.4). (b) and (c) are similar plots for YBCO and BiSCCO tapes for the field parallel to the *c*-axis. The additional inset in (c) shows the temperature dependence of r consistent with semiconducting behaviour of the BiSCCO grain boundaries.

The temperature dependence of r in BiSCCO is consistent with $\rho_{(N)}$ (associated with the grain boundary) rapidly increasing with decreasing temperature which is expected for a semiconducting grain boundary. The functional form of $B_{c2}(T)$ has been derived for each of the three materials studied here by fitting the J_c data to (6.4). In Figure 6.3 and Figure 6.4, these functional forms are compared with the B_{c2} values obtained from the in-house ac magnetic susceptibility measurements as well with those from literature. B_{c2} from ac magnetic susceptibility measurements has been characterised at 1 %, 5 % and 50 % of the full screening (M'_{fs}) in order to quantify how sensitive the values are to the criterion used.

For Nb_3Sn, which is one of the important superconducting materials used in the ITER tokamak [240], there is much data in the literature on samples fabricated by different routes and with different microstructure. $B_{c2}(T)$ obeys the WHH equation and can be characterised by

$$B_{c2}(T) = B_{c2}(0)(1-\tilde{t}^{1.5}) \tag{6.6}$$

where $\tilde{t} = T/T_c$ is the reduced temperature [36, 241, 242]. The data at 1 % of full screening give the values of $B_{c2}(0)$ and T_c of 26.3 T and 16.7 K which are similar to those derived from the J_c data (26.3 T and 16.2 K) and the literature data. For HTS materials, the fundamental properties and their variation with sample preparation and microstructure are far less well known, particularly at low temperatures where $B_{c2}(T)$ values are high. Nevertheless for YBCO, pulsed field $B_{c2}(T)$ data are available up to 400 T [64] and are plotted in Figure 6.4. The J_c data of YBCO have been fitted using $B_{c2}(T)$ in the form

$$B_{c2}(T) = B_{c2}(0)(1-\tilde{t}^{0.61}) \tag{6.7}$$

where the values of $B_{c2}(0)$ and T_c are 68.5 T and 87.6 K. The temperature dependence of B_{c2} from (6.7) only differs significantly from the pulsed field data at 25 K and below where an upward curvature in $B_{c2}(T)$ is found. This curvature may arise from

our assumption that κ_{GL} is independent of temperature, or differences between the single crystal sample used for pulsed field measurements and the tape used in this work which is optimised for high J_c. Further measurements in very high fields are required to explain the differences. A concave curvature of $B_{c2}(T)$ has been observed in several BiSCCO systems [233, 243, 244] which can be characterised using a scaling function

$$B_{c2}(T) = B_{c2}(0)(1-\tilde{t}^{0.5})^{2.1} \tag{6.8}$$

where $B_{c2}(0)$ and T_c from the J_c data are 84.5 T and 110.8 K, respectively. The extrapolated zero-field T_c values found from the ac magnetisation data in Figure 6.3 are lower than the measured zero-field T_c values because we have only used the in-field data to provide the fits. The data in Figure 6.4 show that there is reasonably good agreement between the reduced temperature dependence of B_{c2} obtained from different measurements on different samples. Also shown in Figure 6.4 are values of $\beta'(T)$ which were found by assuming that in the high field regime, in fields not too close to $B_{c2}(T)$, we can simplify the functional form of J_c and consider it to be proportional to $\exp[-B/\beta'(T)]$ similar to $J_c(B)$ in Chapter 4. For YBCO, the measurements were not done in sufficiently high magnetic fields to reach the high-field exponential regime at low temperatures. Nevertheless the data in Figure 6.4 show that the temperature dependence of $\beta'(T)$ is similar to that of $B_{c2}(T)$ for all three materials (where comparison is available) and leads to an empirical description of d as equal to a few coherence lengths through the equation [245, 246]:

$$d = s[\xi_{(S)}(T) - d_0] \tag{6.9}$$

where s and d_0 are constants. Comparing (6.4) to the functional form of J_c used in pinning given by in Chapter 2 (Eqn. 2.20), although (6.4) is mathematically more complicated, it describes $J_c(B)$ in both low-field and high-field limits without any additional parameters that do not have a physical meaning.

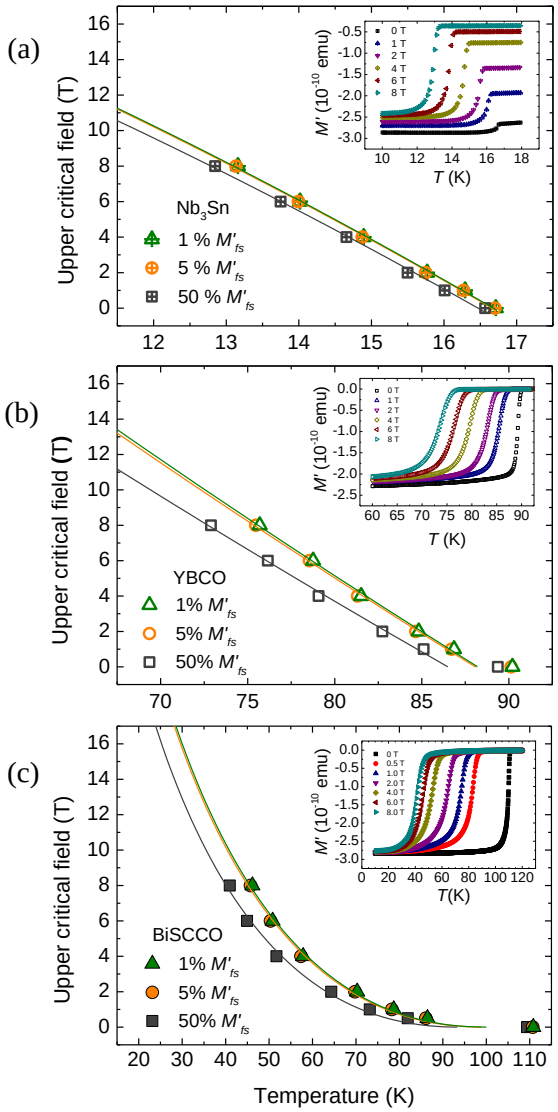

Figure 6.3 (a) Upper critical field of Nb_3Sn versus temperature obtained from ac magnetic susceptibility measurements (inset). The B_{c2} is shown at 1 %, 5 % and 50 % of the full screening (M'_{fs}). The solid lines are fits to the in-field data with (6.6), giving the values of $B_{c2}(0)$ [T_c] of 26.3 T [16.7 K], 26.3 T [16.7 K] and 25.3 T [16.5 K]. (b) Equivalent YBCO data with the field applied along the *c*-axis. The solid lines are fits to the data with (6.7), giving the values of $B_{c2}(0)$ [T_c] of 89.0 T [88.2 K], 88.2 T [88.1 K] and 79.6 T [86.5K]. (c) Equivalent BiSCCO data where the solid line fits are (6.8) with fitting parameters of 84.5 T [100.2 K], 83.7 T [99.7 K] and 74.4 T [93.7 K] respectively.

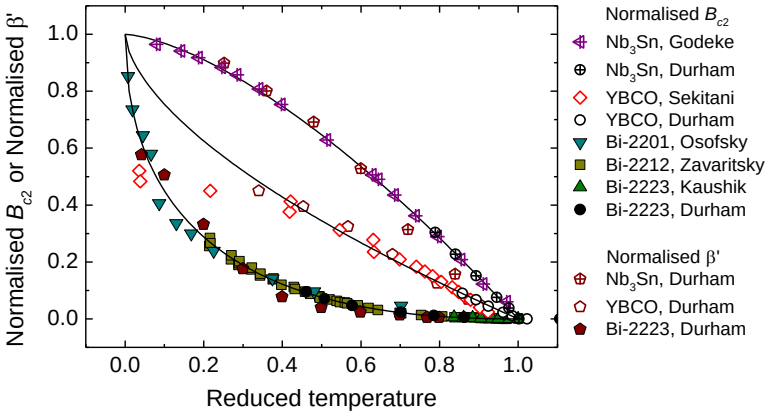

Figure 6.4 Normalised B_{c2} and β´ as a function of reduced temperature for Nb_3Sn, YBCO and BiSCCO. Durham's B_{c2} data are taken from Figure 6.3 at 1 % M'_{fs}. Durham's β´ data are taken from the magnetisation J_c fitted in the high field regime. β´(0) for Nb_3Sn, YBCO and BiSCCO are 6.8 T, 23.4 T and 13.5 T respectively. The lines describe the reduced temperature relations for B_{c2} given by (6.6), (6.7) and (6.8) which are obtained from fits to the J_c data. The data from literature are from Godeke [242], Sekitani [64], Osofsky [243], Zavaritsky [244] and Kaushik [233].

6.5.2 Angular dependence of J_c

The anisotropy of YBCO and BiSCCO can be described using the anisotropic Ginzburg-Landau theory which relates the angle θ between the magnetic field and the tape surface using [19]

$$B_{c2}(\theta) = B_{c2}(90°)\left(\sin^2\theta + \frac{1}{\Gamma_{\text{eff}}^2}\cos^2\theta\right)^{-1/2} \qquad (6.10)$$

similar to (2.9) but Γ_{eff} here is the effective anisotropy obtained from the J_c data. In this chapter, YBCO and BiSCCO are treated as anisotropic layered superconductors with continuum 3D behaviour. Although a weak Josephson coupling between superconducting layers in BiSCCO leads to discrete 2D behaviour at low temperature where the Lawrence-Doniach theory [23] is more accurate, the B_{c2} values calculated

from these two theories are only significantly different at very low θ and are almost indistinguishable for very highly anisotropic materials and the data considered here. Note that in Chapter 4, the anisotropic properties of BiSCCO were assumed to be two-dimensional (i.e. $\Gamma \rightarrow \infty$), therefore any deviation from two-dimensional behaviour was attributed to the misalignment of the grains. Here Γ_{eff} characterises the anisotropy of superconducting parameter, together with grain misalignment (as discussed below). The angular dependence of J_c is shown in Figure 6.5 for YBCO and BiSCCO. Equations (6.4) and (6.10) imply universal scaling behaviour for the angular dependence of J_c as a function of $B(\sin^2\theta + \Gamma_{eff}^{-2}\cos^2\theta)^{1/2}$. This universality is confirmed in the insets for several magnetic fields and angles. The effective anisotropy obtained for YBCO and BiSCCO is 7.0 and 7.8 respectively, both within the range of values quoted in the literature. The YBCO sample used in this work is fabricated by deposition of YBCO film onto substrates with relatively good crystallographic alignment, therefore the effective anisotropy obtained is consistent with the literature values of 3 - 8 [22, 222, 247]. For BiSCCO, the value obtained is at the low end of the range reported in the literature (Γ = 3 - 150) [34, 68, 248, 249]. This is because Γ_{eff} considered here (which is extracted from the experimental J_c data) characterises both anisotropy and grain misalignment in the *c*-direction of BiSCCO tapes and in these PIT materials, the misalignment is significant - probably about 10 degrees (cf Fig. 4.9).

6.5.3 Strain dependence of J_c

In Figure 6.6 (a) - (c), the normalised critical current density, $J_n = J_c(\varepsilon_a)/J_c(\varepsilon_p)$, is shown as a function of relative strain ($\varepsilon_r = \varepsilon_a - \varepsilon_p$ where ε_a is the applied strain and ε_p is the strain at which the maximum of J_c occurs) for Nb_3Sn and YBCO.

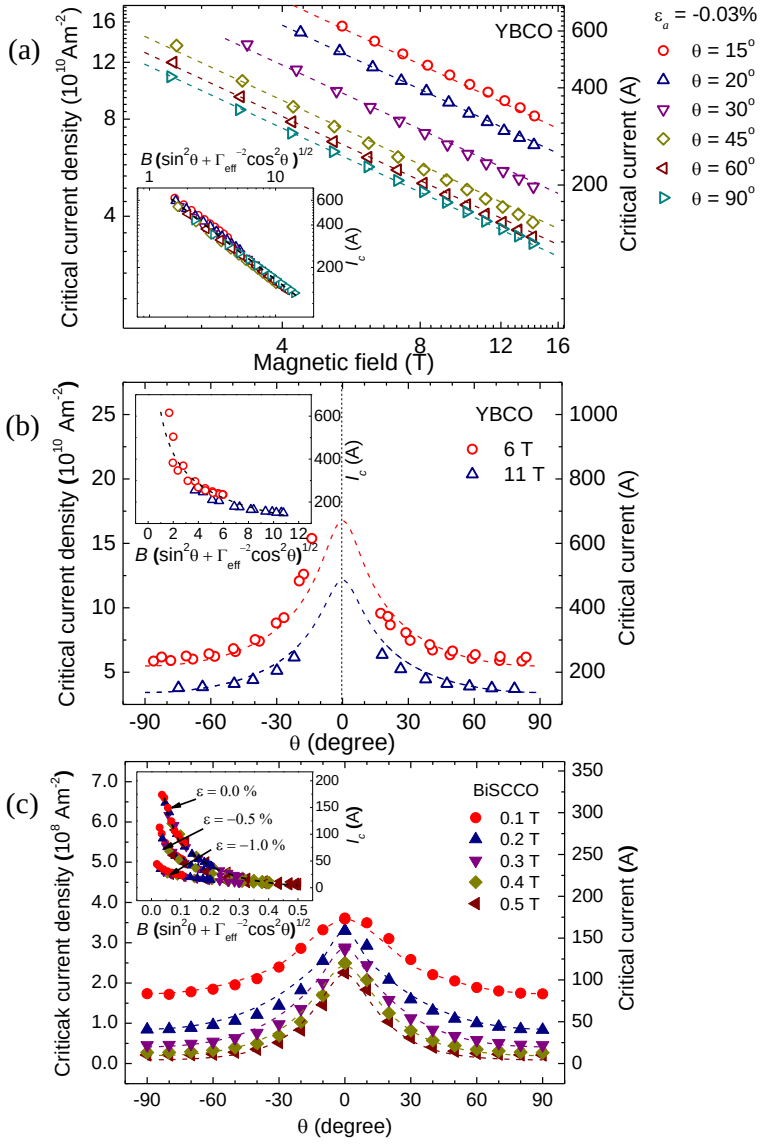

Figure 6.5 (a) Transport critical current density of YBCO tape at 4.2 K versus magnetic field at different angles between the field and the tape surface. (b) Transport J_c of YBCO tape at 4.2 K versus the angle at 6 T and 11 T. (c) Transport J_c of BiSCCO tapes at 77 K versus the angle for zero applied strain. All insets show the data replotted as a universal curve versus $B(\sin^2\theta + \Gamma_{eff}^{-2}\cos^2\theta)^{1/2}$ where Γ_{eff} is 7.0 for YBCO and 7.8 for BiSCCO. The inset in (c) also includes data at two other strains for BiSCCO. All dotted lines are guides to the eye.

For Nb_3Sn, there is a very strong field dependence expected for the strain dependence of J_n over a reduced field B/B_{c2} changing from 0.3 to 0.5. Changes in J_c caused by strain are accounted for by the strain dependence of the superconducting properties B_{c2} and T_c, as is established for many Nb_3Sn samples [197]. For YBCO, J_n is shown as a function of relative strain for both magnetic field normal and parallel to the tape surface at 77 K. Measurements at 4.2 K were only made with magnetic field oriented normal to the tape surface to keep the currents below ~500 A. At 4.2 K, the ε_p changed from -0.3 % at 2 T to -0.1 % at 14 T as has been reported before [250], although no such change was observed at 77 K. The change in ε_p is shown in Figure 6.7. In addition, unlike Nb_3Sn, J_n of YBCO is an almost universal function of the relative strain, independent of magnetic field over a large range of reduced field from 0.06 to 0.4 at 4.2 K and both field and angle at 77 K. This result means that B_{c2} and s are unaffected by strain (and from WHH theory [36] $\rho_{(S)}$ also) at these temperatures. Therefore the strain dependence of J_c is due to the strain dependence of r and hence $\rho_{(N)}$. Further measurements of $\rho_{(S)}$ and $\rho_{(N)}$ are required to explain why the strain dependence of r is larger at 77 K than at 4.2 K and may require inclusion of the role of grain boundary dislocations as a function of strain [251]. Flux pinning theory does not include normal state properties, therefore it cannot explain such variable strain $J_c(\varepsilon)$ data at all. Changing the grain size for example by a factor of 5 at 77 K in flux pinning models is clearly not physical.

Figure 6.6(b) also shows how the strain dependent r eventually causes the universality to break down in the high-field exponential regime and leads to a less strain-dependent J_n on approaching B_{c2}. Since B_{c2} considered here for YBCO is independent of strain, T_c is also expected to be strain independent. Single-crystal data on YBCO show T_c increases with pressure along the *b*-axis and decreases with pressure along the *a*-axis with an average that is close to strain independent [252]. These data provide support for the strain independent superconducting properties found in this work given that the parameters derived here are sample averaged and one can expect percolative current flow in a twinned YBCO tape.

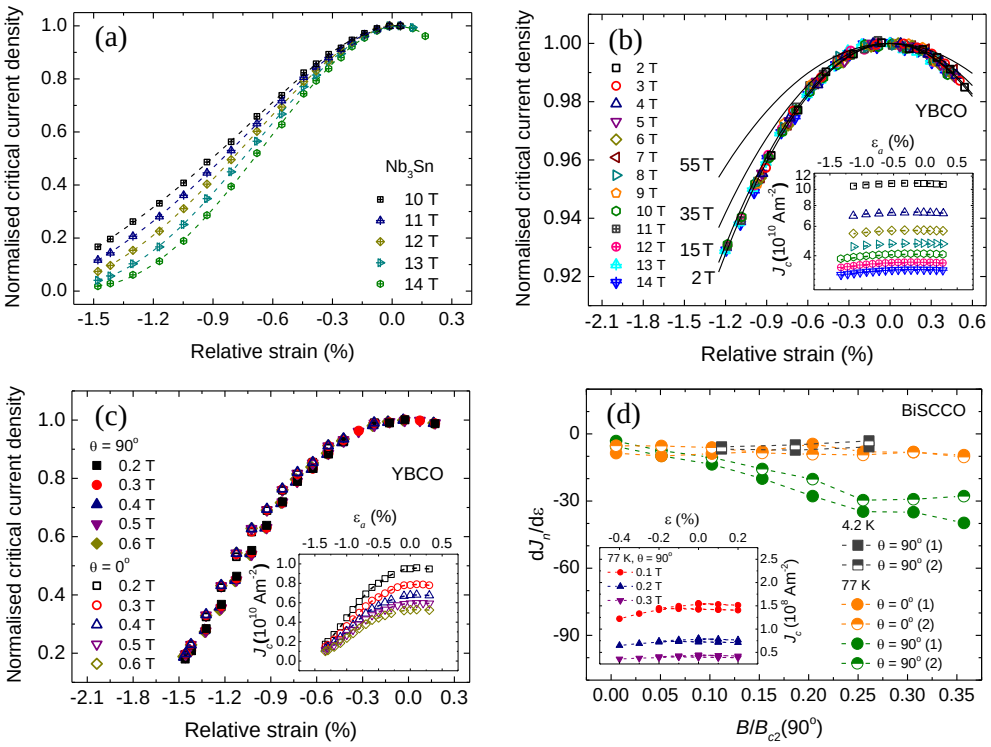

Figure 6.6 (a) Normalised critical current density (J_n) of Nb_3Sn wire versus relative strain at 4.2 K for different applied magnetic fields. (b) J_n of YBCO tape versus relative strain at 4.2 K at different magnetic fields applied normal to the tape surface. The inset shows J_c versus applied strain. J_n of YBCO shows the power-law magnetic field behaviour and ε_p at which the maximum of J_c occurs is a weak function of magnetic field. The solid lines are calculations of J_c using (6.4) and (6.9). (c) J_n of YBCO tape versus relative strain at 77 K for different fields applied normal and parallel to the tape surface. The inset shows J_c versus applied strain for parallel fields only. (d) Change in J_n with respect to strain ($dJ_n/d\varepsilon$) as a function of reduced magnetic field $B/B_{c2}(90^o)$ for BiSCCO tapes at 4.2 K and 77 K for two different field orientations. The inset shows J_c versus applied strain. All dotted lines are guides to the eye.

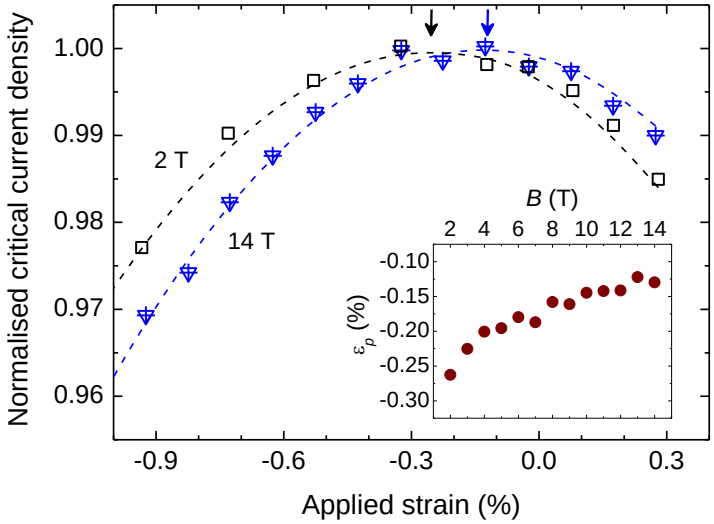

Figure 6.7 Normalised critical current density of YBCO tape at 4.2 K as a function of applied strain for the magnetic fields of 2 T and 14 T applied normal to the tape surface. Dotted lines are guides to the eye. The arrow shows peak strain (ε_p) for each magnetic field. The inset shows ε_p versus magnetic field.

Accurate measurements of the strain dependence of J_c in BiSCCO are demanding because the reversible changes in J_c occur over a much smaller range of strain than in YBCO or Nb_3Sn. The inset of Figure 6.6(d) shows the *roof-top* behaviour for $J_c(\varepsilon)$ which has been characterised in the reversible strain region using the change in J_n with strain as a function of reduced field $B/B_{c2}(90°)$. For parallel fields at 77 K and normal fields at 4.2 K, J_c is in the power-law regime and the strain dependence of J_n is almost independent of magnetic field which suggests that B_{c2} and s are unaffected by strain as also found in YBCO. However, for normal fields at 77 K, J_c is in the exponential regime and J_n is increasingly strain sensitive as the applied field increases which cannot be explained by the strain dependence of r. An increase of ~5 % in d for a tensile strain of 1 % can explain this increasing strain sensitivity, although without data at much higher fields one cannot determine whether this is due to the change in B_{c2} [253] or s.

Table 6.1 The value of fitting parameters in (6.4) and (6.9) fitted to the magnetisation J_c data shown in Figure 6.2.

	r (T = 0)	w	s	T_c	d_0
Nb_3Sn	1.0	4.2 μm	1.9	16.2 K	0
YBCO	1.0	122 nm	1.2	87.6 K	0
BiSCCO	3.6×10^{-2}	122 nm	6.0	110.8 K	2.0 nm

6.5.4 General interpretation of the results and fitting parameters

Table 6.1 summarises the fitting parameters in (6.4) and (6.9) for the fits in Figure 6.2. The r parameter is unity and temperature independent for Nb_3Sn, which is an intermetallic compound, and YBCO, which has low-angle grain boundaries. These results imply that the grain boundaries have a similar temperature-dependent resistivity to the grains and so are metallic. For BiSCCO, r is small and temperature dependent as shown in (6.5) and the inset in Figure 6.2(c) which implies the grain boundaries are highly resistive with semiconducting behaviour. The w parameter, which is strongly correlated with r (the ratio r/w is fixed in the fitting) and characterises the effective widths of the junctions, can change without significant changes in the quality of the fit for BiSCCO. Therefore, w value obtained for YBCO is used. The presence of w explains why flux pinning theory has been so successful historically in explaining LTS materials since the edges of the junctions can be considered as pinning sites. In Nb_3Sn, w is a few microns, about a factor of 5 - 10 larger than the grain size [254], which suggests that several grains act together as a single barrier or equivalently not all triple points separate the barriers (probably because they are not aligned sufficiently with the field direction). The HTS materials YBCO and BiSCCO have much smaller values of w which implies the faceting and

meandering of the grain boundaries divide a grain boundary into many Josephson junctions, or to use the language of flux pinning, there are strong pinning sites along the grain boundaries [95, 255, 256]. The value of d_0 in BiSCCO is sufficiently small that it only affects d at the very lowest temperatures where the fundamental properties are least well known.

There are simple explanations for the values of s found in Table 6.1: s is small in YBCO because B_{c2} is not dependent on strain and the low-angle grain boundaries are thin; s is larger in Nb_3Sn because (unlike YBCO) the local strain depresses the superconductivity near the grain boundaries [241] and s is large in BiSCCO because the PIT route produces relatively large angle of the grain boundaries. Detailed compositional and structural information near the grain boundaries will be necessary to provide a more comprehensive explanation for the s values and the thicknesses of the junctions.

Similar field-dependence behaviour of J_c - the power-law dependence in low fields and the exponential dependence in high fields - has been observed before in several studies including BiSCCO tapes, epitaxial YBCO thin films, silver clamped BiSCCO thick films and NbTi wires [235, 236, 238, 239, 257-260]. While the polynomial form of flux pinning scaling laws has been used to describe $J_c(B)$ in LTS, it has long been believed that mechanisms limiting J_c in HTS YBCO and BiSCCO are different in the two magnetic field regimes [235, 238, 261-263]. Simple explanation of the low field power-law dependence is that dissipation in low fields occurs at the weak-link Josephson network [261]. In high fields, however, J_c measurements on powdered samples have suggested that the dissipation is dominated by intragranular flux motion [238, 263]. Alternative explanations are also available in the literature - the parallel path model [263] proposed for high-quality BiSCCO tapes describes J_c as a summation of weak-link ($4° < \varphi < 8°$) and strong-link ($\varphi < 4°$) contributions which are both exponential field-dependence. The Josephson network is not included in the model and the low-field dissipation is instead explained by flux motion at the grain

boundaries. This analysis is useful in terms of revealing the grain boundary networks in polycrystalline superconductors. Nevertheless, it is completely based on a comparison of the normalised J_c of the tape and the powdered samples which contains an ambiguity of data analysis. Moreover, measurements on a 2°-single grain boundary of YBCO [264] illustrated that the $J_c(B)$ does not exhibit only the exponential strong-link behaviour as expected from the parallel path model, but also the power-law behaviour in low fields as expected from the SNS junction model.

6.6 Concluding comments

We described J_c in polycrystalline superconductors by flux flow along the grain boundaries based on the SNS junction model where the grain boundaries are considered as the normal barriers. The model provides an explanation of the J_c data and predicts the critical current density of the polycrystalline Nb_3Sn, YBCO and BiSCCO over a large range of magnetic field and temperature. From a materials engineering point of view, the SNS junction model provides new grain boundary engineering strategies for improving J_c by revealing the properties of the grain boundaries.

Flux pinning theory can provide important insights into how J_c arises but cannot explain the comprehensive J_c data in polycrystalline HTS superconductors such as YBCO. The parallel path model (based on flux pinning) successfully describe the total J_c of BiSCCO tapes using a simple linear combination of J_c from different grain boundary networks. However, it is not a complete model and some essential details are lacking. It should be noted that the parallel path model evaluates local characteristics within the sample, whereas the SNS junction model analyses the average properties of polycrystalline materials.

In the process of investigating J_c, the average superconducting properties of YBCO are found to be unaffected by strain. The isotope effect led to an understanding of the phonon-mediated fundamental mechanism in LTS and explained the strain dependence of B_{c2} in the LTS Nb_3Sn [197]. The lack of any significant evidence for strain affecting the superconducting properties of YBCO and BiSCCO may yet provide an insight into the mechanism that gives rise to the superconductivity in HTS materials [265, 266].

Chapter 7

Effect of magnetic field, field orientation, temperature and strain on the critical current density of DI-BiSCCO tapes

7.1 Introduction

Following the preliminary results and analysis of J_c for DI-BiSCCO tapes discussed in Chapter 4, the superconducting properties of these tapes were investigated further using the probe specially designed for the transport $J_c(B,T,\theta,\varepsilon)$ measurements in high magnetic fields. Resistivity measurements were performed as a function of magnetic field orientation, magnitude of magnetic field and temperature. This work provides resistive B_{c2} data complementary to the ac susceptibility data provided previously. The temperature and angular dependence of B_{c2} is discussed in Section 7.2 where the grain alignment within the samples is also included. Transport J_c of the DI-BiSCCO tapes is analysed in Sections 7.3 with consideration of the non-uniform current flow and flux flow along the grain boundaries. Strain effects on the superconducting properties of the DI-BiSCCO tapes are discussed in Section 7.4 and finally we provide concluding comments.

7.2 Upper critical magnetic field

The upper critical magnetic field is one of the most important superconducting parameters. No theoretical model will be able to describe J_c in the extended field and temperature phase space unless the *B*-*T* phase boundary is systematically studied and understood. For BiSCCO (and other HTS), the orientation of magnetic field strongly affects the superconducting properties. In Chapter 6, the ac magnetic susceptibility transitions and the magnetisation J_c were used to formulate $B_{c2}(T)$. The functional form of $B_{c2}(\theta)$ from the anisotropic Ginzburg-Landau theory was used to extract the effective anisotropy of the DI-BiSCCO tapes from the transport $J_c(\theta)$ data. In this section, the $B_{c2}(T,\theta)$ dependency is examined using complementary resistive superconducting transitions.

7.2.1 *B*-*T* phase diagram

Resistive transitions of a DI-BiSCCO bare tape were obtained from the transport measurements at various magnetic fields applied at different angles between the magnetic field and the tape surface. The transitions for parallel magnetic fields (*J* // *B* // *ab*-planes) are shown in Figure 7.1 where the measurements were carried out in the variable-temperature cup immersed in liquid helium in the vertical superconducting magnet using the $J_c(B,T,\theta)$ probe. Similar measurements were performed in liquid nitrogen in the conventional iron-cored electromagnet and the results are presented in Figure 7.2 and Figure 7.3 for magnetic fields applied at different orientations ($J \perp B$). A sharp transition was observed at zero magnetic field while the in-field transitions were broadened as the field increased. This behaviour has been observed before in several HTS systems [229-233] and attributed to thermally activated flux motion. The transition width data (T_{onset} - T_{offset} where T_{onset} and T_{offset} are obtained by extrapolating the transition to the normal state resistance and the zero resistance respectively) from Figure 7.1 is plotted as a function of magnetic field in Figure 7.4

(inset). The width can be as large as 10 K at a magnetic field of 12 T parallel to the tape surface. B_{c2} determined at 1 %, 5 % and 50 % of the normal state resistance (R_n) is shown in Figure 7.4. The B_{c2} values are sensitive to the criterion used due to the broad transitions. In analysis hereafter, the B_{c2} values determined at 1 % R_n are used.

Figure 7.5 shows transition temperature of the DI-BiSCCO bare tape as a function of angle between magnetic field and the tape surface at 0.1 T and 0.2 T. The results imply $B_{c2}(\theta)$ described by the anisotropic Ginzburg-Landau theory. The data are replotted in the inset as a universal curve as a function of $B(\sin^2\theta + \Gamma_{eff}^{-2}\cos^2\theta)^{1/2}$ where Γ_{eff} is 8.5 obtained from the best fit. This is similar to the J_c analysis in Chapter 6 in Figure 6.5. Included in the inset are data for fields applied normal to the tape surface obtained from Figure 7.2.

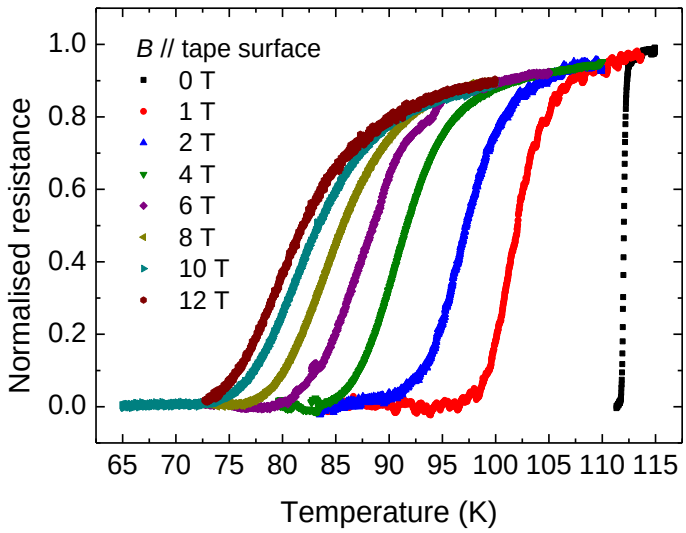

Figure 7.1 Normalised resistance versus temperature for a DI-BiSCCO bare tape as a function of magnetic field applied parallel to the tape surface and the current flow. The applied current was 10 mA for B = 0 – 2 T and 100 mA for B = 4 – 12 T.

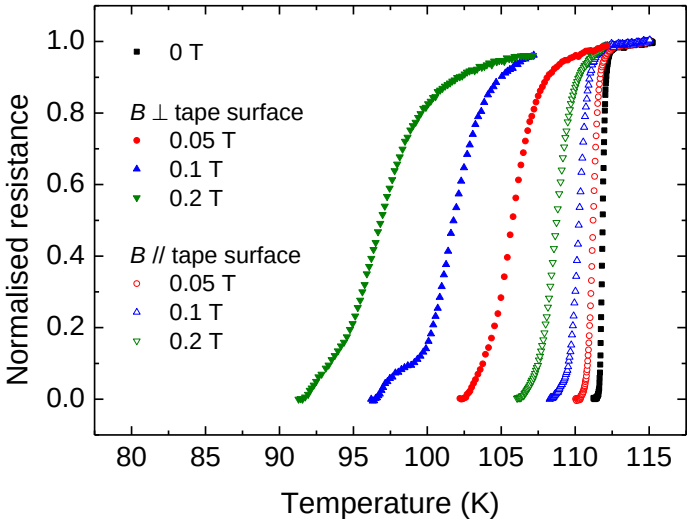

Figure 7.2 Normalised resistance versus temperature for the DI-BiSCCO bare tape as a function of magnetic field applied normal and parallel to the tape surface. In both orientations, the magnetic field was normal to the current flow.

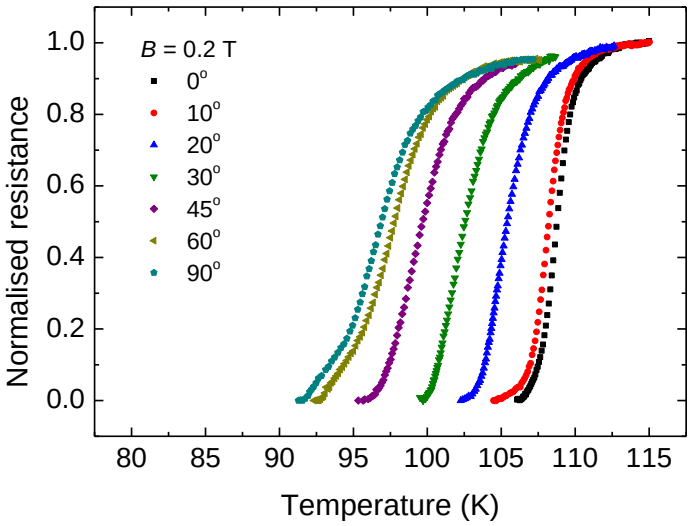

Figure 7.3 Normalised resistance versus temperature for the DI-BiSCCO bare tape as a function of angle between magnetic field and the tape surface at 0.2 T. The magnetic field was normal to the current flow.

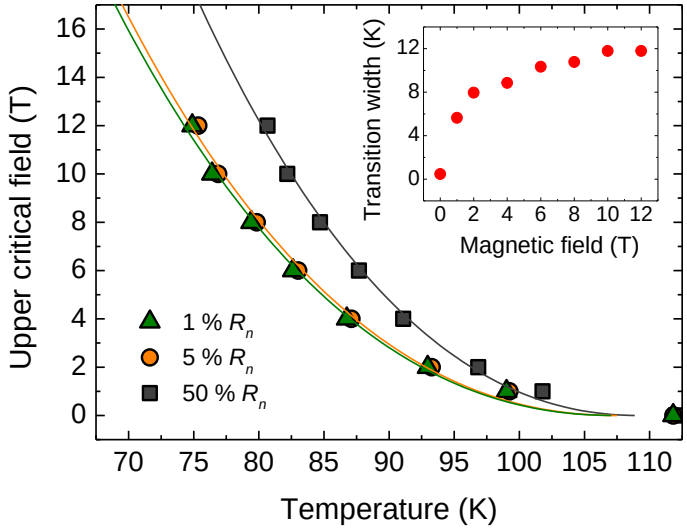

Figure 7.4 Upper critical field versus temperature phase diagram obtained from the resistive transitions of the DI-BiSCCO bare tape presented in Figure 7.1. The magnetic field was applied parallel to the tape surface. The upper critical field was determined at 1 %, 5 % and 50 % of the normal state resistance (R_n). The solid lines are fits to (6.8), giving the values of $B_{c2}(0)$ [T_c] of 508.2 T [107.3 K], 521.7 T [107.5 K] and 714.1 T [109.2 K]. The inset shows transition width, which is the difference between extrapolated onset and offset temperatures of the normal state resistance and the zero resistance respectively, as a function of magnetic field.

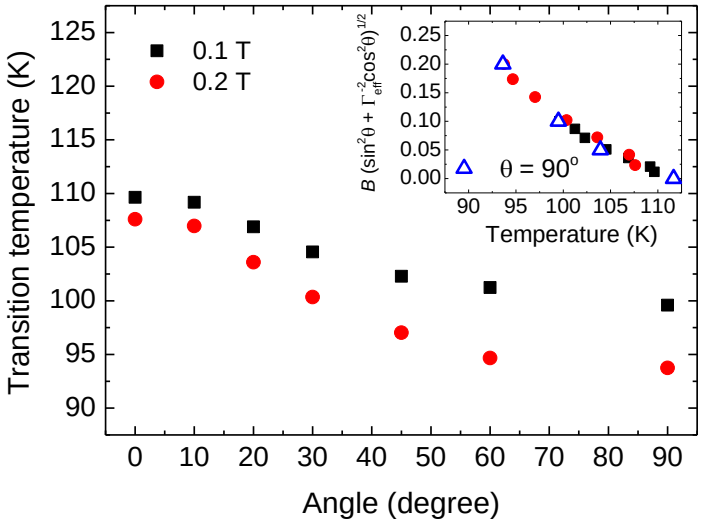

Figure 7.5 Transition temperature at 1 % of the normal state resistance as a function of angle between magnetic field and the surface of the DI-BiSCCO bare tape for the magnetic fields of 0.1 T and 0.2 T. The inset shows data replotted as a function of $B(\sin^2\theta+\Gamma_{eff}^{-2}\cos^2\theta)^{1/2}$ where Γ_{eff} = 8.5. Data from Figure 7.2 for fields applied normal to the tape surface are also plotted for comparison.

7.2.2 Temperature dependence of B_{c2}

B_{c2} obtained from the transport measurements in Figure 7.1 and Figure 7.2 is plotted in Figure 7.6 together with B_{c2} obtained from the ac magnetic susceptibility measurements already presented in Figure 6.3(c) where the DI-BiSCCO bare tape was also used. Both measuring methods give a similar upward curvature of $B_{c2}(T)$ which can be described by (6.8) as shown by the solid lines, except at temperatures close to T_c. The upward curvature of $B_{c2}(T)$ has been observed in several HTS [233, 243, 244, 267-269] and cannot be explained by standard WHH theory. Until now an accurate theoretical explanation of this unconventional behaviour has not been achieved. Some proposed models that provide a $B_{c2}(T)$ versus T relation include the condensation of charged bosons [270, 271], the enhanced thermal fluctuations at low temperature from the reduction in condensation energy by magnetic field [272] and

the melting of vortex lattices [273]. Despite the different fundamental origins of $B_{c2}(T)$ in these models, they all predict a temperature dependence of B_{c2} that depends on the type of materials (the degree of curvature differs from material to material). The work published by Zavaritsky [271] based on the condensation of charged bosons, in particular, demonstrates that there are at least four different groups of unconventional superconductors distinguished by different curvatures of $B_{c2}(T)$. All of them exhibit a universal $B_{c2}(T)$ following $B_{c2} \propto (T_c - T)^{3/2}$ near T_c which diverges in different ways at low temperature. However without experimental B_{c2} data for the entire temperature range or a correct theoretical model, the behaviour of B_{c2} at low temperatures remains uncertain.

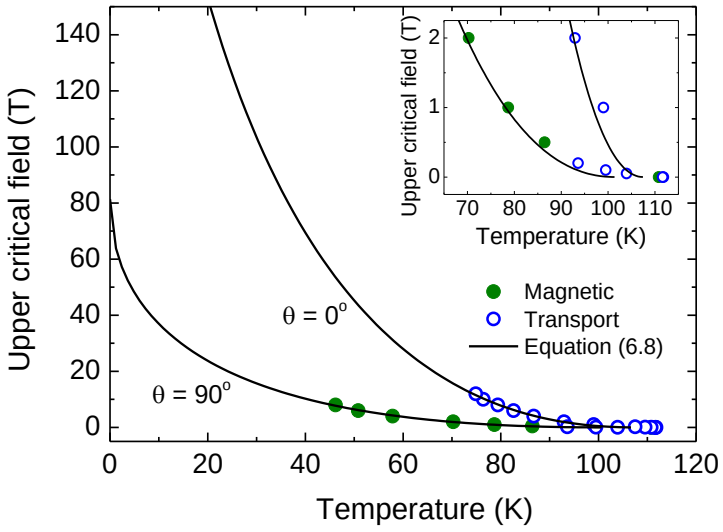

Figure 7.6 Upper critical field versus temperature phase diagram for the DI-BiSCCO bare tape with magnetic fields applied normal and parallel to the tape surface. The magnetic data are taken from Figure 6.3(c) at 1 % of the full screening. The transport data are obtained from the resistive transitions at 1 % of the normal state resistance in Figure 7.1 and Figure 7.2. Solid lines are fits to (6.8) where $T_c(90°)$ = 101.6 K, $B_{c2}(0,90°)$ = 81.4 T, $T_c(0°)$ = 107.6 K and $B_{c2}(0,0°)$ = 500.6 T. The inset shows the same plots near T_c.

Figure 7.7 shows $B_{c2}(T,0°)/B_{c2}(T,90°)$ as a function of temperature for the DI-BiSCCO bare tape calculated from (6.8) with $T_c(90°)$ = 101.6 K, $B_{c2}(0,90°)$ = 81.4 T, $T_c(0°)$ = 107.6 K and $B_{c2}(0,0°)$ = 500.6 T as obtained from the fits in Figure 7.6. The effective anisotropy Γ_{eff} is 6.1 at zero temperature, nearly constant up to around 70 K and rapidly increases at temperatures approaching T_c. Note that Γ_{eff} extracted from the angular J_c and B_{c2} data for the bare tape is 8.0 - 8.6 (see below) which is higher than the calculated Γ_{eff} (T = 0 K) in Figure 7.7. Assuming Γ_{eff} is independent of temperature, the differences are produced by the model used to extrapolate B_{c2} to zero temperature. On the other hand, a weakly-increasing temperature dependence could explain the differences. Recent work on SmBCO and YBCO [274-276] has demonstrated that the anisotropy of SmBCO and YBCO weakly decreases with temperature. Evidence for a temperature dependent Γ_{eff} for BiSCCO has not yet been found, so we have assumed that Γ_{eff} is independent of temperature in the analysis in this chapter.

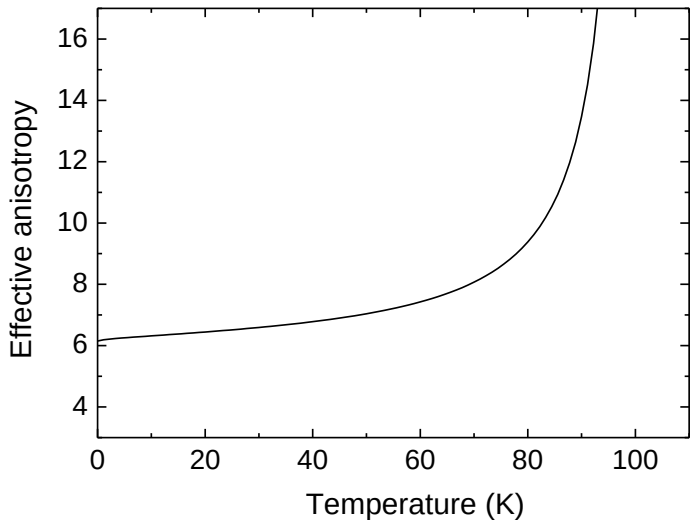

Figure 7.7 Effective anisotropy of the DI-BiSCCO bare tape as a function of temperature calculated from $B_{c2}(T,0°)/B_{c2}(T,90°)$ using $B_{c2}(T)$ from (6.8) where $T_c(90°)$ = 101.6 K, $B_{c2}(0,90°)$ = 81.4 T, $T_c(0°)$ = 107.6 K and $B_{c2}(0,0°)$ = 500.6 T as obtained from the fits in Figure 7.6.

7.2.3 Anisotropy and grain misalignment

The effective anisotropy analysed in Chapter 6 and earlier in this chapter characterises the intrinsic anisotropy Γ of superconductor and the grain misalignment from the anisotropic Ginzburg-Landau theory. In Chapter 4, 2D behaviour ($\Gamma \to \infty$) is assumed and the standard deviation of the misalignment angle σ_{2D} is extracted from the transport J_c data. The relation between σ_{2D} and Γ_{eff} can be obtained by writing the scaling function $f(\theta)$ for the anisotropic Ginzburg-Landau theory as

$$f(\theta) = \left(\sin^2\theta + \frac{1}{\Gamma_{eff}^2}\cos^2\theta \right)^{1/2}, \tag{7.1}$$

which is equivalent to (has the same value as) $f(\theta)$ for the 2D model in Figure 4.10. By calculating $f(0°)$ from (7.1) and using $\sigma_{2D} = 70.9 f(0°)$ from (4.3), one obtains

$$\sigma_{2D} = \frac{70.9}{\Gamma_{eff}} \tag{7.2}$$

where the misalignment effect for the anisotropic Ginzburg-Landau theory is included in Γ_{eff}. Because perfect 2D behaviour is unlikely, σ_{2D} is an overestimate. In Chapter 4, σ_{2D} obtained for the DI-BiSCCO Ag20, SS20, CA50 and bare tapes was between 8.2° to 11.8°. However, the average misalignment angle obtained from the rocking curve measurements at the half width at half maximum (HWHM) is between 6° to 9° [158, 277] and corresponds to the standard deviation of only 5.1° to 7.6° (calculated from HWHM $= \sqrt{2\ln 2}\sigma$ assuming a Gaussian distribution function [278]).

In order to obtain more accurate values for the standard deviation of the misalignment angle to those obtained in Chapter 4, we have reanalysed the data using the anisotropic Ginzburg-Landau theory following an analysis similar to the work of van der Meer [166] to obtain σ_{3D}. The Gaussian distribution function of the *c*-axis grain misalignment *G*(φ) is used and the scaling function at θ = 0° is

numerically calculated from (7.3) for different values of σ_{3D} and Γ. The plot of $f(0°)$ as a function of σ_{3D} is illustrated in Figure 7.8.

$$f(\theta) = \frac{\int_{-90°}^{90°} G(\varphi)[\sin^2(\theta+\varphi) + \Gamma^{-2}\cos^2(\theta+\varphi)]^{1/2} d\varphi}{\int_{-90°}^{90°} G(\varphi)[\sin^2(90°+\varphi) + \Gamma^{-2}\cos^2(90°+\varphi)]^{1/2} d\varphi} \qquad (7.3)$$

For isotropic material (Γ = 1), Figure 7.8 shows that the field orientation and the grain alignment do not affect the superconducting properties because $f(\theta)$ is always equal to 1. On the other hand, for a highly anisotropic material when Γ is larger than ~50 the materials tends to have 2D behaviour where the plot of $f(0°)$ versus σ_{3D} is linear for $\sigma_{3D} \leq 20^{\circ}$ and can be described by $\sigma_{3D} = \sigma_{2D} = 70.9 f(0°)$ from (4.3). $f(0°)$ of the DI-BiSCCO samples measured in this thesis is shown in Table 7.1 which was obtained from J_c measurements at θ = 0° and 90°.

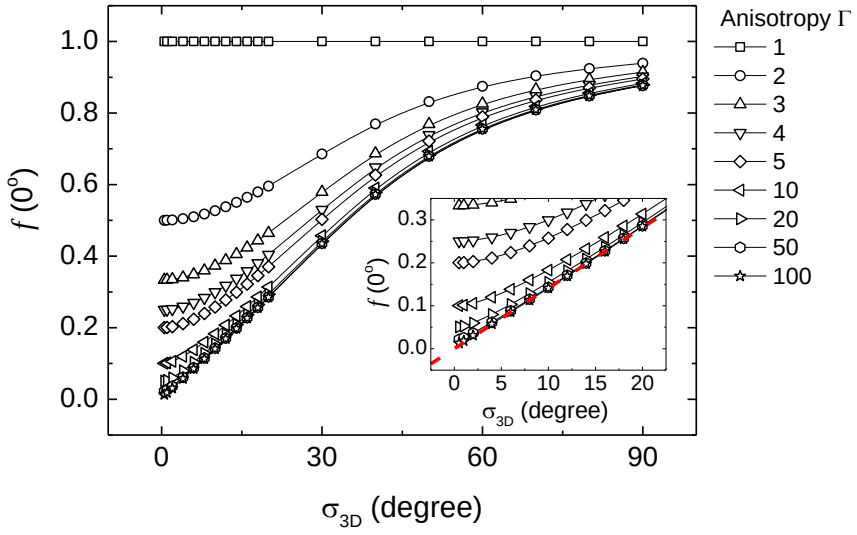

Figure 7.8 The calculated scaling function at θ = 0° as a function of standard deviation of the *c*-axis misalignment angle (σ_{3D}) for various values of the intrinsic anisotropy (Γ). The inset is the same plot in a different scale. Dotted line in the inset is $\sigma_{3D} = \sigma_{2D} = 70.9 f(0°)$ from (4.3).

In Table 7.1 a list of the samples used for each measurement is provided where the grain misalignment characterised from the 2D model in Chapter 4 and Γ_{eff} characterised from the anisotropic Ginzburg-landau theory are also included. The standard deviation of the misalignment angle assuming 2D behaviour ranges from 8.2° to 11.8° which corresponds to an effective anisotropy of 6.0 to 8.6. Equation (7.3) was used to find a range of possible values of σ_{3D} and Γ for each sample which are plotted in Figure 7.9. σ_{3D} reaches its maximum value of σ_{2D} when $\Gamma \geq 50$, while Γ never falls below its minimum of Γ_{eff}. Assuming a standard deviation of the *c*-axis misalignment angle of 5.1° to 7.6° obtained from rocking curve measurements in the literature [158, 277], we conclude that Γ for BiSCCO among the four samples is in the range from 7 to 30. Since the additional lamination process only reinforced the tapes, the variation in the grain misalignment (maximum of 3.6° among the four samples and 0.6° within the same sample, obtained from the 2D model) is simply because the tapes produced by PIT technique have local variations in texturing.

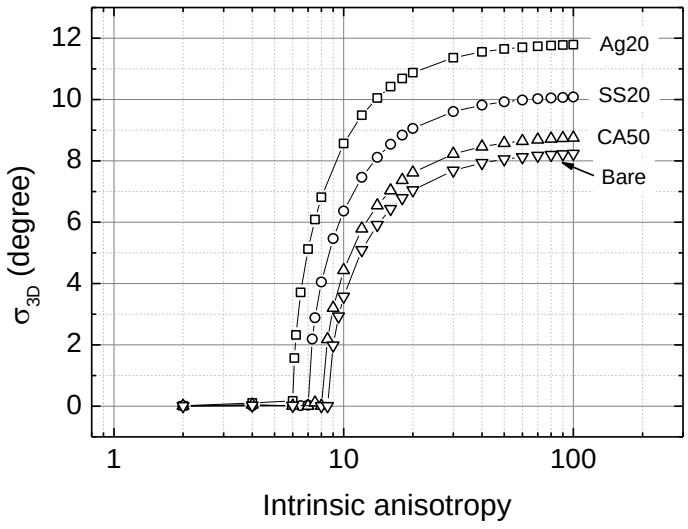

Figure 7.9 The standard deviation of the misalignment angle (σ_{3D}) versus intrinsic anisotropy for the DI-BiSCCO Ag20, SS20, CA50 and bare tapes calculated from (7.3) where the scaling function at $\theta = 0°$ is obtained from the experiments.

Table 7.1 List of DI-BiSCCO samples used for each measurement and parameters representing the anisotropic properties.

Measurement	Sample	σ_{2D} (°)	Γ_{eff}	f (0°)	Reference
$J_c(B)$	Bare	8.2	8.6	0.116	Figure 4.9
θ = 0°, 90°	SS20	10.1	7.0	0.142	
T = 77 K	Ag20	11.8	6.0	0.166	
	CA50	8.8	8.1	0.123	
$J_c(B,\theta)$	CA50	9.1	7.8	-	Figure 6.5(c)
T = 77 K					
$B_{c2}(T,\theta)$	Bare	8.3	8.5	-	Figure 7.5
$T \approx$ 93- 110 K					
$J_c(\theta)$	Bare	8.8	8.0	-	Figure 7.13
B = 0.05 T					
T = 90 K, 100 K					

7.3 Critical current density

7.3.1 Temperature and magnetic field dependence of J_c

The transport critical current density of a DI-BiSCCO CA50 tape was measured at various magnetic fields and temperatures using the $J_c(B,T,\theta,\varepsilon)$ probe described in Chapter 5. Voltage-current characteristics of the tape are shown in Figure 7.10 for the magnetic field applied normal to the tape surface at 20 K, 40 K and 60 K.

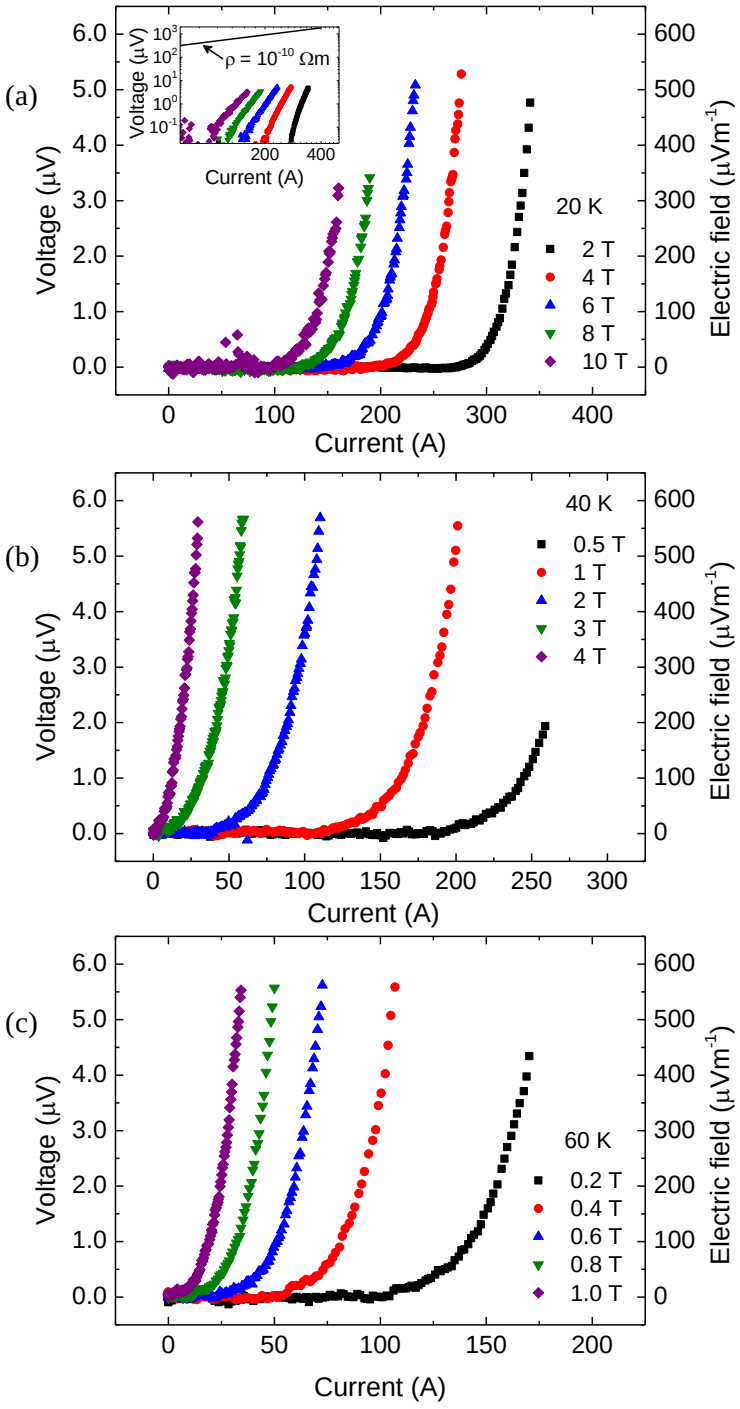

Figure 7.10 Voltage-current characteristics of a DI-BiSCCO CA50 tape at 20 K (a), 40 K (b) and 60 K (c) for various magnetic fields normal to the tape surface. The inset in (a) is the log-log plot of the same data including the resistive curve of silver at 20 K.

The temperature uncertainty in these measurements was ±150 mK. The voltage taps separation was 10 mm. The critical current was determined using the standard 100 μVm^{-1} electric field criterion and also at 4.8 μVm^{-1} (see below). J_c was calculated from the current divided by the unstrained superconducting cross-sectional area of 4.8×10^{-7} m^2. The magnetic field and temperature dependence of the transport J_c is presented in Figure 7.11. At 100 μVm^{-1} electric field criterion, the results show similar $J_c(B)$ behaviour to J_c obtained from the magnetisation measurements on a DI-BiSCCO bare tape. The transport J_c measurements were largely obtained in the high-field exponential regime up to ~400 A. We avoided low-field measurements to avoid high currents damaging the sample either from heating or from mechanical stress. The transport J_c value was higher than the J_c from magnetisation measurements at all temperatures because of the higher electric field at which it was measured [279, 280].

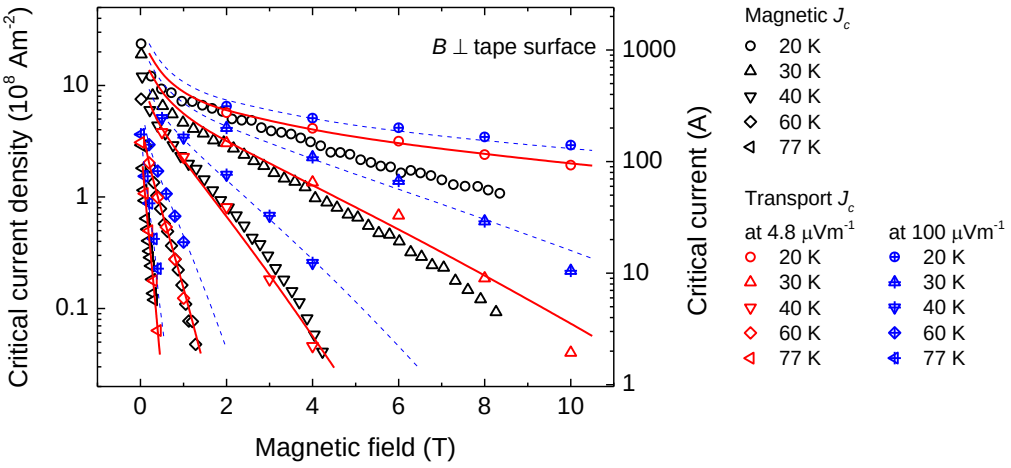

Figure 7.11 Magnetic and transport critical current densities determined at the electric fields of 4.8 μVm^{-1} and 100 μVm^{-1} for the DI-BiSCCO tapes as a function of magnetic field applied normal to the tape surface at different temperatures. Solid lines are fits to the transport data at 4.8 μVm^{-1} using (6.4) and (6.9). Dotted lines are fits to the data at 100 μVm^{-1} using the same equations.

J_c obtained from magnetisation measurements is measured at an effective electric field (E_{eff}) that drives the shielding current to flow within the sample. E_{eff} is induced by penetration of magnetic flux into the sample and can be calculated using the Maxwell-Faraday equation where

$$E_{\text{eff}} = \frac{A_s}{P_s}\frac{\mathrm{d}B}{\mathrm{d}t} \tag{7.4}$$

where A_s is the sample area normal to the applied magnetic field, P_s is the typical path of current flow (say the perimeter of the sample) and dB/dt is the sweep rate of the applied magnetic field. It is known that electric field distributions are position dependent [281]. However, the electric field at the outer regions dominates the magnetic moment, therefore the value near the sample surface is commonly used [282]. The width and the length of the sample used in the magnetisation measurements were 4 mm and 6 mm, respectively. The sweep rate of magnetic field was 0.004 Ts^{-1}. The calculated value of E_{eff} is therefore 4.8 μVm^{-1}, ~20 times lower than the value commonly used in the transport data. The transport J_c of the tape determined at this E_{eff} is also plotted in Figure 7.11 in which the J_c value and the magnetic field dependence are now much more similar to the magnetic J_c. Nonetheless, magnetic and transport data at high magnetic fields and low temperatures (20 K and 30 K) are still different. We can rule out the effect of current flowing across the silver matrix because the transport data were measured at low E-fields - three orders of magnitude below the resistive behaviour of silver as shown by the inset in Figure 7.10(a). The resistivity of silver is about 10^{-10} - 10^{-9} Ωm at the temperature between 20 K to 60 K [283]. A simple requirement for an agreement between the two measurements is that E_{eff} at these fields and temperatures must be lower. Given the inhomogeneous nature of J_c in BiSCCO tapes, the length scale of the magnetic granularity in the magnetisation measurements is typically of the order of several grains [284, 285] and the use of A_s in (7.4) may not give an accurate value of E_{eff}.

We consider the SNS junction model from Chapter 6 to describe the transport J_c data. It is presented by the solid and dotted lines in Figure 7.11. The fitting parameters are summarised in Table 7.2 and the temperature-dependent parameters plotted in Figure 7.12. The Ginzburg-Landau parameter of BiSCCO used in the fitting was 139 [171] and was assumed to be temperature independent. The effective width of the junctions, which is strongly correlated with *r*, was fixed at 122 nm (the value obtained from fitting the magnetisation YBCO data in Chapter 6). The values of d_0 are all small (a few nanometres) and they only affect *d* at low temperature. It was found that the junctions predominantly affecting the transport J_c at 100 μVm^{-1} are thinner than the junctions determining the magnetic J_c. However at the effective electric field of 4.8 μVm^{-1}, the thicknesses of the junctions in the two measurements are similar. Assuming a Gaussian distribution function of the grain misalignment, the sample consists of a number of superconducting grains connected by junctions which have the misalignment angles (or thicknesses) normally distributed. The current flow and magnetic flux penetration in such networks have been observed in YBCO and BiSCCO using the magneto-optical imaging [220, 286, 287], although the out-of-plane misorientation in the PIT BiSCCO tapes makes it more difficult. Computational simulation of the current transfer based on models that explicitly include percolation have been studied and provide a possibility for investigating the influence of the grain orientation [288, 289]. In the dissipation state, the voltage across the grain boundaries is proportional to the flow rate of magnetic flux that preferably penetrates through the defects, cracks and higher-angle grain boundaries [290]. In polycrystalline superconductors where the grain boundary's thicknesses are not identical throughout the material, the current flow and motion of magnetic flux is not uniform. At low electric field where the transport current is low, fluxons essentially move along the higher-angle grain boundaries or the thicker junctions where the intergrain J_c is lower [6]. At high electric field, the dissipation also occurs at the thinner junctions where the intergrain J_c is larger. As a result, the transport J_c determined at high electric field (100 μVm^{-1} in this context) has an average thickness

smaller than that of the thick junctions that are important for low-electric field dissipation.

Figure 7.12 shows that although B_{c2} for the transport and the magnetic J_c data is similar at high temperature, it is significantly different at temperature below 30 K where the B_{c2} value fitted to the transport J_c is larger and cannot be explained by (6.8). The difference at low temperature is influenced by the nature of experimental techniques used. The transport J_c depends on electric field criterion which can be arbitrarily chosen. In contrast, the effective electric field driving the magnetisation J_c may not be constant for all fields and temperatures due to the variation in magnetic granularity. Since the SNS junction model does not include electric field dependency, the fitted B_{c2} can be different if J_c is determined at different electric field. Although Equation (6.8) can describe the experimental $B_{c2}(T)$ data in Figure 7.6 and the literature data for Bi-2223 in Figure 6.4, both data are at high temperatures (above 30 K). In this temperature range, there is no discrepancy between the fitted B_{c2} in Figure 7.12 and Equation (6.8) can also explain the transport data. Therefore a different functional form of $B_{c2}(T)$ that gives a higher value of B_{c2} compared to (6.8) at low temperature should not be discarded. Direct B_{c2} measurements at low temperature/high magnetic field will clarify this problem. Finally, the ratio r extracted from the transport J_c was found to have an exponential temperature dependence described by (6.5) at high temperature. The electric field criterion does not affect the value of r, consistent with r only dependent on structural and chemical compositions of the junctions which are similar throughout the sample. The deviation at 20 K from semiconducting grain boundaries in (6.5) may be attributed to the temperature dependence of κ_{GL} or $\rho_{(S)}$ which has not been included.

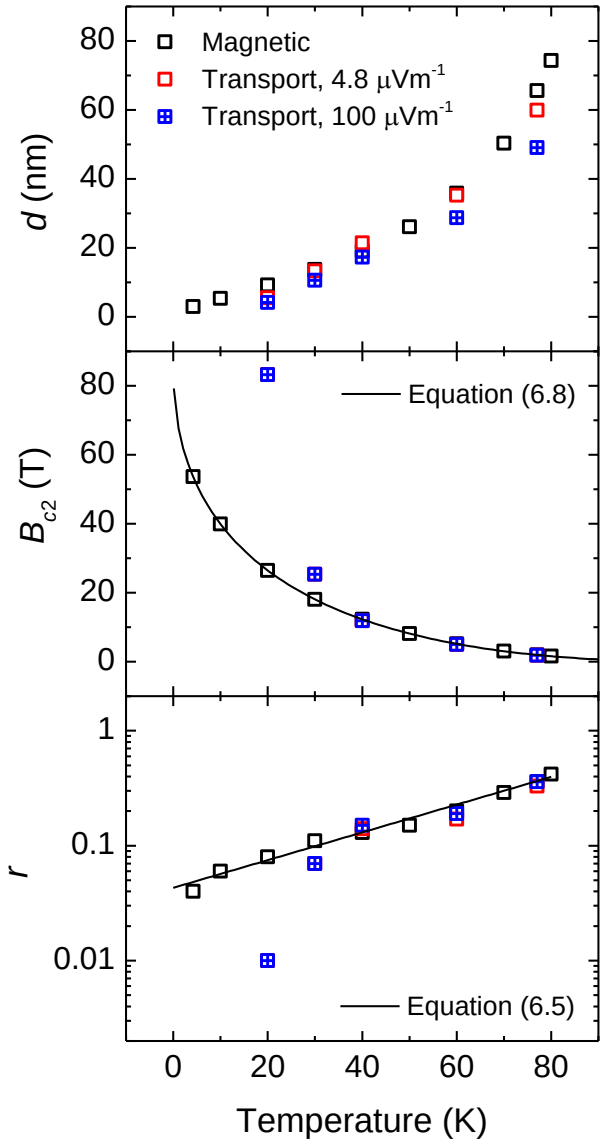

Figure 7.12 Half-thickness (d) of the junction, upper critical magnetic field (B_{c2}) and ratio (r) between normal state resistivities of the superconducting grains and the junctions fitted to the magnetic and the transport J_c data as a function of temperature.

Table 7.2 The value of fitting parameters in (6.4) and (6.9) fitted to the magnetic and the transport J_c data.

Measurement	***E* (μVm^{-1})**	***w* (nm)**	***s***	***d_0* (nm)**
Magnetic	(4.8)	122	6.0	2.0
Transport	4.8	122	4.8	0.9
Transport	100	122	4.0	1.0

7.3.2 Angular dependence of J_c

Detailed anisotropic effects on J_c of a DI-BiSCCO bare tape were investigated by measuring J_c as a function of magnetic field orientation at 90 K and 100 K for the applied magnetic field of 0.05 T. The results are presented in Figure 7.13. The maximum of J_c is found when the magnetic field is applied parallel to the tape surface where B_{c2} is large. The angular data in Figure 7.13 are replotted in the inset as a function of $B(\sin^2\theta + \Gamma_{eff}^{-2}\cos^2\theta)^{1/2}$ where Γ_{eff} = 8.0. The inset is therefore equivalent to the plot of J_c versus magnetic field applied normal to the tape surface at which the data are included and show a good agreement with the angular data.

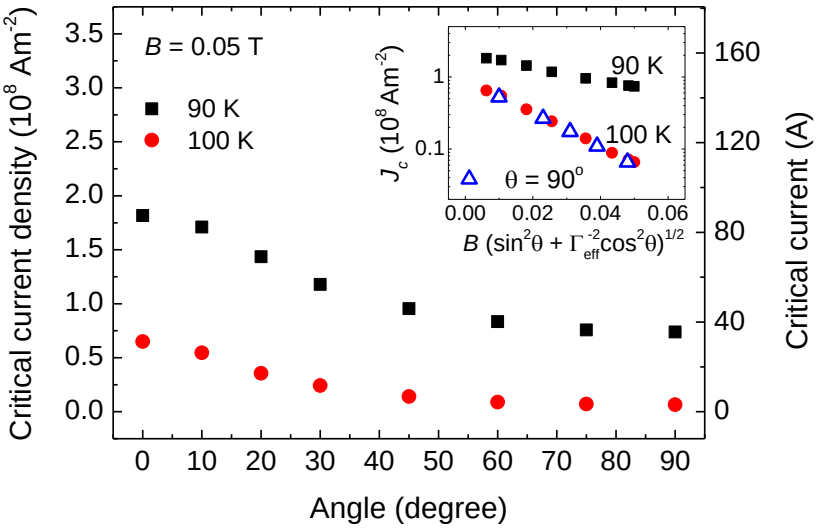

Figure 7.13 Critical current density of a DI-BiSCCO bare tape as a function of angle between applied magnetic field and the tape surface for the magnetic field of 0.05 T at 90 K and 100 K. The inset shows data replotted as a function of $B(\sin^2\theta + \Gamma_{\text{eff}}^{-2}\cos^2\theta)^{1/2}$. Data for fields applied normal to the tape surface at 100 K are also plotted for comparison.

7.4 Effects of strain

The effects of strain on the superconducting properties of BiSCCO are interesting although the measurements are demanding. The critical tensile strains of DI-BiSCCO are only 0.2 % for the bare tapes and 0.3 - 0.4 % for the laminated tapes, depending on the laminating material and thickness. In Chapters 4 and 6, the J_c versus strain measurements at 77 K and 4.2 K were performed and presented up to 0.2 % in tension to avoid damage from exceeding the strain limit. However, irreversibility of J_c was still found in compression even under small compressive strain of -0.1 %. Poor bonding between BiSCCO filaments and silver matrix may provide an

explanation. In this section, J_c versus strain data in the tensile reversible regime are presented in the extended temperature space, made available by the $J_c(B,T,\theta,\varepsilon)$ probe, at various magnetic fields.

J_c measurements as a function of tensile strain up to ~0.2 % were performed using the $J_c(B,T,\theta,\varepsilon)$ probe described in Chapter 5. Figure 7.14 shows the normalised critical current density J_n of a DI-BiSCCO CA50 tape as a function of strain at the temperatures of 20 K, 40 K and 60 K. The dominant source of error was associated with the stability of the sample temperature which was around ±150 mK. Nevertheless, it is discernible that the strain sensitivity of J_n increases with increasing magnetic field at 40 K and 60 K, similar to the results shown in Figure 6.6(d) for magnetic field normal to the tape surface at 77 K and the results presented by van der Laan [291]. On the other hand, the data at 20 K show approximately the same value of $dJ_n/d\varepsilon$ for different magnetic fields, consistent with the 4.2 K results in Figure 6.6(d). It should be noted that the ranges of applied magnetic field for these temperatures are all different. The magnitude of the magnetic field chosen was influenced by the value of the critical current. Comprehensive analysis requires measurements over a large range of reduced magnetic field B/B_{c2} to make comparison between the data at different temperatures. Table 7.3 shows B_{c2} extracted from the transport J_c in the previous section for each temperature, the calculated B/B_{c2} and $dJ_n/d\varepsilon$. The ranges of B/B_{c2} are similar for all temperatures but only the data at 20 K have no significant field dependence. We have found in HTS YBCO that strain sensitivity of J_n is lower at 4.2 K than at 77 K, although no field dependence was observed at both temperatures (see Fig. 6.6). In LTS Nb_3Sn, strain changes T_c and B_{c2} so the lower strain sensitivity at low temperature can be explained by the change in superconducting properties [197]. These results mean that temperature plays an important role in describing the strain dependence in both materials. For BiSCCO, the contrast between the field dependency of $dJ_n/d\varepsilon$ at low and high temperatures will require an understanding of the temperature dependence of strain effects.

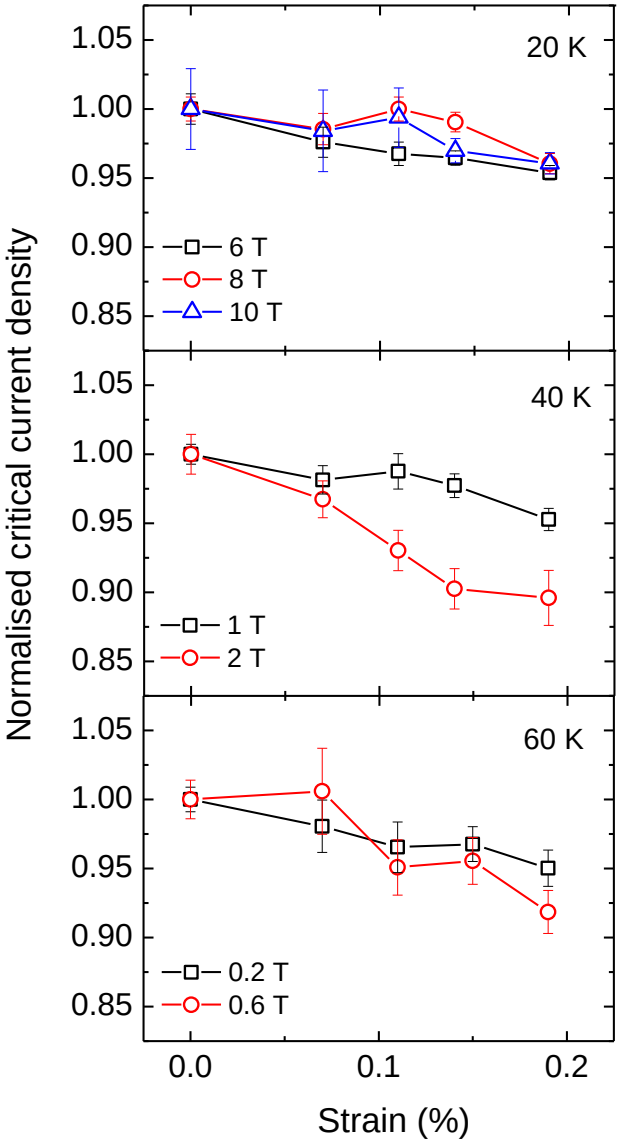

Figure 7.14 Normalised critical current density of a DI-BiSCCO CA50 tape as a function of applied strain at 20 K, 40 K and 60 K at different magnetic fields applied normal to the tape surface. The normalising constants are values of the critical current density at zero applied strain.

Table 7.3 Change in the normalised critical current density with respect to strain ($dJ_n/d\varepsilon$) of the DI-BiSCCO CA50 tapes at different temperatures and magnetic fields.

T (K)	B (T)	B_{c2} (T)	B/B_{c2}	$dJ_n/d\varepsilon$
20	6	83.2	0.07	-25 ± 3
	8		0.10	-15 ± 9
	10		0.12	-17 ± 7
40	1	11.8	0.08	-21 ± 7
	2		0.17	-58 ± 8
60	0.2	5.0	0.04	-24 ± 4
	0.6		0.12	-48 ± 16

Increasing strain sensitivity with magnetic field at 40 K and 60 K (and also 77 K) is attributed to broadening of the effective thickness of the junctions due to tensile strain. However, at this point it remains unclear whether the wider junction is a result of the larger s (grain boundary property) or the degradation of B_{c2} which in turn stretches the coherence length. The effect of strain on the intrinsic superconducting properties of Bi-2223 was observed by Chen [253] where T_c was found to linearly decrease with strain and $dT_c/d\varepsilon$ was -2 K per percent. This result also supports the linearity of J_n versus strain observed in this work and in many studies on BiSCCO family [150, 159, 160, 291]. On the other hand, dislocations along the grain boundaries themselves generate a strain field that distorts the lattice structure. It was proposed following the contraction pairing model [292, 293] that the strain field, which is usually tensile strain over several nanometres from the dislocation cores, creates nonpairing (normal) regions. This explanation tries to explain the origin of the weak-link behaviour of the grain boundaries in HTS and the shift of maximum J_c

to compressive strain found in YBCO [250]. The external tensile strain applied to the sample will accumulate at the grain boundaries and increase the strain field amplitude. As a result, the distance from dislocation cores at which the strain is larger than the critical value that quenches the pairing mechanism (1.0 % in this model) is extended. The increase of *s* due to applied strain is supported by this explanation. However it is clear that a complete understanding of the strain effects at the grain boundaries or understanding the grain boundaries themselves requires knowledge of the fundamental pairing mechanisms which is still lacking.

7.5 Concluding comments

Our group has successfully developed a theoretical model to describe J_c in polycrystalline superconductors where the dissipation arises from flux flow along the grain boundaries. The model is applicable for both LTS and HTS despite the pairing mechanism in the latter case still being unknown. For DI-BiSCCO tapes, the magnetisation and transport J_c data confirm the occurrence and fundamental nature of the SNS junctions within the superconductor.

Although the three-dimensional grain boundary network in DI-BiSCCO tapes makes it more complicated to characterise the anisotropic superconducting properties in this material, the following simple conclusions can be made. Firstly, any direction of the grain misorientation (in-plane and out-of-plane) can limit the current flow due to the normal-conducting properties of the grain boundaries. Out-of-plane misorientation, in particular, has an important effect on the anisotropic properties of the tapes. Any analysis that includes this grain misalignment may describe the angular data equivalently well. However, in order to obtain an accurate measure of the texturing within the tape that is useful for further analysis and interpretation, the model must be carefully chosen. The anisotropic Ginzburg-Landau theory has been used to

describe the angular dependence of B_{c2} in this thesis and there is no doubt that it explains the data even if the intrinsic anisotropy of BiSCCO and the average grain misalignment are not well known. The large range of intrinsic anisotropy reported in literatures limits the utility of the theory. Nevertheless, the correlation between the effective properties and the texturing of samples can be established from experimental data.

There exists a restriction to understanding J_c in BiSCCO, which is not from the model itself but results from the uncertain theoretical picture of the pairing mechanism in HTS. The SNS junction model does not require knowledge of pairing, however it will be necessary in order to describe strain effects on polycrystalline sample. Comprehensive experimental investigation will simplify the problem, even though it is not easy to make an extremely-high field measurement or probe local superconducting properties on the scale of a few nanometres. We return to this challenge in the next chapter where some possible research directions are suggested.

Chapter 8

Future work

In this chapter, we will consider the possible directions of some future work. The probe designed for comprehensive $J_c(B,T,\theta,\varepsilon)$ measurements presented in Chapter 5 has incorporated a variable-temperature insulating cup with the springboard-shaped sample holder. The sample holder is suitable for strain and angular measurements on high-temperature superconducting tapes, such as BiSCCO and YBCO, in high magnetic fields. BiSCCO tapes itself have been developed continuously in their texturing and homogeneity of the superconducting phase since the manufacturing process is still dominated by the powder-in-tube technique. It has been shown that improving the grain alignment in the tapes enhances J_c because the grain boundaries in BiSCCO exhibit the weak-link behaviour. SEI has already achieved the critical current of 200 A at 77 K for their DI-BiSCCO tapes and potentially it can be even higher. Therefore, the probe used to characterise J_c of the tapes need to be able to carry the high current and at the same time remain economically efficient. In this thesis, optimisation of the current leads based on the boil-off gas cooling is presented. The work provides the framework for future design and calculation of the current leads carrying high current into the cryogen. The current leads inside the variable-temperature cup are of concern to the author. More work is required to consider the high-current leads that need to be flexible or bendable without becoming damaged while the strain is applied. Stacks of YBCO tapes have been used due to the flexibility of the tapes and the excellent in-field performance of YBCO. Nevertheless, these current leads have not been fully tested with high current in the large strain range (-1.4 % to 1.0 %) that the springboard-shaped sample holder is capable of because J_c of DI-BiSCCO tapes measured here are only reversible in

tension up to about 0.2 - 0.4 %. Ultimately, examination and modification of the flexible high-current leads will be required.

It has been suggested that J_c degradation in compression is a result of filament buckling and delamination between the filament and silver matrix. However, in situ scanning electron microscope of the tape's microstructure under both tensile and compressive strains should also be examined. Another study that will give a better understanding of electro-mechanical properties of BiSCCO is direct mechanical measurements such as stress-strain measurement (extended into compression where standard tensile testing equipment cannot be used) and Poisson ratios measurement of the filaments. Commercially available BiSCCO tapes are generally multifilamentary, therefore a single filament will need to be extracted from the tape. Extracting BiSCCO filaments is usually done by chemical etching methods with a diluted solution of ammonium hydroxide (NH_4OH) and hydrogen peroxide (H_2O_2) in deionised water [294]. A problem with the chemical etching is that branching and nonuniformity of the filaments make it difficult to separate them from each other or even from the inner silver matrix. Accordingly, other techniques such as Focused Ion Beam milling should be considered.

The SNS junction model developed in our group to describe J_c in polycrystalline LTS and HTS has been successfully used for Nb_3Sn, YBCO and BiSCCO. It has provided useful information on the important properties of the grain boundaries in these materials. It is essential that the model is to be assessed with other superconductors as well. Interesting materials include MgB_2 and iron-based superconductor, where the grain boundaries are found to exhibit a similar behaviour to LTS and HTS, respectively. In addition, the SNS junction model itself describes J_c in polycrystalline superconductors from the average superconducting properties. Therefore, some poorly understood properties of superconductors may not be determined unless an additional knowledge is brought to bear. For instance, the reversible strain dependence of J_c in BiSCCO tapes is believed to involve the

increasing effective thickness of the junctions that suppress J_c, however it remains unknown whether this is due to B_{c2} degradation or from increasing the characteristic thickness parameter of the junctions. To obtain more useful information, it will require further investigation of microscopic superconducting and grain boundary properties. Theoretical development will also require an insight of how superconductivity arises in HTS. It will include deriving the temperature and strain dependencies of fitting parameters in the model for which at the moment, simple scaling functions are applied. We believe that information obtained from our analysis here and further improvements will bring a big impact to the research and development of superconductors in the near future.

Appendix 1: Publications

P. Sunwong, J. S. Higgins, and D. P. Hampshire, "Probes for investigating the effect of magnetic field, field orientation, temperature and strain on the critical current density of anisotropic high-temperature superconducting tapes in a split-pair 15 T horizontal magnet," In progress, 2013.

P. Sunwong, J. S. Higgins, Y. Tsui, M. J. Raine, and D. P. Hampshire, "The critical current density of grain boundary channels in polycrystalline HTS and LTS superconductors in magnetic fields," *Superconductor Science and Technology*, vol. 26, pp. 095006, 2013.

P. Sunwong, J. S. Higgins, and D. P. Hampshire, "Angular, temperature and strain dependencies of the critical current of DI-BSCCO tapes in high magnetic fields," *IEEE Transactions on Applied Superconductivity*, vol. 21, pp. 2840-2844, 2011.

P. Sunwong, J. S. Higgins, and D. P. Hampshire, "Critical current measurements of DI-BSCCO tapes as a function of angle in high magnetic fields," *Journal of Physics: Conference Series*, vol. 234, pp. 022013, 2010.

Appendix 2: Conferences and courses

Superconductivity and Quantum Fluids, 8 July 2013, Institute of Physics, London, UK

Fusion Frontiers and Interfaces Workshop, 13 May 2013, York Plasma Institute, York, UK

The Applied Superconductivity Conference, 7 – 12 October 2012, Portland, Oregon, USA

Superconductivity Summer School, 9 – 11 July 2012, University of Oxford, UK

The European Conference on Applied Superconductivity, 18 – 23 September 2011, The Hague, The Netherlands

Superconductivity Summer School, 11 – 12 July 2011, University of Cambridge, UK

The Applied Superconductivity Conference, 1 – 6 August 2010, Washington, D C, USA

The European Conference on Applied Superconductivity, 13 – 17 September 2009, Dresden, Germany

Appendix 3: Computer programs

LabVIEW

For the transport J_c(B,T,θ,ε) measurements, the programs used are listed below.

Project - Temperature profile.lvproj

To run temperature profile measurements of the current leads with 5 measuring inputs, the applied current can be constant or ramping. It was also used for J_c measurements with an option of sample's temperature reading.

Project - Temperature control.lvproj

To control the sample's temperature inside the variable-temperature system, specific for LakeShore 336 temperature controller.

Strain Gauge.vi

To apply strain to the sample with the additional use of JVL's MacTalk.

PPMS MultiVu

To control the Quantum Design PPMS system for dc magnetisation and ac magnetic susceptibility measurements.

FlexPDE

To obtained numerical solutions of the heat transfer equation for the vapour-cooled current leads.

Mathematica

To perform general calculations, in particular integration of the grain misalignment and effective normal magnetic field.

Excel with Solver Add-in

To fit the experimental J_c data with Equation (6.4) from the SNS junction model.

References

[1] "The first LHC protons run ends with new milestone," CERN press office, 2012.

[2] "www.iter.org," 2008.

[3] W. J. Nuttall, R. H. Clarke, and B. A. Glowacki, "Stop Squandering Helium," *Nature*, vol. 485, pp. 573, 2012.

[4] S. Connor, "A ballooning problem: the great helium shortage," in *The Independent*, 2013.

[5] J. G. Bednorz and K. A. Müller, "Possible high T_C superconductivity in the Ba-La-Cu-O system," *Zeitschrift für Physik B*, vol. 64, pp. 189-193, 1986.

[6] D. Dimos, P. Chaudhari, and J. Mannhart, "Superconducting transport properties of grain boundaries in $YBa_2Cu_3O_7$ bicrystals," *Physical Review B*, vol. 41, pp. 4038-4049, 1990.

[7] R. L. Fagaly, "Superconducting quantum interference device instruments and applications," *Review of Scientific Instruments*, vol. 77, pp. 101101, 2006.

[8] H. K. Onnes, "Further Experiments with Liquid Helium. G On the Electrical Resistance of Pure Metals, etc VI. On the Sudden Change in the Rate at which the Resistance of Mercury Disappears," *Communications from the Physical Laboratory of the University of Leiden*, vol. 124C, pp. 21-26, 1911.

[9] W. Meissner and R. Ochsenfeld, "Ein neuer Effekt bei Eintritt der Supraleitfähigkeit," *Naturwissenschaften*, vol. 21, pp. 787-788, 1933.

[10] C. Kittel, *Introduction to solid state physics*, seventh ed: John Wiley & Sons, 1996.

[11] F. London and H. London, "The electromagnetic equations of the supraconductor," *Proc Roy Soc (London)*, vol. A149, pp. 71-88, 1935.

[12] L. D. Landau, "Zur Theorie der Phasenumwandlungen II," *Physikalische Zeitschrift der Sowjetunion*, vol. 11, pp. 545 - 555, 1937.

[13] V. L. Ginzburg and L. D. Landau, "On the Theory of Superconductivity," *Zhurnal Eksperimentalnoj i Teoreticheskoj Fiziki*, vol. 20, pp. 1064-1082, 1950.

[14] A. A. Abrikosov, "On the magnetic properties of superconductors of the second group," *Soviet Physics JETP*, vol. 5, pp. 1174-1182, 1957.

[15] A. A. Abrikosov, "The Magnetic Properties of Superconducting Alloys," *Journal of Physics and Chemistry of Solids*, vol. 2, pp. 199-208, 1957.

[16] W. H. Kleiner, L. M. Roth, and S. H. Autler, "Bulk Solution of Ginzburg-Landau Equations for Type II Superconductors: Upper critical field region," *Physical Review*, vol. 133, pp. A1226-A1227, 1964.

[17] D. R. Tilley and J. Tilley, *Superfluidity and Superconductivity*, 3rd ed. Bristol: IOP publishing Ltd., 1990.

[18] C. P. Poole, H. A. Farach, and R. J. Creswick, *Superconductivity*. San Diego, California: Academic Press Inc, 1995.

[19] J. R. Clem, "Anisotropy and two-dimensional behaviour in the high-temperature superconductors," *Superconductor Science and Technology*, vol. 11, pp. 909-914, 1998.

[20] J. R. Clem, "Phenomenological Theory of Magnetic Structure in the High-Temperature Superconductors," *Physica C*, vol. 162-164, pp. 1137-1142, 1989.

[21] J. R. Clem, "Two-dimensional vortices in a stack of thin superconducting films: A model for high-temperature superconducting multilayers," *Physical Review B*, vol. 43, pp. 7837-7846, 1991.

[22] A. B. Sneary, "The Fabrication of a High Temperature Superconducting Magnet and Critical Current Characterisation of the Component $Bi_2Sr_2Ca_2Cu_3O_x$ Tapes and Filaments in High Magnetic Fields," *Thesis: Department of Physics, Durham University*, pp. 1-156, 2000.

[23] W. E. Lawrence and S. Doniach, "Theory of layer structure superconductors," presented at Proceedings of the twelfth international conference on low temperature physics, Kyoto, 1971.

[24] M. Tinkham, "Effect of Fluxoid Quantization on Transition of Superconducting Films," *Physical Review*, vol. 129, pp. 2413-2422, 1963.

[25] E. Maxwell, "Isotope effect in the superconductivity of mercury," *Physical Review*, vol. 78, pp. 477, 1950.

[26] C. A. Reynolds, B. Serin, W. H. Wright, and L. B. Nesbitt, "Superconductivity of isotopes of mercury," *Physical Review*, vol. 78, pp. 487, 1950.

[27] J. Bardeen, L. N. Cooper, and J. R. Schrieffer, "Theory of Superconductivity," *Physical Review*, vol. 108, pp. 1175-1204, 1957.

[28] V. Z. Kresin and S. A. Wolf, *Fundamentals of superconductivity*. New York: Plenum, 1990.

[29] R. E. Glover and M. Tinkham, "Transmission of Superconducting Films at Millimeter-Microwave and Far Infrared Frequencies," *Physical Review*, vol. 104, pp. 844-845, 1956.

[30] M. Tinkham, "Energy Gap Interpretation of Experiments on Infrared Transmission through Superconducting Films," *Physical Review*, vol. 104, pp. 845-846, 1956.

[31] G. M. Éliashberg, "Interactions between electrons and lattice vibrations in a superconductor," *Soviet Physics JETP*, vol. 11, pp. 696-702, 1960.

[32] V. Z. Kresin, H. Gutfreund, and W. A. Little, "Superconducting state in strong coupling," *Solid State Communications*, vol. 51, pp. 339-342, 1984.

[33] V. Z. Kresin, "On the critical-temperature for any strength of the electron phonon coupling," *Physics Letters A*, vol. 122, pp. 434-438, 1987.

[34] M. Cyrot and D. Pavuna, *Introduction to superconductivity and high-Tc materials*. Singapore: World Scientific, 1992.

[35] L. P. Gor'kov, "Microscopic derivation of the Ginzburg-Landau equations in the theory of superconductors," *Soviet Physics JETP*, vol. 9, pp. 1364-1367, 1959.

[36] N. R. Werthamer, E. Helfand, and P. C. Hohenberg, "Temperature and Purity Dependence of the Superconducting Critical Field, H_{C2}. III. Electron Spin and Spin-Orbit Effects.," *Physical Review*, vol. 147, pp. 295-302, 1966.

[37] K. Maki, "Effect of Pauli paramagnetism on magnetic properties of high-field superconductors.," *Physical Review*, vol. 148, pp. 362-369, 1966.

[38] D. D. Osheroff, R. C. Richardson, and D. M. Lee, "Evidence for a New Phase of Solid He^3," *Physical Review Letters*, vol. 28, pp. 885-888, 1972.

[39] D. Vollhardt and P. Wölfle, *The superfluid phases of helium 3*. London: Taylor & Francis, 1990.

[40] K. Ishida, H. Mukuda, Y. Kitaoka, K. Asayama, Z. Q. Mao, Y. Mori, and Y. Maeno, "Spin-triplet superconductivity in Sr_2RuO_4 identified by ^{17}O Knight shift," *Nature*, vol. 396, pp. 658-660, 1998.

[41] K. Ishida, Y. Kitaoka, and K. Asayama, "Anisotropic pairing in superconducting Sr_2RuO_4: Ru NMR and NQR studies," *Physical Review B*, vol. 56, pp. R505-R508, 1997.

[42] D. F. Agterberg, "Vortex Lattice Structures of Sr_2RuO_4," *Physical Review Letters*, vol. 80, pp. 5184-5187, 1998.

[43] I. J. Lee and M. J. Naughton, "Anisotropy of the Upper Critical Field in $(TMTSF)_2PF_6$," *Physical Review Letters*, vol. 78, pp. 3555-3558, 1997.

[44] H. Tou, Y. Kitaoka, K. Asayama, N. Kimura, Y. Onuki, E. Yamamoto, and K. Maezawa, "Odd-parity superconductivity with parallel spin pairing in UPt_3: evidence from ^{95}Pt Knight shift study," *Physical Review Letters*, vol. 77, pp. 1374-1377, 1996.

[45] H. Tou, Y. Kitaoka, K. Ishida, K. Asayama, N. Kimura, Y. Onuki, E. Yamamoto, Y. Haga, and K. Maezawa, "Nonunitary Spin-Triplet Superconductivity in UPt_3: Evidence from ^{195}Pt Knight Shift Study," *Physical Review Letters*, vol. 80, pp. 3129-3132, 1998.

[46] C. C. Tsuei and J. R. Kirtley, "Phase-Sensitive Evidence for *d*-Wave Pairing Symmetry in Electron-Doped Cuprate Superconductors," *Physical Review Letters*, vol. 85, pp. 182-185, 2000.

[47] C. C. Tsuei and J. R. Kirtley, "Pairing symmetry in cuprate superconductors," *Reviews of Modern Physics*, vol. 72, pp. 969-1016, 2000.

[48] A. P. Mackenzie and Y. Maeno, "p-wave superconductivity," *Physica B*, vol. 280, pp. 148-153, 2000.

[49] R. Beck, Y. Dagan, A. Milner, A. Gerber, and G. Deutscher, "Order-parameter-node removal in the d-wave superconductor $YBa_2Cu_3O_{7-x}$ in a magnetic field," *Physical Review B*, vol. 69, pp. 144506, 2004.

[50] A. A. Abrikosov, "On the nature of the order parameter in HTSC and influence of impurities," *Journal of Physics and Chemistry of Solids*, vol. 56, pp. 1567-1572, 1995.

[51] C. O'Donovan and J. P. Carbotte, "Mixed order parameter symmetry in the BCS model," *Physica C*, vol. 252, pp. 87-99, 1995.

[52] J. Wheatley and T. Xiang, "Stability of d-wave pairing in two dimensions," *Solid State Communications*, vol. 88, pp. 593-595, 1993.

[53] B. E. C. Koltenbah and R. Joynt, "Material-specific gap function in the t–J model of high-temperature superconductors," *Reports on Progress in Physics*, vol. 60, pp. 23-56, 1997.

[54] K. Krishana, N. P. Ong, Q. Li, G. D. Gu, and N. Koshizuka, "Plateaus Observed in the Field Profile of Thermal Conductivity in the Superconductor $Bi_2Sr_2CaCu_2O_8$," *Science*, vol. 277, pp. 83, 1997.

[55] Y. Dagan and G. Deutscher, "Doping and Magnetic Field Dependence of In-Plane Tunneling into $YBa_2Cu_3O_{7-x}$: Possible Evidence for the Existence of a Quantum Critical Point," *Physical Review Letters*, vol. 87, pp. 17704, 2001.

[56] W. A. Fietz and W. W. Webb, "Hysteresis in superconducting alloys - Temperature and field dependence of dislocation pinning in niobium alloys," *Physical Review*, vol. 178, pp. 657-667, 1969.

[57] E. J. Kramer, "Scaling Laws for Flux Pinning in Hard Superconductors," *Journal of Applied Physics*, vol. 44, pp. 1360-1370, 1973.

[58] D. Dew-Hughes, "Flux pinning mechanisms in type II superconductors," *Philosophical Magazine*, vol. 30, pp. 293-305, 1974.

[59] D. J. C. Jackson and M. P. Das, "Melting of the flux line lattice," *Superconductor Science and Technology*, vol. 9, pp. 713-727, 1996.

[60] C. C. Tsuei and J. R. Kirtley, "d-wave pairing symmetry in cuprate superconductors," *Physica C*, vol. 341-348, pp. 1625-1628, 2000.

[61] B. Bucher, J. Karpinski, E. Kaldis, and P. Wachter, "Strong pressure dependence of T_c of the new 80 K phase $YBa_2Cu_4O_{8+x}$," *Physica C: Superconductivity*, vol. 157, pp. 478-482, 1989.

[62] M. Kim, W. Kim, S. B. Lee, S. Yu, J. Kim, and B. Dabrowski, "Thermodynamic properties of $YBa_2Cu_4O_8$ crystal near upper critical fields $H_{c2}(T)$," *Journal of Applied Physics*, vol. 81, pp. 4231-4233, 1997.

[63] M. K. Wu, J. R. Ashburn, C. J. Torng, P. H. Hor, R. L. Meng, L. Gao, Z. J. Huang, Y. Q. Wang, and C. W. Chu, "Superconductivity at 93 K in a new mixed-phase Y-Ba-Cu-O compound system at ambient pressure," *Physical Review Letters*, vol. 58, pp. 908-910, 1987.

[64] T. Sekitani, "Upper critical field for optimally-doped $YBa_2Cu_3O_{7-\delta}$," *Physica B*, vol. 346-347, pp. 319-324, 2004.

[65] J. M. Tarascon, W. R. McKinnon, P. Barboux, D. M. Hwang, B. G. Bagley, L. H. Greene, G. W. Hull, Y. LePage, N. Stoffel, and M. Giroud, "Preparation, structure, and properties of the superconducting compound series $Bi_2Sr_2Ca_{n-1}Cu_nO_y$ with n=1, 2, and 3," *Physical Review B*, vol. 38, pp. 8885-8892, 1988.

[66] S. I. Vedeneev, A. G. M. Jansen, E. Haanappel, and P. Wyder, "Temperature dependence of the upper critical field of $Bi_2Sr_2CuO_x$ single crystals," *Physical Review B*, vol. 60, 1999.

[67] Y. Ando, G. S. Boebinger, A. Passner, L. F. Schneemeyer, T. Kimura, M. Okuya, S. Watauchi, J. Shimoyama, K. Kishio, K. Tamasaku, N. Ichikawa, and S. Uchida, "Resistive upper critical fields and irreversibility lines of optimally doped high-T_c cuprates," *Physical Review B*, vol. 60, pp. 12475-12479, 1999.

[68] I. Matsubara, H. Tanigawa, T. Ogura, H. Yamashita, and M. Kinoshita, "Upper critical field and anisotropy of the high-Tc BSCCO phase," *Physical Review B*, vol. 45, pp. 7414-7417, 1992.

[69] C. Politis and H. L. Luo, "Superconductivity in Tl-Ca-Ba-Cu-O compounds," *Modern Physics Letters B*, vol. 2, pp. 793-798, 1988.

[70] W. Buckel and R. Kleiner, *Superconductivity : fundamentals and applications*: Weinheim ; New York : Wiley-VCH, 2004.

[71] A. Schilling, M. Cantoni, J. D. Guo, and H. R. Ott, "Superconductivity above 130 K in the Hg-Ba-Ca-Cu-O system," *Nature*, vol. 363, pp. 56-58, 1993.

[72] M. Kim, M. Bae, W. Lee, and S. Lee, "Thermodynamic parameters of $HgBa_2Ca_2Cu_3O_{8-x}$ from high-field magnetization," *Physical Review B*, vol. 51, pp. 3261-3264, 1995.

[73] Z.-A. Ren, G.-C. Che, X.-L. Dong, J. Yang, W. Lu, W. Yi, X.-L. Shen, Z.-C. Li, L.-L. Sun, F. Zhou, and Z.-X. Zhao, "Superconductivity and phase diagram in iron-based arsenic-oxides ReFeAsO1-δ (Re = rare-earth metal) without fluorine doping," *EPL*, vol. 83, pp. 17002, 2008.

[74] H. Lee, M. Bartkowiak, J. Park, J. Lee, J. Kim, N. Sung, B. K. Cho, C. Jung, J. Kim, and H. Lee, "Effects of two gaps and paramagnetic pair breaking on the upper critical field of $SmFeAsO_{0.85}$ and $SmFeAsO_{0.8}F_{0.2}$ single crystals," *Physical Review B*, vol. 80, pp. 144512, 2009.

[75] T. Y. Chen, Z. Tesanovic, R. H. Liu, X. H. Chen, and C. L. Chien, "A BCS-like gap in the superconductor $SmFeAsO_{0.85}F_{0.15}$," *Nature*, vol. 453, pp. 1224-1227, 2008.

[76] M. Shahbazi, X. L. Wang, C. Shekhar, O. N. Srivastava, and S. X. Dou, "Upper critical field, critical current density and thermally activated flux flow in fluorine doped CeFeAsO superconductors," *Superconductivity Science and Technology*, vol. 23, pp. 105008, 2010.

[77] J. Paglione and R. L. Greene, "High-temperature superconductivity in iron-based materials," *Nature Physics*, vol. 6, pp. 645-658, 2010.

[78] M. Shahbazi, X. L. Wang, C. Shekhar, O. N. Srivastava, Z. W. Lin, J. G. Zhu, and S. X. Dou, "Upper critical field and thermally activated flux flow in $LaFeAsO_{1-x}F_x$," *Journal of Applied Physics*, vol. 109, pp. 07E162, 2011.

[79] J. Nagamatsu, N. Nakagawa, T. Muranaka, Y. Zenitani, and J. Akimitsu, "Superconductivity at 39 K in magnesium diboride," *Nature*, vol. 410, pp. 63-64, 2001.

[80] L. Lyard, P. Samuely, P. Szabo, C. Marcenat, T. Klein, K. H. P. Kim, C. U. Jung, H. Lee, B. Kang, S. Choi, S. Lee, L. Paulius, J. Marcus, S. Blanchard, A. G. M. Jansen, U. Welp, G. Karapetrov, and W. K. Kwok, "Upper critical magnetic fields in single crystal MgB_2," *Superconductivity Science and Technology*, vol. 16, pp. 193-198, 2003.

[81] A. Kohen and G. Deutscher, "Symmetry and temperature dependence of the order parameter in MgB_2 from point contact measurements," *Physical Review B*, vol. 64, pp. 060506, 2001.

[82] D. Jerome, A. Mazaud, M. Ribault, and K. Bechgaard, "Superconductivity in a synthetic organic conductor $(TMTSF)_2PF_6$," *Journal de Physique Lettres*, vol. 41, pp. L-95-L-98, 1980.

[83] H. Elsinger, J. Wosnitza, S. Wanka, J. Hagel, D. Schweitzer, and W. Strunz, "κ–$(BEDT\text{-}TTF)_2$Cu[N(CN)2]Br: A Fully Gapped Strong-Coupling Superconductor," *Physical Review Letters*, vol. 84, pp. 6098-6101, 2000.

[84] S. Milbradt, A. A. Bardin, C. J. S. Truncik, W. A. Huttema, P. L. Burn, S. C. Lo, B. J. Powell, and M. Broun, "In-plane superfluid density and microwave conductivity of the organic superconductor κ-$(BEDT\text{-}TTF)_2Cu[N(CN)_2]Br$: evidence for d-wave pairing," *arXiv:1210.6405*, 2012.

[85] T. T. M. Palstra, O. Zhou, Y. Iwasa, P. E. Sulewski, R. M. Fleming, and B. R. Zegarski, "Superconductivity at 40 K in Cesium doped C_{60}," *Solid State Communications*, vol. 93, pp. 327-3330, 1995.

[86] Y. Ihara, H. Alloul, P. Wzietek, D. Pontiroli, M. Mazzani, and M. Ricco, "NMR Study of the Mott Transitions to Superconductivity in the Two Cs_3C_{60} Phases," *Physical Review Letters*, vol. 104, pp. 256402, 2010.

[87] F. Steglich, J. Aarts, C. D. Bredl, W. Lieke, D. Meschede, W. Franz, and H. Schafer, "Superconductivity in the Presence of Strong Pauli Paramagnetism: $CeCu_2Si_2$," *Physical Review Letters*, vol. 43, pp. 1892-1896, 1979.

[88] W. Assmus, M. Herrmann, U. Rauchschwalbe, S. Riegel, W. Lieke, H. Spille, S. Horn, G. Weber, F. Steglich, and G. Cordier, "Superconductivity in $CeCu_2Si_2$ Single Crystals," *Physical Review Letters*, vol. 52, pp. 469-472, 1984.

[89] H. A. Vieyra, N. Oeschler, S. Seiro, H. S. Jeevan, C. Geibel, D. Parker, and F. Steglich, "Determination of Gap Symmetry from Angle-Dependent H_{c2} Measurements on $CeCu_2Si_2$," *Physical Review Letters*, vol. 106, pp. 207001, 2011.

[90] C. Petrovic, P. G. Pagliuso, M. F. Hundley, R. Movshovich, J. L. Sarrao, J. D. Thompson, Z. Fisk, and P. Monthoux, "Heavy-fermion superconductivity in $CeCoIn_5$ at 2.3 K," *Journal of Physics: Condensed Matter*, vol. 13, pp. L337-L342, 2001.

[91] L. Howald, G. Knebel, D. Aoki, G. r. Lapertot, and J.-P. Brison, "The upper critical field of CeCoIn5," *New Journal of Physics*, vol. 13, pp. 113039, 2011.

[92] K. Izawa, H. Yamaguchi, Y. Matsuda, H. Shishido, R. Settai, and Y. Onuki, "Angular Position of Nodes in the Superconducting Gap of Quasi-2D Heavy-Fermion Superconductor $CeCoIn_5$," *Physical Review Letters*, vol. 87, pp. 057002, 2001.

[93] G. R. Stewart, Z. Fisk, J. O. Willis, and J. L. Smith, "Possibility of Coexistence of Bulk Superconductivity and Spin Fluctuations in UPt_3," *Physical Review Letters*, vol. 52, pp. 679-682, 1984.

[94] D. Jaccard, J. Flouquet, P. Lejay, and J. L. Tholence, "Transport and magnetic measurements on UPt_3," *Journal of Applied Physics*, vol. 57, pp. 3082-3083, 1985.

[95] D. C. Larbalestier, A. Gurevich, D. M. Feldmann, and A. Polyanskii, "High - T_C superconducting materials for electric power applications," *Nature*, vol. 414, pp. 368-377, 2001.

[96] N. P. Armitage, P. Fournier, and R. L. Greene, "Progress and perspectives on the electron-doped cuprates," *Reviews of Modern Physics*, vol. 82, pp. 2421-2487, 2010.

[97] A. Damascelli, Z. Hussain, and Z. X. Shen, "Angle-resolved photoemission studies of the cuprate superconductors," *Reviews of Modern Physics*, vol. 75, pp. 473-541, 2003.

[98] G. W. Crabtree, J. Z. Liu, A. Umezawa, W. K. Kwok, C. H. Sowers, S. K. Malik, B. W. Veal, D. J. Lam, M. B. Brodsky, and J. W. Downey, "Large

anisotropic critical magnetization currents in single-crystal $YBa_2Cu_3O_{7-\delta}$," *Physical Review B*, vol. 36, pp. 4021-4024, 1987.

[99] H. Maeda, Y. Tanaka, M. Fukutomi, and T. Asano, "A New High-T_c Oxide Superconductor without a Rare Earth Element," *Japanese Journal of Applied Physics*, vol. 27, pp. L209-L210, 1988.

[100] M. R. Presland, J. L. Tallon, R. G. Buckley, R. S. Liu, and N. E. Flower, "General trends in oxygen stoichiometry effects on T_c in Bi and Tl superconductors," *Physica C*, vol. 176, pp. 95-105, 1991.

[101] K. Togano, H. Kumakura, H. Maeda, E. Yanagisawa, and K. Takahashi, "Properties of Pb-doped Bi-Sr-Ca-Cu-O superconductors," *Applied Physics Letters*, vol. 53, pp. 1329, 1988.

[102] S. M. Khalil, "Enhancement of superconducting and mechanical properties in BSCCO with Pb additions," *Journal of Physics and Chemistry of Solids*, vol. 62, pp. 457-466, 2001.

[103] S. Chu and M. E. McHenry, "Critical current density in high-T Bi-2223 single crystals using AC and DC magnetic measurements," *Physica C*, vol. 337, pp. 229-233, 2000.

[104] A. K. Saxena, *High-Temperature Superconductors*: Springer, 2010.

[105] Y. Kamihara, T. Watanabe, M. Hirano, and H. Hosono, "Iron-based layered superconductor $LaO_{1-x}F_x$ FeAs (x=0.05-0.12) with T_c=26 K," *Journal of the American Chemical Society*, vol. 130, pp. 3296, 2008.

[106] Z. Ren, W. Lu, J. Yang, W. Yi, and X. Shen, "Superconductivity at 55 K in Iron-Based F-Doped Layered Quaternary Compound $Sm[O_{1-x}F_x]$ FeAs," *Chinese Physics Letters*, vol. 25, pp. 2215-2216, 2008.

[107] J. Zhao, Q. Huang, C. D. L. Cruz, S. Li, J. W. Lynn, Y. Chen, M. A. Green, G. F. Chen, G. Li, Z. Li, J. L. Luo, N. L. Wang, and P. Dai, "Structural and magnetic phase diagram of $CeFeAsO_{1-x}F_x$ and its relation to high-temperature superconductivity," *Nature Materials*, vol. 7, pp. 953-959, 2008.

[108] H. Q. Yuan, J. Singleton, F. F. Balakirev, S. A. Baily, G. F. Chen, J. L. Luo, and N. L. Wang, "Nearly isotropic superconductivity in $(Ba,K)Fe_2As_2$," *Nature*, vol. 457, pp. 565-568, 2009.

[109] J. L. Zhang, L. Jiao, Y. Chen, and H. Q. Yuan, "Universal behavior of the upper critical field in iron-based superconductors," *Frontiers of Physics*, vol. 6, pp. 463-473, 2011.

[110] A. I. Goldman, D. N. Argyriou, B. Ouladdiaf, T. Chatterji, A. Kreyssig, S. Nandi, N. Ni, S. L. Bud'ko, P. C. Canfield, and R. J. McQueeney, "Lattice and magnetic instabilities in $CaFe_2As_2$: A single-crystal neutron diffraction study," *Physical Review B*, vol. 78, pp. 100506, 2008.

[111] R. M. Norman, "High-temperature superconductivity in the iron pnictides," *Physics*, vol. 1, pp. 21, 2008.

[112] D. G. Hinks, H. Claus, and J. D. Jorgenson, "The complex nature of superconductivity in MgB_2 as revealed by the reduced total isotope effect," *Nature*, vol. 411, pp. 457-460, 2001.

[113] S. L. Bud'ko, G. Lapertot, C. Petrovic, C. E. Cunningham, N. Anderson, and P. C. Canfield, "Boron Isotope Effect in Superconducting MgB_2," *Physical Review Letters*, vol. 86, pp. 1877-1880, 2001.

[114] C. Buzea and T. Yamashita, "Review of the superconducting properties of MgB_2," *Superconductor Science and Technology*, vol. 14, pp. R115-R146, 2001.

[115] S. L. Bud'ko, C. Petrovic, G. Lapertot, C. E. Cunningham, P. C. Canfield, M. H. Jung, and A. H. Lacerda, "Magnetoresistivity and $H_{c2}(T)$ in MgB_2," *Physical Review B*, vol. 63, pp. 220503(R), 2001.

[116] S. L. Bud'ko, V. G. Kogan, and P. C. Canfield, "Determination of superconducting anisotropy from magnetization data on random powders as applied to $LuNi_2B_2C$, YNi_2B_2C, and MgB_2," *Physical Review B*, vol. 64, pp. 180506(R), 2001.

[117] A. Y. Liu, I. I. Mazin, and J. Kortus, "Beyond Eliashberg Superconductivity in MgB_2: Anharmonicity,Two-Phonon Scattering, and Multiple Gaps," *Physical Review Letters*, vol. 87, pp. 087005, 2001.

[118] A. V. Pronin, A. Pimenov, A. Loidl, and S. I. Krasnosvobodtsev, "Optical Conductivity and Penetration Depth in MgB_2," *Physical Review Letters*, vol. 87, pp. 097003, 2001.

[119] C. Eom, M. Lee, J. Choi, L. Belenky, X. Song, L. Cooley, M. Naus, S. Patnaik, J. Jiang, M. Rikel, A. Polyanskii, A. Gurevich, X. Cai, S. Bu, S. Babcock, E. Hellstrom, D. Larbalestier, N. Rogado, K. Regan, M. Hayward, T. He, J. Slusky, K. Inumaru, M. Haas, and R. Cava, "High critical current density and enhanced irreversibility field in superconducting MgB_2 thin films," *Nature*, vol. 411, pp. 558-560, 2001.

[120] K. Bechgaard, C. S. Jacobsen, K. Mortensen, H. J. Pedersen, and N. Thorup, "The properties of five highly conducting salts: $(TMTSF)_2X$, $X = PF_6^-$, AsF_6^-, SbF_6^-, BF_4^- and NO_3^-, derived from tetramethyltetraselenafulvalene (TMTSF)," *Solid State Communications*, vol. 33, pp. 1119-1125, 1980.

[121] Y. V. Sushko, H. Ito, T. Ishiguro, S. Horiuchi, and G. Saito, "Reentrant superconductivity in κ-$(BEDT\text{-}TTF)_2Cu[N(CN)_2]Cl$ and its pressure phase diagram," *Solid State Communications*, vol. 87, pp. 997-1000, 1993.

[122] M. Poirier, D. Fournier, M. Castonguay, and K. D. Truong, "Ultrasonic investigation of the P-T phase diagram of κ-$(BEDT\text{-}TTF)_2X$ organic superconductors," *J. Phys. IV France*, vol. 114, pp. 251-255, 2004.

[123] G. R. Stewart, "Heavy-fermion systems," *Reviews of Modern Physics*, vol. 56, pp. 755-787, 1984.

[124] J. P. Brison, L. Glemot, H. Suderow, A. Huxley, S. Kambe, and J. Flouquet, "Heavy fermion superconductivity," *Physica B*, vol. 280, pp. 165-171, 2000.

[125] N. Mathur, F. Grosche, S. Julian, I. Walker, D. Freye, R. Haselwimmer, and G. Lonzarich, "Magnetically mediated superconductivity in heavy fermion compounds," *Nature*, vol. 394, pp. 39-43, 1998.

[126] M. Jourdan, M. Huth, and H. Adrian, "Superconductivity mediated by spin fluctuations in the heavy-fermion compound UPd_2Al_3," *Nature*, vol. 398, pp. 47-49, 1999.

[127] A. N. Iyer, R. Jammy, and U. Balachandran, "Recent Issues in Fabrication of Ag-Clad BSCCO Superconductors," *Journal of Electronic Materials*, vol. 24, pp. 1873-1876, 1995.

[128] Y. Yamada, M. Mogi, and K. Sato, "Examples and Future Prospects of High-Temperature Superconductor Products," *Sei Technical Review*, vol. 65, pp. 51-59, 2007.

[129] Y. Feng and D. C. LARBALESTIER, "Texture Relationships and Interface Structure in Ag-Sheathed Bi(Pb)-Sr-Ca-Cu-O Superconducting Tapes," *Interface Science*, vol. 1, pp. 401-410, 1994.

[130] Y. Yuan, J. Jiang, X. Y. Cai, D. C. Larbalestier, E. E. Hellstrom, Y. Huang, and R. Parrella, "Significantly enhanced critical current density in Ag-sheathed $(Bi,Pb)_2Sr_2Ca_2Cu_3O_x$ composite conductors prepared by overpressure processing in final heat treatment," *Applied Physics Letters*, vol. 84, pp. 2127-2129, 2004.

[131] M. Kikuchi, N. Ayai, T. Ishida, K. Tatamidani, K. Hayashi, S. Kobayashi, E. Ueno, K. Yamazaki, S. Yamade, H. Takaaze, J. Fujikami, and K. Sato, "Development of New Types of DI-BSCCO Wire," *Sei Technical Review*, pp. 73-80, 2008.

[132] T. Kato, S. Kobayashi, K. Yamazaki, K. Ohkura, M. Ueyama, N. Ayai, J. Fujikami, E. Ueno, M. Kikuchi, K. Hayashi, and K. Sato, "Development of high performance Ag sheathed Bi2223 wire," *Physica C*, vol. 412-414, pp. 1066-1072, 2004.

[133] K. Yamazaki, T. Kato, K. Ohkura, M. Ueyama, N. Ayai, H. Takigawa, B. Ueno, K. Hayashi, and K. Sato, "Development of Ag-sheathed Bi2223 superconducting wires," *Trans Mater Res Soc Jpn*, vol. 29, pp. 1229-1233, 2004.

[134] S. Kobayashi, K. Yamazaki, T. Kato, K. Ohkura, E. Ueno, K. Fujino, J. Fujikami, N. Ayai, M. Kikuchi, K. Hayashi, K. Sato, and R. Hata, "Controlled over-pressure sintering process of Bi2223 wires," *Physica C*, vol. 426-431, pp. 1132-1137, 2005.

[135] "2G HTS Wire," in *www.superpower-inc.com/content/2g-hts-wire*, 2013.

[136] W. Zhang, M. W. Rupich, U. Schoop, D. T. Verebelyi, C. L. H. Thieme, X. Li, T. Kodenkandath, Y. Huang, E. Siegal, D. Buczek, W. Carter, N. Nguyen, J. Schreiber, M. Prasova, J. Lynch, D. Tucker, and S. Fleshler, "Progress in AMSC scale-up of second generation HTS wire," *Physica C*, vol. 463-465, pp. 505-509, 2007.

[137] G. Celentano and A. Augieri, "High temperature superconductivity: challenges and perspectives for electric power applications," in *Energia, Ambiente e Innovazione*, vol. 3, 2012, pp. 60-71.

[138] Y. J. Uemura and A. Keren, "Magnetic-field penetration depth in K_3C_{60} measured by muon spin relaxation," *Nature*, vol. 352, pp. 605-607, 1991.

[139] Y. J. Uemura et al, "Universal Correlations between T_C and n_s/m (Carrier Density over Effective Mass) in High-T_C Cuprate Superconductors," *Physical Review Letters*, vol. 62, pp. 2317-2320, 1989.

[140] Y. J. Uemura, L. P. Le, G. M. Luke, B. J. Sternlieb, W. D. Wu, J. H. Brewer, T. M. Riseman, C. L. Seaman, M. B. Maple, M. Ishikawa, D. G. Hinks, J. D. Jorgensen, G. Saito, and H. Yamochi, "Basic Similarities among Cuprate, Bismuthate, Organic, Chevrel-Phase, and Heavy-Fermion Superconductors shown by Penetration-Depth Measurements," *Physical Review Letters*, vol. 66, pp. 2665-2668, 1991.

[141] N. M. Plakida, *High-Temperature Superconductivity*: Springer-Verlag, 1995.

[142] P. Monthoux and D. Pines, "Spin-Fluctuation-Induced Superconductivity in the Copper Oxides: A Strong Coupling Calculation," *Physical Review Letters*, vol. 69, pp. 961-964, 1992.

[143] S. Chakravarty, A. Sudbø, P. W. Anderson, and S. Strong, "Interlayer Tunneling and Gap Anisotropy in High-Temperature Superconductors," *Science*, vol. 261, pp. 337-340, 1993.

[144] B. Dam, J. M. Hujibregtse, F. C. Klaassen, R. C. F. van der Geest, G. Doornbos, J. H. Rector, A. M. Testa, S. Freisem, J. C. Martinez, B. Stauble-Pumpin, and R. Griessen, "Origin of high critical currents in $YBa_2Cu_3O_{7-d}$ superconducting thin films," *Nature*, vol. 399, pp. 439-442, 1999.

[145] T. Sueyoshi, S. Inada, T. Ueno, N. Jyodai, T. Fujiyoshi, K. Miyahara, T. Ikegami, K. Ebihara, R. Miyagawa, Y. Chimi, and N. Ishikawa, "Effect of controlled densities of columnar defects on pinning parameters in $YBa_2Cu_3O_{7-\delta}$ thin films," *Physica C*, vol. 424, pp. 153-158, 2005.

[146] A. Crisan, S. Fujiwara, J. C. Nie, A. Sundaresan, and H. Ihara, "Sputtered nanodots: A costless method for inducing effective pinning centers in superconducting thin films," *Applied Physics Letters*, vol. 79, pp. 4547-4549, 2001.

[147] R. M. Scanlan, W. A. Fietz, and E. F. Koch, "Flux pinning centers in superconducting Nb_3Sn," *Journal of Applied Physics*, vol. 46, pp. 2244-2249, 1975.

[148] J. Mannhart, P. Chaudhari, D. Dimos, C. C. Tsuei, and T. R. McGuire, "Critical Currents in [001] Grains and across Their Tilt Boundaries in $YBa_2Cu_3O_7$ Films," *Physical Review Letters*, vol. 61, pp. 2476-2479, 1988.

[149] B. ten Haken, A. Beuink, and H. H. J. ten Kate, "Small and Repetitive Axial Strain Reducing the Critical Current in BSCCO/Ag Superconductors," *IEEE Transactions on Applied Superconductivity*, vol. 7, pp. 2034-2037, 1997.

[150] N. Cheggour, X. F. Lu, T. G. Holesinger, T. C. Stauffer, J. Jiang, and L. F. Goodrich, "Reversible effect of strain on transport critical current in $Bi_2Sr_2CaCu_2O_{8+x}$ superconducting wires: a modified descriptive strain model*," *Superconductor Science and Technology*, vol. 25, pp. 015001, 2012.

[151] Y. Ma, "Progress in wire fabrication of iron-based superconductors," *Superconductor Science and Technology*, vol. 25, pp. 113001, 2012.

[152] T. Ozaki, K. Deguchi, Y. Mizuguchi, Y. Kawasaki, T. Tanaka, T. Yamaguchi, H. Kumakura, and Y. Takano, "Fabrication of binary FeSe superconducting wires by diffusion process," *Journal of Applied Physics*, vol. 111, pp. 112620, 2012.

[153] P. Sunwong, J. S. Higgins, and D. P. Hampshire, "Critical current measurements of DI-BSCCO tapes as a function of angle in high magnetic fields," *Journal of Physics: Conference Series*, vol. 234, pp. 022013, 2010.

[154] P. Sunwong, J. S. Higgins, and D. P. Hampshire, "Angular, Temperature and Strain Dependencies of the Critical Current of DI-BSCCO Tapes in High Magnetic Fields," *IEEE Transactions on Applied Superconductivity*, vol. 21, pp. 2840-2844, 2011.

[155] N. Ayai, "DI-BSCCO wires by Controlled over pressure sintering," *Journal of Physics: Conference Series*, vol. 43, pp. 47-50, 2006.

[156] M. Kikuchi, T. Kato, K. Ohkura, N. Ayai, J. Fujikami, K. Fujino, S. Kobayashi, E. Ueno, K. Yamazaki, S. Yamade, K. Hayashi, K. Sato, T. Nagai, and Y. Matsui, "Recent development of drastically innovative BSCCO wire (DI-BSCCO)," *Physica C*, vol. 445-448, pp. 717-721, 2006.

[157] S. Yamade, "Development of high performance DI-BSCCO wire with over 200 A critical current," *Physica C*, vol. 463-465, pp. 821-824, 2007.

[158] N. Ayai, T. Kato, J. Fujikami, S. Kobayashi, M. Kikuchi, K. Yamazaki, S. Yamade, T. Ishida, K. Tatamidani, K. Hayashi, K. Sato, R. Hata, H. Kitaguchi, H. Kumakura, K. Osamura, and J. Shimoyama, "DI-BSCCO Wire with I_c over 200 A at 77 K," *Journal of Physics: Conference Series*, vol. 97, 2008.

[159] K. Osamura, S. Machiya, H. Suzuki, S. Ochiai, H. Adachi, N. Ayai, K. Hayashi, and K. Sato, "Mechanical behavior and strain dependence of the critical current of DI-BSCCO tapes," *Superconductor Science and Technology*, vol. 21, pp. 054010, 2008.

[160] K. Osamura, S. Machiya, H. Suzuki, S. Ochiai, H. Adachi, N. Ayai, K. Hayashi, and K. Sato, "Improvement of Reversible Strain Limit for Critical Current of DI-BSCCO Due to Lamination Technique," *IEEE Transactions on Applied Superconductivity*, vol. 19, pp. 3026-3029, 2009.

[161] M. Kiuchi, S. Takayama, E. S. Otabe, T. Matsushita, J. Fujikami, K. Hayashi, and K. Sato, "Critical current properties in multifilamentary Bi-2223 tape produced by the over pressure processing," *Physica C*, vol. 463-465, pp. 825-828, 2007.

[162] Y. Himeda, M. Kiuchi, E. S. Otabe, and T. Matsushita, "Evaluation of anisotropy of J_c in silver-sheathed Bi-2223 tape," *Physica C*, vol. 426-431, pp. 1170-1175, 2005.

[163] S. Takayama, M. Kiuchi, E. S. Otabe, T. Matsushita, N. Ayai, J. Fujikami, K. Hayashi, and K. Sato, "Evaluation of field-angle anisotropy of critical current in multifilamentary Bi-2223 tapes prepared by CT-OP process," *Physica C*, vol. 468, pp. 1779-1782, 2008.

[164] J. R. Clem, "Pancake vortices," *Journal of Superconductivity*, vol. 17, pp. 613-629, 2004.

[165] P. Schmitt, P. Kummeth, L. Schultz, and G. Saemann-Ischenko, "Two-Dimensional Behavior and Critical-Current Anisotropy in Epitaxial $Bi_2Sr_2CaCu_2O_{8+x}$ Thin Films," *Physical Review Letters*, vol. 67, pp. 267-270, 1991.

[166] O. van der Meer, B. ten Haken, and H. H. J. ten Kate, "A model to describe the angular dependence of the crit6ical current in a Bi2223/Ag superconducting tape," *Physica C*, vol. 357-360, pp. 1174-1177, 2001.

[167] B. Xu, J. H. Su, and J. Schwartz, "Dependence of transport critical current of magnetic field processed $Bi_2Sr_2CaCu_2O_8$/AgMg tapes on the background magnetic field and magnetic field direction," *Superconductor Science and Technology*, vol. 18, pp. 503-507, 2005.

[168] M. Rabara, T. Takeuchi, and K. Miya, "Systematic study of angular hysteresis of critical current density in $Bi_2Sr_2Ca_2Cu_3O_x$ tapes," *Physica C*, vol. 313, pp. 213-218, 1999.

[169] L. F. Goodrich and T. C. Stauffer, "Hysteresis in transport critical-current measurements of oxide superconductors," *IEEE Transactions On Applied Superconductivity*, vol. 11, pp. 3234-3237, 2001.

[170] O. A. Shevchenko, J. J. Rabbers, A. Godeke, B. t. Haken, and H. H. J. t. Kate, "AC loss in a high-temperature superconducting coil," *Physica C*, vol. 310, pp. 106-110, 1998.

[171] D. P. Hampshire, "A barrier to increasing the critical current density of bulk untextured polycrystalline superconductors in high magnetic fields," *Physica C*, vol. 296, pp. 153-166, 1998.

[172] T. Y. Hsiang and D. K. Finnemore, "Superconducting critical currents for thick, clean superconductor-normal-metal-superconductor junctions," *Physical Review B*, vol. 22, pp. 154-163, 1980.

[173] H. J. N. van Eck, L. Vargas, B. ten Haken, and H. H. J. ten Kate, "Bending and axial strain dependence of the critical current in superconducting BSCCO tapes," *Superconductor Science and Technology*, vol. 15, pp. 1213-1215, 2002.

[174] A. Nyilas, K. Osamura, and M. Sugano, "Mechanical and physical properties of Bi-2223 and Nb_3Sn superconducting materials between 300 K and 7 K," *Superconductor Science and Technology*, vol. 16, pp. 1036-1042, 2003.

[175] Y. Zhao, P. Zeng, L. Lei, and H. Yi, "Experimental investigation on constitutive behaviour of superconducting powder BSCCO," *Journal of Materials Science*, vol. 42, pp. 4692-4700, 2007.

[176] J. Y. Pastor, P. Poza, and J. LLorca, "Mechanical Properties of Textured $Bi_2Sr_2CaCu_2O_{8+\delta}$ High-Temperature Superconductors," *Journal of the American Ceramic Society*, vol. 82, pp. 3139-3144, 1999.

[177] A. Salazar, J. Y. Pastor, and J. LLorca, "Fatigue Behavior of Multifilamentary BSCCO 2223/Ag Superconducting Tapes," *IEEE Transactions on Applied Superconductivity*, vol. 14, pp. 1841-1847, 2004.

[178] N. Cheggour and D. P. Hampshire, "A probe for investigating the effects of temperature, strain, and magnetic field on transport critical currents in superconducting wires and tapes," *Review of Scientific Instruments*, vol. 71, pp. 4521-4530, 2000.

[179] A. Godeke, M. Dhallé, A. Morelli, L. Stobbelaar, H. van Weeren, H. J. N. van Eck, W. Abbas, A. Nijhuis, A. den Ouden, and B. ten Haken, "A device to investigate the axial strain dependence of the critical current density in superconductors," *Review of Scientific Instruments*, vol. 75, pp. 5112-5118, 2004.

[180] D. M. J. Taylor and D. P. Hampshire, "Properties of helical springs used to measure the axial strain dependence of the critical current density in superconducting wires," *Superconductor Science and Technology*, vol. 18, pp. 356-368, 2005.

[181] M. N. Wilson, *Superconducting Magnets*: Oxford University Press, 1986.

[182] H. Lee, P. Arakawa, K. R. Efferson, and Y. Isawa, "Helium vapour-cooled brass current leads: experimental and analytical results," *Cryogenics*, vol. 41, pp. 485-489, 2001.

[183] S. Jeong and S. In, "Investigation on vapor-cooled current leads operating in a pulse mode," *Cryogenics*, vol. 44, pp. 241-248, 2004.

[184] L. F. Goodrich, D. F. Vecchia, E. S. Pittman, J. W. Ekin, and A. F. Clark, "Critical current measurements on a NbTi superconducting wire standard reference material," N.B.S. special publication, Boulder No. 260 - 91, 1984.

[185] H. A. Hamid and D. P. Hampshire, "Critical current density of superconductors as a function of strain in high magnetic fields," *Cryogenics*, vol. 38, pp. 1007-1015, 1998.

[186] T. Hasebe, T. Tsuboi, K. Jikihara, S. Yasuhara, J. Sakuraba, M. Ishihara, and Y. Yamada, "Critical current measurement unit utilizing Bi-based oxide superconducting current leads and cryocoolers," *IEEE Transactions on Applied Superconductivity*, vol. 5, pp. 821-824, 1995.

[187] M. A. Young, J. A. Demko, M. J. Gouge, M. O. Pace, J. W. Lue, and R. Grabovickic, "Measurements of the performance of BSCCO HTS tape under magnetic fields with a cryocooled test rig," *IEEE Transactions on Applied Superconductivity*, vol. 13, pp. 2964-2967, 2003.

[188] M. H. Sohn, S. Kim, K. D. Sim, E. Y. Lee, H. M. Kim, H. Y. Park, K. C. Seong, and Y. K. Kwon, "Development of cryogen free I_c measurement system," *Physica C*, vol. 468, pp. 2161-2164, 2008.

[189] L. F. Goodrich, L. T. Medina, and T. C. Stauffer, "High critical-current measurements in liquid and gaseous helium," *Advances in Cryogenic Engineering*, vol. 44, pp. 873-880, 1998.

[190] J. W. Ekin, *Experimental Techniques for Low-Temperature Measurements*. New York: Oxford University Press, 2007.

[191] D. C. van der Laan, H. J. N. van Eck, J. Schwartz, B. ten Haken, and H. H. J. ten Kate, "Interpretation of the critical current in $Bi_2Sr_2Ca_2Cu_3O_x$ tape conductors as parallel weak-link and strong-link paths," *Physica C*, vol. 372-376, pp. 1024-1027, 2002.

[192] K. Osamura, "Force free strain exerted on a YBCO layer at 77 K in surround Cu stabilized YBCO coated conductors," *Superconductor Science and Technology*, vol. 23, pp. 045020, 2010.

[193] J. Ekin, "Strain scaling law for flux pinning in practical superconductors. Pt. 1: basic relationship and application to Nb_3Sn conductors," *Cryogenics*, vol. 20, pp. 611-24, 1980.

[194] C. R. Walters, I. M. Davidson, and G. E. Tuck, "Long sample high sensitivity critical current measurements under strain," *Cryogenics*, vol. 26, pp. 406-412, 1986.

[195] N. Cheggour and D. P. Hampshire, "Unifying the strain and temperature scaling laws for the pinning force density in superconducting niobium-tin multifilamentary wires," *Journal of Applied Physics*, vol. 86, pp. 552-555, 1999.

[196] S. A. Keys, N. Koizumi, and D. P. Hampshire, "The strain and temperature scaling law for the critical current density of a jelly-roll Nb_3Al strand in high magnetic fields," *Superconductor Science and Technology*, vol. 15, pp. 991-1010, 2002.

[197] D. M. J. Taylor and D. P. Hampshire, "The scaling law for the strain dependence of the critical current density in Nb_3Sn superconducting wires," *Superconductor Science and Technology*, vol. 18, pp. S241-S252, 2005.

[198] B. ten Haken, A. Godeke, and H. H. J. ten Kate, "The influence of compressive and tensile axial strain on the critical properties of Nb_3Sn conductors," *IEEE Transactions on Applied Superconductivity*, vol. 5, pp. 1909-1912, 1995.

[199] B. ten Haken, A. Godeke, H. H. J. ten Kate, and W. Specking, "The critical current of Nb_3Sn wires for ITER as a function of the axial tension and compression," *IEEE Transactions on Magnetics*, vol. 32, pp. 2739-2742, 1996.

[200] B. ten Haken, A. Godeke, and H. H. J. ten Kate, "The strain dependence of the critical properties of Nb_3Sn conductors," *Journal of Applied Physics*, vol. 85, pp. 3247-3253, 1999.

[201] "Materials Properties," in *http://cryogenics.nist.gov/MPropsMAY/materialproperties.htm*, 2013.

[202] "Tufnol Fabric Laminates," in *www.tufnol.com*, 2008.

[203] "Thermal Insulation," in *www.proctorgroup.com/products/thermal-insulation/spacetherm*, 2010.

[204] "Thermophysical Properties of Fluid Systems," in *http://webbook.nist.gov/chemistry/fluid/*, 2011.

[205] S. A. Keys and D. P. Hampshire, "Characterisation of the transport critical current density for conductor applications," in *Handbook of Superconducting Materials*, vol. 2, D. Cardwell and D. Ginley, Eds. Bristol: IOP Publishing, 2003, pp. 1297-1322.

[206] G. Morgan, "Optimization of current leads into a cryogenic system," *Brookhaven National Laboratory Report AADD-171*, 1970.

[207] J. P. Holman, *Heat Transfer*: McGraw-Hill, 2002.

[208] S. W. V. Sciver, *Helium Cryogenics*. New York: Plenum Press, 1986.

[209] P. Sunwong, J. S. Higgins, Y. Tsui, M. J. Raine, and D. P. Hampshire, "The critical current density of grain boundary channels in polycrystalline HTS and LTS superconductors in magnetic fields," *Superconductivity Science and Technology*, vol. 26, pp. 095006, 2013.

[210] L. Trappeniers, J. Vanacken, L. Weckhuysen, K. Rosseel, A. Y. Didyk, I. N. Goncharov, L. I. Leonyuk, W. Boon, F. Herlach, V. V. Moshchalkov, and Y. Bruynseraede, "Critical Currents, Pinning Forces and Irreversibility Fields in $(Y_xTm_{1-x})Ba_2Cu_3O_7$ Single Crystals with Columnar Defects in Fields up to 50 T," *Physica C*, vol. 313, 1999.

[211] D. Dew-Hughes, "The critical current of superconductors: an historical review," *Low Temperature Physics*, vol. 27, pp. 713-722, 2001.

[212] D. Dimos, P. Chaudhari, J. Mannhart, and F. K. LeGoues, "Orientation Dependence of Grain-Boundary Critical Currents in $YBa_2Cu_3O_{7-\delta}$ Bicrystals," *Physical Review Letters*, vol. 61, pp. 219-222, 1988.

[213] Z. G. Ivanov, P. Å. Nilsson, D. Winkler, J. A. Alarco, T. Claeson, E. A. Stepantsov, and A. Y. Tzalenchuk, "Weak links and dc SQUIDS on artificial nonsymmetric grain boundaries in $YBa_2Cu_3O_{7-\delta}$," *Applied Physics Letters*, vol. 59, pp. 3030-3032, 1991.

[214] H. Hilgenkamp and J. Mannhart, "Grain boundaries in high-T_c superconductors," *Reviews of Modern Physics*, vol. 74, pp. 485-549, 2002.

[215] S. E. Babcock and J. L. Vargas, "The nature of grain boundaries in the high-T_c superconductors," *Annual Review of Materials Science*, vol. 25, pp. 193-222, 1995.

[216] J. Mannhart, H. Hilgenkamp, B. Mayer, C. Gerber, J. R. Kirtley, K. A. Moler, and M. Sigrist, "Generation of Magnetic Flux by Single Grain Boundaries of $YBa_2Cu_3O_{7-x}$," *Physical Review Letters*, vol. 77, pp. 2782-2785, 1996.

[217] C. Traeholt, J. G. Wen, H. W. Zandbergen, Y. Shen, and J. W. M. Hilgenkamp, "TEM investigation of $YBa_2Cu_3O_7$ thin films on $SrTiO_3$ bicrystals," *Physica C*, vol. 230, pp. 425-434, 1994.

[218] Q. Li, Y. N. Tsay, Y. Zhu, M. Suenaga, G. D. Gu, and N. Koshizuka, "Electromagnetic and microstructural properties of bulk bicrystal grain boundaries in $Bi_2Sr_2CaCu_2O_{8+\delta}$ superconductors," *Physica C*, vol. 341-348, pp. 1407-1410, 2000.

[219] H. Andoh, O. Harnack, M. Darula, and H. Kohlstedt, "Dynamics of order parameter and microwave emission for a $YBa_2Cu_3O_{7-\delta}$ bicrystal junction," *Physica C*, vol. 339, pp. 237-244, 2000.

[220] D. M. Feldmann, J. L. Reeves, A. A. Polyanskii, G. Kozlowski, R. Biggers, R. M. Nekkanti, I. Maartense, M. Tomsic, P. Barnes, C. E. Oberly, T. L. Peterson, S. E. Babcock, and D. C. Larabalestier, "Influence of nickel substrate grain structure on $YBa_2Cu_3O_{7-x}$ supercurrent connectivity in deformation-textured coated conductors," *Applied Physics Letters*, vol. 77, pp. 2906-2908, 2000.

[221] G. J. Carty and D. P. Hampshire, "The critical current density of an SNS junction in high magnetic fields," *Superconductor Science and Technology*, vol. 26, pp. 065007, 2013.

[222] M. Tinkham, *Introduction to Superconductivity*, 2nd ed. Singapore: McGraw-Hill Book Co., 1996.

[223] A. Schmid, "A Time dependent Ginzburg-Landau Equation and its Application to the problem of resistivity in the Mixed State," *Physik der Kondensierte Materie*, vol. 5, pp. 302-317, 1966.

[224] Quantum Design, "PPMS ACMS User's manual," in *PPMS Hardware and Options Manual*. San Diego: Quantum Design, 2004, pp. 1-3.

[225] C. P. Bean, "Magnetization of hard superconductors," *Physical Review Letters*, vol. 8, pp. 250-253, 1962.

[226] C. P. Bean, "Magnetization of high-field superconductors," *Reviews of Modern Physics*, vol. 36, pp. 31-39, 1964.

[227] F. Gomory, "Characterization of high-temperature superconductors by AC susceptibility measurements," *Superconductivity Science and Technology*, vol. 10, pp. 523-542, 1997.

[228] D. Shi, "High temperature superconducting materials science and engineering : new concepts and technology," Oxford: Pergamon, 1995.

[229] M. Tinkham, "Resistive Transition of High-Temperature Superconductors," *Physical Review Letters*, vol. 61, pp. 1658-1661, 1988.

[230] S. Y. Lin, R. S. Liu, D. N. Zheng, W. Y. Liang, and P. P. Edwards, "Granular effects in superconducting $YBa_2Cu_4O_8$ ceramic," *Physica C*, vol. 185-189, pp. 1829-1830, 1991.

[231] T. T. M. Palstra, B. Batlogg, L. F. Schneemeyer, and J. V. Waszczak, "Thermal Activated Dissipation in $Bi_{2.2}Sr_2Ca_{0.8}Cu_2O_{8+\delta}$," *Physical Review Letters*, vol. 61, pp. 1662-1665, 1988.

[232] M. Rupp, A. Gupta, and C. C. Tsuei, "Magnetic field induced broadening of the resistive transition in epitaxial c-axis-oriented $HgBa_2CaCu_2O_{6+\delta}$ films," *Applied Physics Letters*, vol. 67, pp. 291-293, 1995.

[233] S. D. Kaushik and S. Patnaik, "Intergrain connectivity and resistive broadening in vortex state: a comparison between MgB_2, $NbSe_2$ and $Bi_2Sr_2Ca_2Cu_3O_{10}$ superconductors," *IEEE Transactions on Applied Superconductivity*, vol. 17, pp. 3016-3019, 2007.

[234] J. S. Higgins and D. P. Hampshire, "Critical Current Density of $YBa_2Cu_3O_{7-\delta}$ Coated Conductors Under High Compression in High Fields," *IEEE Transactions on Applied Superconductivity*, vol. 21, pp. 3234-3237, 2011.

[235] L. N. Bulaevskii, L. L. Daemen, M. P. Maley, and J. Y. Coulter, "Limits to the critical current in high-Tc superconducting tapes," *Physical Review B*, vol. 48, pp. 798, 1993.

[236] L. Le Lay, C. M. Friend, T. Maruyama, K. Osamura, and D. P. Hampshire, "Evidence that pair breaking at the grain boundaries of Bi2Sr2Ca2Cu3Ox tapes determines the critical current density above 10 K in high fields.," *Journal of Physics: Condensed Matter*, vol. 6, pp. 10053-10066, 1994.

[237] Y. Mawatari, H. Yamasaki, S. Kosaka, and M. Umeda, "Critical current properties and vortex-glass-liquid-transition in Ag-sheathed Bi-2223 tapes," *Cryogenics*, vol. 35, pp. 161-167, 1995.

[238] M. Dhallé, M. Cuthbert, M. D. Johnston, J. Everett, R. Flukiger, S. X. Dou, W. Goldacker, T. Beales, and A. D. Caplin, "Experimental assessment of the current-limiting mechanisms in BSCC0/Ag high temperature superconducting tapes," *Superconductor Science and Technology*, vol. 10, pp. 21-31, 1997.

[239] D. P. Hampshire and S.-W. Chan, "The critical current density in high fields in epitaxial thin films of $YBa_2Cu_3O_7$: flux pinning and pair-breaking," *Journal of Applied Physics*, vol. 72, pp. 4220-4226, 1992.

[240] R. Aymar, "ITER R&D: Executive summary: Design Overview," *Fusion Engineering and Design*, vol. 55, pp. 107-118, 2001.

[241] N. Cheggour and D. P. Hampshire, "The unified strain and temperature scaling law for the pinning force density of bronze-route Nb_3Sn wires in high magnetic fields," *Cryogenics*, vol. 42, pp. 299 - 309, 2002.

[242] A. Godeke, M. C. Jewell, A. A. Golubov, B. Ten Haken, and D. C. Larbalestier, "Inconsistencies between extrapolated and actual critical fields in Nb_3Sn wires as demonstrated by direct measurements of H_{c2}, H* and T_c," *Superconductor Science and Technology*, vol. 16, pp. 1019-1025, 2003.

[243] M. S. Osofsky, R. J. Soulen, S. A. Wolf, J. M. Broto, H. Rakoto, J. C. Ousset, G. Coffe, S. Askenazy, P. Pari, I. Bozovic, J. N. Eckstein, and G. F. Virshup, "Anomalous Temperature Dependence of the Upper Critical Magnetic Field in Bi-Sr-Cu-0," *Physical Review Letters*, vol. 71, pp. 2315, 1993.

[244] V. N. Zavaritsky, M. Springford, and A. S. Alexandrov, "c-axis negative magnetoresistance and upper critical field of $Bi_2Sr_2CaCu_2O_y$," *Europhysics Letters*, vol. 51, pp. 334, 2000.

[245] A. V. Nikulov and Y. D. Remisov, "The critical current of the Josephson junction with boundaries in the mixed state: application to HTSC polycrystalline materials," *Superconductor Science and Technology*, vol. 3, pp. 312-317, 1991.

[246] A. Barone and G. Paterno, *Physics and Applications of the Josephson Effect*. New York: Wiley, 1982.

[247] Z. Hao, "Angular dependences of the thermodynamic and electromagnetic properties of the high-T_C superconductors in the mixed state," *Physical Review B*, vol. 46, pp. 5853-5856, 1992.

[248] K. Tagaya, K. Senda, T. Yosida, N. Fukuoka, and H. Sasakura, "Lower critical fields in Bi-2212 and Bi-2223 superconductors," *Japanese Journal of applied physics*, vol. 31, pp. L 1170-L 1171, 1992.

[249] J. C. Martínez, S. H. Brongersma, A. Koshelev, B. Ivlev, P. H. Kes, R. P. Griessen, D. G. de Groot, Z. Tarnavski, and A. A. Menovsky, "Magnetic Anisotropy of a $Bi_2Sr_2CaCu_2O_x$ Single Crystal," *Physical Review Letters*, vol. 69, pp. 2276-2279, 1992.

[250] M. Sugano, K. Shikimachi, N. Hirano, and S. Nagaya, "The reversible strain effect on critical current over a wide range of temperatures and magnetic fields for YBCO coated conductors," *Superconductor Science and Technology*, vol. 23, pp. 085013, 2010.

[251] D. C. van der Laan, T. J. Haugan, and P. N. Barnes, "Effect of a Compressive Uniaxial Strain on the Critical Current Density of Grain Boundaries in Superconducting $YBa_2Cu_3O_7$ Films," *Physical Review Letters*, vol. 103, pp. 027005, 2009.

[252] U. Welp, M. Grimsditch, S. Fleshler, W. Nessler, J. Downey, and G. W. Crabtree, "Effect of Uniaxial Stress on the Superconducting Transition in $YBa_2Cu_3O_7$," *Physical Review Letters*, vol. 69, pp. 2130, 1992.

[253] X. F. Chen, G. X. Tessema, and M. J. Skove, "Effect of elastic stress on the resistivity and T_c of $(Bi, Pb)_2Sr_2Ca_{n-1}Cu_nO_x$," *Physica C*, vol. 181, pp. 340-344, 1991.

[254] N. Pugh, J. Evetts, and E. Wallach, "A transmission electron-microscopy study of bronze-processed Nb_3Sn and $(Nb,Ta)_3Sn$ multifilamentary superconducting wire," *Journal of Materials Science*, vol. 20, pp. 4521-4526, 1985.

[255] A. Gurevich and E. A. Pashitskii, "Current transport through low-angle grain boundaries in high-temperature superconductors," *Physical Review B*, vol. 57, pp. 13878-13893, 1998.

[256] A. Goyal, S. X. Ren, E. D. Specht, D. M. Kroeger, R. Feenstra, D. Norton, M. Paranthaman, D. F. Lee, and D. K. Christen, "Texture formation and grain boundary networks in rolling assisted biaxially textured substrates and in epitaxial YBCO films on such substrates," *Micron*, vol. 30, pp. 463-478, 1999.

[257] M. P. Maley, P. J. Kung, J. Y. Coulter, W. L. Carter, G. N. Riley, and M. E. McHenry, "Behavior of critical currents in Bi-Pb-Sr-Ca-Cu-O/Ag tapes from transport and magnetization measurement: Dependence upon temperature, magnetic field, and field orientation," *Physical Review B*, vol. 45, pp. 7566-7569, 1992.

[258] Z. H. Wang, "Transport current characteristics in textured $Bi_{1.84}Pb_{0.4}Sr_2Ca_2Cu_3O_y$ silver clamped thick films," *Physica C*, vol. 316, pp. 56-62, 1999.

[259] T. Hamada, R. Morimo, A. Takada, Y. Yamashita, K. Nakayama, and R. Kawano, "Limitation of flux bundle volume and its influence on irreversibility fields," *Materials Chemistry and Physics*, vol. 61, pp. 275-279, 1999.

[260] N. Savvides and S. Gnanarajan, "YSZ buffer layers and YBCO superconducting tapes with enhanced biaxial alignment and properties," *Physica C*, vol. 387, pp. 328-340, 2003.

[261] R. L. Peterson, "Critical-current diffraction patterns of grain-boundary Josephson weak links," *Physical Review B*, vol. 42, pp. 8014-8018, 1990.

[262] Y. H. Li, J. A. Kilner, M. Dhalle, A. D. Caplin, G. Grasso, and R. Flukiger, "'Brick wall' or 'rail switch' - the role of low-angle ab-axis grain boundaries in critical current of BSCCO tapes," *Superconductor Science and Technology*, vol. 8, pp. 764-768, 1995.

[263] D. C. van der Laan, J. Schwartz, B. ten Haken, M. Dhalle, and H. J. N. van Eck, "Limits to the critical current in $Bi_2Sr_2Ca_2Cu_3O_x$ tape conductors: The parallel path model," *Physical Review B*, vol. 77, 2008.

[264] D. T. Verebelyi, D. K. Christen, R. Feenstra, C. Cantoni, A. Goyal, D. F. Lee, and M. Paranthaman, "Low angle grain boundary transport in $YBa_2Cu_3O_{7-\delta}$ coated conductors," *Applied Physics Letters*, vol. 76, pp. 1755-1757, 2000.

[265] T. Shimojima, F. Sakaguchi, K. Ishizaka, Y. Ishida, T. Kiss, M. Okawa, T. Togashi, C. T. Chen, S. Watanabe, M. Arita, K. Shimada, H. Namatame, M. Taniguchi, K. Ohgushi, S. Kasahara, T. Terashima, T. Shibauchi, Y. Matsuda, A. Chainani, and S. Shin, "Orbital-Independent Superconducting Gaps in Iron Pnictides," *Science*, vol. 332, pp. 564-567, 2011.

[266] T. Park, V. A. Sidorov, F. Ronning, J.-X. Zhu, Y. Tokiwa, H. Lee, E. D. Bauer, R. Movshovich, J. L. Sarrao, and J. D. Thompson, "Isotropic quantum scattering and unconventional superconductivity," *Nature*, vol. 456, pp. 366-368, 2008.

[267] A. P. Mackenzie, S. R. Julian, G. G. Lonzarich, A. Ccarrington, S. D. Hughes, R. S. Liu, and D. C. Sinclair, "Resistive upper critical field of $Tl_2Ba_2CuO_6$ at low temperatures and high magnetic fields," *Physical Review Letters*, vol. 71, pp. 1238-1241, 1993.

[268] A. S. Alexandrov, V. N. Zavaritsky, W. Y. Liang, and P. L. Nevsky, "Resistive Upper Critical Field of High-T_c Single Crystals of $Bi_2Sr2CaCu_2O_8$," *Physical Review Letters*, vol. 76, pp. 983-986, 1996.

[269] D. J. C. Walker, O. Laborde, A. P. Mackenzie, S. R. Julian, A. Carrington, J. W. Loram, and J. R. Cooper, "Resistive upper critical field of thin films of underdoped $YBa_2(Cu_{0.97}Zn_{0.03})_3O_{7-\delta}$," *Physical Review B*, vol. 51, pp. 9375-9378, 1995.

[270] V. N. Zavaritsky, "Phase Transition of BSCCO in High Magnetic Fields," *Journal of Superconductivity: Incorporating Novel Magnetism*, vol. 15, pp. 567-570, 2002.

[271] V. N. Zavaritsky, V. V. Kabanov, and A. S. Alexandrov, "Universal upper critical field of unconventional superconductors," *Europhysics Letters*, vol. 60, pp. 127-133, 2002.

[272] J. R. Cooper, J. W. Loram, and J. M. Wade, "Low-temperature increase of resistive critical fields in certain superconductors: A simple fluctuation approach," *Physical Review B*, vol. 51, pp. 6179-6182, 1995.

[273] G. Kotliar and C. M. Varma, "Low-Temperature Upper-Critical-Field Anomalies in Clean Superconductors," *Physical Review Letters*, vol. 77, pp. 2296-2299, 1996.

[274] R. Khasanov, S. Strassle, D. Di Castro, T. Masui, S. Miyasaka, S. Tajima, A. Bussmann-Holder, and H. Keller, "Multiple Gap Symmetries for the Order Parameter of Cuprate Superconductors from Penetration Depth Measurements," *Physical Review Letters*, vol. 99, pp. 237601, 2007.

[275] A. Kortyka, R. Puzniak, A. Wisniewski, M. Zehetmayer, H. W. Weber, C. Y. Tang, X. Yao, and K. Conder, "Evidence for a temperature dependent anisotropy of the superconducting state parameters in underdoped $SmBa_2Cu_3O_x$," *Physical Review B*, vol. 82, pp. 054510, 2010.

[276] S. Bosma, S. Weyeneth, R. Puzniak, A. Erb, A. Schilling, and H. Keller, "Magnetic torque study of the temperature-dependent anisotropy parameter in overdoped superconducting single-crystal $YBa_2Cu_3O_7$," *Physical Review B*, vol. 84, pp. 024514, 2011.

[277] M. Kikuchi, N. Ayai, J. Fujikami, S. Kobayashi, K. Yamazaki, S. Yamade, T. Ishida, T. Kato, K. Hayashi, K. Sato, R. Hata, J. Iihara, K. Yamaguchi, H. Kumakura, H. Kitaguchi, K. Osamura, and J. Shimoyama, "Progress in high

performance DI-BSCCO wire," *AIP Conference Proceedings*, vol. 986, pp. 407-415, 2008.

[278] E. W. Weisstein, "Gaussian Function," MathWorld--A Wolfram Web Resource, 2013.

[279] J. D. Hettinger, D. H. Kim, K. E. Gray, U. Welp, R. T. Kampwirth, and M. Eddy, "Effective electric field in dc magnetization measurements: Comparing magnetization to transport critical currents," *Applied Physics Letters*, vol. 60, pp. 2153-2155, 1992.

[280] J. Horvat, W. K. Yeoh, J. H. Kim, and S. X. Dou, "Transport and magnetic critical current in superconducting MgB_2 wires," *Superconductivity Science and Technology*, vol. 21, pp. 065003, 2008.

[281] T. Schuster, H. Kuhn, and E. H. Brandt, "Flux penetration into flat superconductors of arbitrary shape: Patterns of magnetic and electric fields and current," *Physical Review B*, vol. 54, pp. 3514-3524, 1996.

[282] A. D. Caplin, L. F. Cohen, G. K. Perkins, and A. A. Zhukov, "The electric field within high temperature superconductors: mapping the *E-J-B* surface," *Superconductivity Science and Technology*, vol. 7, pp. 412-422, 1994.

[283] D. R. Smith and F. R. Fickett, "Low-Temperature Properties of Silver," *Journal of Research of NIST*, vol. 100, pp. 119-171, 1995.

[284] A. E. Pashitski, A. Polyanskii, A. Gurevich, J. A. Parrell, and D. C. Larabalestier, "Suppression of magnetic granularity by transport current in $(Bi,Pb)_2Sr_2Ca_2Cu_3O_x$ tapes," *Applied Physics Letters*, vol. 67, pp. 2720-2722, 1995.

[285] A. E. Pashitski, A. Polyanskii, A. Gurevich, J. A. Parrell, and D. C. Larabalestier, "Magnetic granularity, percolation and preferential current flow in a silver-sheathed $Bi_{1.8}Pb_{0.4}Sr_2Ca_2Cu_3O_{8+x}$ tape," *Physica C*, vol. 246, pp. 133-144, 1995.

[286] D. M. Feldmann, J. L. Reeves, A. A. Polyanskii, A. Goyal, R. Feenstra, D. F. Lee, M. Paranthaman, D. M. Kroeger, D. K. Christen, S. E. Babcock, and D. C. Larbalestier, "Magneto-Optical Imaging of Transport Currents in $YBa_2Cu_3O_{7-x}$ on RABiTS^{TM}," *IEEE Transactions on Applied Superconductivity*, vol. 11, pp. 3772-3775, 2001.

[287] A. Polyanskii, D. M. Feldmann, S. Patnaik, J. Jiang, X. Cai, D. Larabalestier, K. DeMoranville, D. Yu, and R. Parrella, "Examination of Current Limiting Mechanisms in Monocore $Bi_2Sr_2Ca_2Cu_3O_x$ Tape with High Critical Current Density," *IEEE Transactions on Applied Superconductivity*, vol. 11, pp. 3269-3272, 2001.

[288] B. Zeimetz, N. A. Rutter, B. A. Glowacki, and J. E. Evetts, "Computer simulation of current percolation in polycrystalline high-temperature superconductors," *Superconductivity Science and Technology*, vol. 14, pp. 672-675, 2001.

[289] B. Zeimetz, B. A. Glowacki, and J. E. Evetts, "Application of percolation theory to current transfer in granular superconductors," *European Physical Journal - B,* vol. 29, pp. 359-367, 2002.

[290] V. Born, K. Guth, H. C. Freyhardt, and C. Jooss, "Self-enhanced flux penetration into small angle grain boundaries in YBCO thin films," *Superconductivity Science and Technology,* vol. 17, pp. 380-385, 2004.

[291] D. C. van der Laan, "Evidence that the reversible strain effect on critical current density and flux pinning in $Bi_2Sr_2Ca_2Cu_3O_x$ tapes is caused entirely by the pressure dependence of the critical temperature," *Superconductor Science and Technology,* vol. 24, pp. 032001, 2011.

[292] G. Deutscher and P. G. De Gennes, "A spatial interpretation of emerging superconductivity in lightly doped cuprates," *C. R. Physique,* vol. 8, pp. 937-941, 2007.

[293] G. Deutscher, "Origin of weak-link behavior of grain boundaries in superconducting cuprates and pnictides," *Applied Physics Letters,* vol. 96, pp. 122502, 2010.

[294] G. Strano, A. S. Siri, and G. Grasso, "Current distribution and microstructure studies of isolated filaments extracted from Ag-sheathed Bi(2223) tapes," *Superconductor Science and Technology,* vol. 13, pp. 1470-1475, 2000.